MPHIL

Functionally Sorted Laminated Material for Damage Resistance and Damage Tolerance

Hua, Shi

Award date:
2018

Awarding institution:
University of Bath

Functionally Sorted Laminated Material for Damage Resistance and Damage Tolerance

Shi Hua

A thesis submitted for the degree of Master of Philosophy

University of Bath

Department of Mechanical Engineering

May 2018

ACKNOWLEDGEMENTS

First and foremost, I would like to express my sincere appreciation and thanks to my supervisor Dr. Andrew Rhead and Professor Richard Butler. Both of you have provided me with endless patience, constant encouragement and unconditional support to my postgraduate and undergraduate research projects. Your professionalism and enthusiasm for research had guided me through tough times and still influence me now. It has been a great honour to be your student.

I would like to thank my precious colleagues, Mark Nielsen, Lucie Culliford, Kevin Johnson, Timothy Fletcher and Zsombor Sapi. Thank you for your help on my research.

The experimental work in this thesis would not have been possible without the help of the technicians of the laboratory. Clare Ball, Steve Thomas and Emma Walker have supported me with preparing the test specimens, setting-up the test rigs and CT scans.

Last but not least, my deepest gratitude goes to my beloved parents in China for their understanding, supports and loves. For more than 12 years being away from home, your loves never fade away, and you always have faith in me. I am proud to be your son.

ABSTRACT

In this thesis, the damage mechanisms and failure behaviours of hybrid laminates panels due to out-of-plane impact and near-edge and on-edge impact were investigated. The impact tests include low-velocity dynamic impact test and quadra-static indentation. Compression after impact was conducted to discover the residual stiffness in the post-test samples and the improvement of damage resistance and damage tolerance are analysed. A novel testing and inspection method had been developed by combining X-ray CT-scan and quadra-static indentation to observe formation of damage gradually and clearly. Finite element models for beams and plates were created to study the interaction between layers and a correlation had been established by an analytical model using through-thickness-shear stress. By adding glass layers into carbon laminates, the hybrid laminates display increases in structural efficiency of up to 32% in comparison to full carbon laminates with identical impact energies. In the on-edge and near-edge impact tests, for blocked stacking sequence, the delaminations and cracks are contained in the middle region of sample, which increases residual stiffness and increase structure damage tolerance.

CONTENTS

List of Figures

List of Tables

Nomenclature

List of Abbreviations

2D	Two-dimensional
3D	Three-dimensional
ASTM	American Society for Testing and Materials
BVID	Barely visible impact damage
CAI	Compression after impact
CDM	Continuum Damage Mechanics
CLT	Classical laminate theory
CT	Computational Tomography
CZM	Cohesive zone modelling
CFRP	Carbon fibre reinforced polymer
DIC	Digital Image Correlation
DoF	Degree of freedom
DIC	DIC Digital Image Correlation
VCCT	Virtual crack closure technique

List of Units

^{o}	Degree
^{o}C	Degree Celsius
fps	Frame per second
GPa	Giga-Pascal
kN	Kilo-Newton
min	Minute
mm	Millimetre
ms	Millisecond
MPa	Mega-Pascal

List of symbol

$E11$, $E22$, $E33$	Elastic Young's moduli
$G11$, $G23$, $G13$	Shear moduli
$v12$, $v13$, $v23$,	Poisson's ratios

σij	Directional stress components
τij	Shear stress components

1 Introduction

1.1 Background

Nowadays, the uses of composites materials, especially Carbon Fibre Reinforced Plastic (CFRP) and Glass Fibre Reinforced Plastic (GFRP), are not limited to military aircrafts but also beginning to significantly influence commercial airliners. The composite materials considered here consist of fibre reinforcement embedded within a brittle matrix. It offers advanced mechanical properties that aluminium alloy is not able to achieve, including high strength-to-weight and stiffness-to-weight ratio, advanced fatigue performance, and corrosion resistance. Most importantly, because of the heterogeneous nature of composites, the mechanical properties in different directions within a component can be tailored as desired. Modern composite manufacturing techniques enable the overall number of parts and consequently production cost to be reduced.

The very first application of composite material in an all-composite kit plane was in 1957 and it was first introduced in commercial aircraft for secondary structure components in 1972. With the latest Airbus A350 XWB and Boeing 787 Dreamliner commercial aircraft being rolled out, the use of advanced composites in overall structural weight has increased from 3% to more than 50% in just under 30 years.

In contrast, the disadvantages of composites material are also very obvious, the most severe problem is known as Barely Visible Impact Damage (BVID). This damage is most likely to be caused by foreign object impact. Significant impact and other forms of loading acting in the direction transverse to the surface is the reason to cause this damage, such as dropping tools during manufacture, small runway debris kicked up from tyres to airframe during taking-off and landing, bird strike, hail impact during flight and even from vehicles during ground handling.

Advanced composites allow the combination of strong fibres, with outstanding load bearing performance in fibre direction, and relatively brittle and weaker polymer matrix to accommodate and transfer the load to the reinforcement, as well as promoting overall formability.

The failure mechanisms of composite and metallic materials are completely different. Since the two constituents of composites are relatively brittle and lack plastic deformation mechanisms compared to metal, composites usually fail in an abrupt behaviour. Impact loading and other transverse loadings give rise to a highly complex internal stress state. These stresses usually act at the matrix regions between fibres where the most vulnerable locations are situated. The lower mechanical properties at the inter-laminar regions allow delamination to occur at a relatively low stress level compared to that in the direction of reinforcement.

Impact induced delamination significantly degrades the residual properties of the structures, the most severe case being compression after impact. For metallic material, this issue is less relevant because impact damage can be easily identified due to the plastic deformation process, and the damage would not significantly affect the residual properties and the integrity of the structure. In the case of composite structures, however, factors which affect design, such as accidental impact damage and manufacturing imperfections, and consequent damage tolerance performance have to be considered and systematically improved.

Developing a reliable methodology that is able to allow composite material resisting foreign impact and improve the damage tolerance has become crucial for the aerospace industry. This methodology has to be both greatly reducing the cost and time spent on validation testing and also maintaining the potential of the weight-saving advantage that composites offer. This is one of the key motivations of the research presented in this report.

1.2 Objectives

The aim of this project is to deliver a solution to improve damage resistance and damage tolerance by investigating the failure mechanisms of composites under low-velocity impact load. In order to achieve this goal, the following objectives are required to be fulfilled;

- Characterise the failure mechanisms and damage formation of laminated composite under low-velocity impact using both dynamic impact and static indentation tests.

Providing useful insight on damage initiation, propagation, and interaction for numerical model validation. Investigate the interaction between inter- and intra-laminar damage.

- Use experimentations, computational simulation and analytical models to investigate the key mechanisms behind the low-velocity impact and compression after impact failure.

- Study the behaviours of GFRP and find out the influence of adding GFRP lamina into CFRP laminates

- Provide possible solutions for improving damage resistance and damage tolerance. Predicting and preventing BVID in composite structures in order to obtain a better CAI performance.

1.3 Thesis Structure

This study of the low-velocity impact and compression after impact of laminated composite material is presented in 5 chapters. Each chapter title with a brief content is listed here:

Chapter 1. Introduction and background to the use of composite materials in the aerospace industry stating the importance of understanding impact damage and damage tolerance. The objectives are outlined in this chapter.

Chapter 2. Literature review covers low-velocity impact and compression after impact experimental and modelling approaches is presented. Composite failure mechanisms, damage behaviour and structural response of composites under low-velocity impact and compression after impact loading, as well as their influencing factors, are studied through other research available in the literature.

Chapter 3. Damage resistance of carbon-glass laminates in low-velocity impact experiments. The aim of the work presented in this section is to determine the effect of adding GFRP layers to CFRP laminates, which can be proved to improve the damage

resistance properties of the laminates.

Chapter 4. Damage tolerance of carbon-glass laminates in compression after impact experiments. The experimental results show that the hybrid laminates display failure stresses up to 32% greater than CFRP laminates with identical impact energies.

Chapter 5. The effect of ply blocking on near-edge and on-edge impact damage mechanisms. The blocked stacking sequence could contain damage in the middle region of coupon.

Chapter 6. Important conclusions and future works from this research is summarised.

2 Literature Review

This chapter provides an extensive literature review on low-velocity impact of composite structures and relative modelling methods. The aim of this literature review is to bring the current and past research outcomes together to understand the behaviours of damage modes and the interaction in low-velocity impact and compression after impact. This review covers the failure behaviour of laminated CFPR under low- and high-velocity impact and its damage tolerance performance under compression after impact. The major influencing parameters affecting the damage behaviour of composite laminates during experimentation are reviewed. The behaviour of BVID, such as intra- and inter-laminar damage in the form of matrix cracking and delamination has been drawn huge attentions to research, which is also covered in this chapter.

2.1 Laminated Composite

Damage resistance and damage tolerance of composite material mostly depends on the properties of fibre and matrix and the bond between them. After years of development, many types of fibre with a wide range of mechanical properties are available for structural applications. Among these various fibre types, those of carbon, glass, and Kevlar are frequently utilised and were also the earliest composites applied to commercial aircraft. These fibres are embedded within epoxy resin to form fibre reinforced polymer composites in structural applications. Carbon fibre has the excellent modulus and strength but is brittle. Glass fibre has outstanding strain to failure ratio but is not as strong as carbon fibre. These mechanical properties, especially strength performance, are directly proportional to the damage resistance of composites [1]. It was observed that carbon and glass composites with higher failure strength outperformed composites with same type of reinforcement but lower failure strength in low-velocity impact tests [2–4].

Planar 2D woven fabrics, considered as an alternative to unidirectional (UD) forms of reinforcement, provide continuous fibre reinforcement and are characterised by balanced and equal properties in transverse and longitudinal directions. But they have relatively lower mechanical properties than UD reinforcements as a result of fibre

crimping. In addition, the inter-laminar fracture resistance of 2D woven composites is more advanced, since the interleaved structure creates stress concentrations, which makes the delamination is difficult to propagate compared to UD composites [5].

3D woven and stitched composites offer advantages in impact performance and damage tolerance by placing z-binder reinforcement in the through-thickness direction. This directly suppresses the formation of delamination [6,7].

Carbon-glass hybrid and fibre-metal laminated composites, such as those using glass/carbon fibre and aluminium alloy sheet/glass fibre, bring together the advantages of both and have received much research attention for low and high velocity impact analysis [8–10]. It was shown glass/carbon has less notch sensitivity and better post-impact compressive performance when compared to carbon-only or glass-only composites [8]. Composites with reinforcement forms other than continuous fibres are not able to provide strong damage resistant or damage tolerance properties, and they do not usually have any structural applications.

Matrix plays an important role in composites laminates. It is for transferring loads to the reinforcements and protecting the reinforcements from surrounding environment. Mechanical properties in the transverse, through-thickness, in-plane, and inter-laminar shear directions in laminated UD composites are predominately determined by the matrix system [11]. Another important property of matrix is fracture toughness (i.e. critical energy release rate). Fracture toughness is crucial when considering the selection of the composite material system for impact and fatigue resistance in aerospace applications. This is one of the critical driving parameters for the propagation of matrix-dominated failure (delamination and matrix crack) and profoundly affects the performance of composites under transverse and fatigue loadings [11–14]. Therefore, desirable matrix systems for aerospace applications should show high stiffness/strength and high fracture toughness. Common resin systems that are frequently applied in the industry are thermosets and thermoplastics (e.g. polyether-ether ketone (PEEK)) [15].

In this research, laminates are fabricated from high strength unidirectional HTA/913C carbon fibre and GE5/913 glass fibre impregnated with toughened 8552 epoxy sheets from Hexcel^{TM}. This material system is a high-performance aerospace grade composite

and is widely used and studied across the industry and academia.

2.2 Impact Types

Impact can be categorised by different perspectives, such as impact velocity from high to low, impactor mass from large to small, damage level from non-penetration to full penetration, impact energy from high, inter-medium to low and impact behaviour of the substrate (quasi-static or localised response) [13,18,21,22].

Based on the relative velocities of the impactor and the laminate, impact is generally divided into 3 types. Hyper-velocity impacts involve impactor-laminate velocity differentials in the order of 30-70km/s, resulting in near instant vaporisation of the target [28]. These types of impact are typically only seen in satellite and spacecraft applications. Ballistic impact is defined for relative impact velocities of 70-2000m/s. Due to the short contact period involved, the structure does not have time to respond in global or flexural shear modes. The applications have focused on preventing penetration for armour plate and blast resistance [29]. Low velocity impact refers to those with relative impact velocities smaller than 70m/s, giving rise to impact energies up to 50J [30]. Impacts in this type can result from a wide range of scenarios, from dropped tools during manufacture or maintenance, to bird strikes during aircraft take-off. Despite the low energies involved, the resulting damage can be extensive and is mainly internal, making it hard to detect on the surface and causing the phenomenon of BVID. This is a major problem for the aerospace industry in particular, since the laminate strength can be affected by up to 70%. Due to this major concern, the safety of employing composites is critical, this type of impact damage has been extensively researched in past three decades.

2.3 Quasi-static Loading

At low velocities, laminate response is dominated by the lowest mode shape, meaning that load, deflection and strain are effectively in phase. For this reason, it is possible to approximate low velocity impact by quasi-static loading. This has numerous advantages, from both a modelling perspective and a practical perspective, as quasi-static tests are easier to conduct and are more repeatable than impact tests.

The limits of the quasi-static approximation have been well researched. Kaczmarek and Maison [31] developed the work by Swanson [32] to define the quasi-static limits, proposing a mass criterion that the impact could be considered quasi-statically if the impactor mass was at least ten times the lumped plate mass. A review study by Nettles and Douglas [33] summarises the previous research on this topic, as well as performing some original tests comparing impact to quasi-static indentation, across a wide range of laminate layups and support conditions. They conclude that when impact and quasi-static indentation are compared based on the maximum transverse force experienced, load-displacement behaviour and delamination area are similar.

2.4 Impact Damage

2.4.1 Matrix Cracks

Unlike metallic structural, laminated composites barely leave any obvious indentation on their external surface after impact, but BVID may significantly degrade the loadbearing capability under further loading, especially compressive and fatigue scenarios. Due to the nature of laminated composite, non-critical damage usually initiates under impact loading at stress levels much lower than the fibre failure strength. It is well known that the most common internal damage modes caused by low velocity impact at a macroscopic level are matrix crack and delamination [34-39].

During an impact event, the laminate is subject to a complex loading condition, which causes compression at the top, tension at the bottom, inter-laminar shear stress within, and immediate contact stress under the impactor. Matrix cracking is recognised as an early damage mechanism before delamination, after which the stress is redistributed and concentrated at the locations where the matrix cracks intersect with resin-rich regions at the adjacent ply interfaces. Because of the developed inter-laminar shear stresses and the relatively weak mechanical properties of the matrix, delamination initiates from these matrix cracks. Since the matrix cracks are unable to penetrate adjacent plies with a different fibre orientation, they tend to migrate from one ply to another by joining together via delamination at the interfaces [40,41]. As the load increases, delamination growth at pre-existing locations and the occurrence of fibre breakage results in the load-bearing capability of the laminate being completely disrupted. Therefore, non-critical damage mechanisms and coupling phenomena

between matrix cracks and delamination before critical failure becomes extremely important for the study of both impact damage resistance and damage tolerance.

BVID, as previously described, is considered to be the most dangerous type of damage to laminated composites. Many researchers have studied failure evolution and damage mechanisms in laminated composite material under localised impact loading. Based on the nature of laminate composites, the damage mode and failure mechanism are characterised as following:

Matrix cracking or intra-laminar damage takes place within a ply in the form of shear cracks and transverse cracks running along the direction of the fibre when a laminate is under transverse loading. Matrix cracks and fibre matrix debonding, as the initial damage modes in composite under transverse loading, occurring at an early stage of impact and static indentation due to the relatively weak mechanical properties of the resin. It is also the first form of damage in laminates under other loading conditions such as cyclic, tension, and compression loads [42-46]. Unlike delaminations, matrix crack remains undetectable under NDI methods, e.g. ultrasonic inspection. The occurrence of matrix cracking does not significantly affect the transverse stiffness of the laminate and its residual properties [47]. According to Takeda et al. [48], the association of matrix crack to delamination formation was observed for the first time in cross-ply glass/epoxy laminates by a scanning electron microscope (SEM). The authors found that matrix cracks act as the precursor to delamination formation and occur well ahead of delamination cracks. Some years later, Joshi and Sun [49] reported a similar observation and explicitly explained the different roles of transverse and shear cracks.

Choi et al. [50-51] performed experimental and analytical studies on a series of cross ply and quasi-isotropic laminates subjected into point and line impacts, and they observed that shear cracks occur at the region where high inter-laminar shear stress is present in the laminate and are inclined at approximately 45^{o} to the impact direction. This high inter-laminar shear stress originates from the contact load and bending deformation of the laminate during impact. Transverse cracks or vertical cracks are normal to the fibre direction and are incurred by in-plane normal stresses exceeding the transverse tensile strength of the bottom ply due to flexural deformation. Because the

transverse cracks usually occur at the bottom ply in laminate under bending load [52,53], they are also called bending or tensile cracks.

2.4.2 Delaminations

Delamination (inter-laminar failure) takes place at the resin-rich regions between neighbouring plies, usually happens on dissimilar fibre orientation. No delamination is usually be found at the interface between plies with the same fibre orientation [54-57]. Delamination as the most common and dangerous damage mode caused by the high inter-laminar shear and normal stresses exceeding the strength level of the interface. It takes place at holes [68], free edges [59,60], and ply drop [61], and also can also be caused by thermal loading in the curing process [62]. A significant amount of research has been performed using detailed mapping of impact delamination shape, size, and the correlation with other parameters i.e. orientation of neighbouring plies, matrix cracks, and impact energy [63–68].

The occurrence of delamination can be explained by the fact that a laminate consists of different orthotropic layers. Under flexural deformation as the result of concentrated transverse loading in the through thickness direction, each ply with different fibre orientation tends to deform differently due to the bending stiffness and bending-twisting coupling effect. Out-of-plane and shear stresses are therefore developed at the interface between plies with different orientations. As the flexural deformation increases, these inter-laminar stresses increase too and exceed the critical values, causing delamination to take place. Lesser and Filippov [69] presented a simple explanation of delamination between two layers using a Navier solution. The two layers were not bonded together during concentrated loading. It was found that the difference in displacement of the two layers had a similar shape to delamination.

Although delamination as a type of BVID is difficult to inspect, it can be observed by analysing the force history plot. If performing impact testing on a given laminate with incremental energy, the response of the laminate for low energy impact shows a smooth half-sine wave under lower energy levels. Once the impact energy exceeds a critical level then multiple load drops can be observed. This critical energy is called the delamination threshold energy, which is defined as the least amount of impact energy

required to induce delamination. The force level corresponding to the load drop is called the critical load (F_C), which is governed by the flexural rigidity and critical energy release rate of the composite [70,71]. This process can also be thought of as a drop between two different response states. For low energy impact, where the energy is below the delamination threshold energy, and the maximum load during impact is lower than the critical load, the laminate presents a low energy response state. For high energy impact, where the impact energy is higher than the delamination threshold energy, the impact force history follows a high energy response state, and once the F_C is reached, delamination degrades the local flexural stiffness of the laminate and lower velocity of the impactor, leading to a drop to the lower energy response state [72].

2.4.3 Surface Dent

Permanent surface indentation (dent) together with back face (un-impacted surface) bulge is the damage that occurs to the surface of the structure under out-of-plane loading. They are also referred to as the impact 'footprint'. In general, the dent depth is sensitive to impact energy and strongly dependent on the laminate thickness. Possible explanations for such a phenomenon could be the highly localised Hertzian contact stresses at the loading point, fibre failure due to compression near the impact site, and plasticity or crushing of the matrix beneath the impactor.

Dent depth is usually used for correlating the residual compressive strength with damage developed during transverse loading in the literature [73-78], and it is also a crucial indicator in most inspection protocols for identifying BVID damage and damage tolerance evaluation in aerospace composite structures.

The formation of permanent indentation is a complex process. It cannot be analysed in isolation and must be studied with many parameters and involves other damage modes i.e. matrix crack, delamination, and fibre failure. In addition, the recovery of the residual dent depth due to the viscoelastic phenomenon, known as relaxation, is usually observed even without subsequent mechanical and environmental loading after impact [79-84]. Hence, there are few closed form solutions available in the literature to fully explain this phenomenon in detail and to derive the key parameters of this process. Nevertheless, Caprino [85] and Caprino [86] used the test data available in the literature

to develop an empirical analytical solution to predict the indentation dent and its correlation to residual tensile properties, based on the penetration energy of laminates under impact and static indentation. They found the indentation law developed in their study has general applicability and reported that the indentation depth for a given material system is independent of other parameters but varies specifically with the ratio of the impact energy and the penetration energy. The author later improved the previous model into a two-parameter law that only is dependent on the indention energy.

A number of researchers have modelled the permanent indentation using finite element analysis and suggested that the indentation is governed by matrix plasticity and non-linear shear behaviour [45,82,87]. Shi [33,35] and Tan [88] developed finite element analysis models to predict impact damage and captured the permanent indentations. Apart from the prediction of other damage modes, both predictions of dent depth were in good agreement with experimental results. He [82] focused on numerical prediction of permanent indentation using finite element analysis with an implemented elastoplastic formulation incorporating fibre failure. Permanent indentation as a result of high energy impact, accompanied by fibre failure, was very well captured. Bouvet [89], and Abdallah [81], reported the attributes of permanent dent to microscale resin debris formed during cracking that gets trapped between the fracture planes inside the matrix crack. The trapped debris makes it difficult for the matrix crack to return to its original fully closed position, a scenario which has also been captured by microscopic images [39,81]. This observation, together with strong evidence clearly showing the mechanism of creation of permanent indentation, is extremely useful for understanding the damage evolution of impact damage.

2.4.4 Other Damage

Fibre tensile failure is most likely to occur at higher energy impact, which results in fibre breakage due to high tensile stress at the back face of the laminate and compressive fibre failure at the impacted surface under the impactor. When a laminate is under transverse loading, compressive and shear stresses start forming under the impact, which leads to compressive fibre failure on the impacted side. Due to the high bending stresses developed on the back face of laminate as the flexural defamation increases during transverse loading, tensile fibre breakage occurs. This failure mode appears to

occur much later and be less complicated in comparison to matrix cracking and delamination. A considerably larger amount of energy is absorbed in the case of fibre breakage. As a consequence, the load-bearing capability of the composite is significantly diminished, leading to catastrophic failure of the structure. In addition, fibre failure is also considered as precursor of laminate penetration [89].

The compressive strength of ply is normally lower than the tensile strength in most UD composites, and the first fibre fracture should occur where the compressive stress is high [90]. Micro-buckling is another compressive fibre failure mode that commonly occurs when laminate is under compression or compression after impact test [91]. The information regarding the correlation of this damage mode to impact damaged laminate is very limited. For micro–damage i.e. fibre micro-buckling, fibre/matrix debonding, and micro-cracking, which have only a minor effect on impact damage progression and residual mechanical properties [92].

Penetration is usually caused by extreme load being applied to the composite during high-velocity high-energy impact. Textile reinforced composite, woven fabric, 3D braided Spectra® and Kevlar®, etc. are commonly used as high velocity impact resistant material. To reduce the vulnerability of laminated composite to impact damage, numerous academics and engineers have attempted to improve the impact resistance and damage tolerance by matrix and fibre toughening [93–95], hybrid methods [96], through-thickness reinforcement [97,98], and protective coating [99].

2.5 Low-Velocity Impact and Static Indentation

An impact event finishes within several milliseconds, and it is difficult to control and capture the delamination propagation. In fact, damage formation in composites when subjected to transverse point load in quasi-static loading rate is analogous to that incurred by low-velocity impact [81,116–119]. In [48], low-velocity impacts are defined as impacts in which the contact time between the impactor and the plate is long enough to allow all wave reflections from the boundaries. The relationship between deflection and impact load then approaches those of a purely static loading case [47]. Low-velocity impact tests do not allow to observe the succession and evolution of the degradation mechanisms within the plate, since this can only be inspected upon

completion of impact testing. For this reason, a number of researchers have turned their attention to static indentation tests. These tests have been demonstrated to give similar global behaviour and damage states to low-velocity impact tests [39,60,120,121]. Since they are static tests, they can be easily interrupted at different stages to observe the damage evolution within the plate.

Extensive studies can be found in the literature presenting experimental observation for low-velocity impact or static indentation tests on laminated composites. Several of these works are reviewed here to illustrate the existing results and show the motivation for the proposed experiments in this study. In the experiments described in the literature, the plate used is often of a circular or rectangular shape; it is either clamped between two fixtures or simply supported on a steel window. In most cases, quasi-isotropic lay-ups are considered [39,46,102,122], while some works deal with cross-ply $[0_n/90_m]_S$ or $[0_n/45_m]_S$ stacking sequences [104,123].

Although detailed damage morphology shows that no obvious difference can be found between impact-induced damage and static indentation-induced damage, it has been ascertained that the permanent indentation depth caused by the static and dynamic methods are slightly different. Symons [57] compared the overall damage extent and permanent indentation depth of T300/914 cross-ply laminate under static indentation and low-velocity impact and high-velocity impact, and confirmed the strong similarity of damage between static indentation and low-velocity impact. However, the former produces a deeper dent depth than that induced by low-velocity impact under the same incident energy.

2.6 Modelling Low-velocity Impact

Zhang [129] presented an approach to predict the initiation and propagation of damage in composite laminated plates. This work was based on contact constrain introduced by penalty function method. The potential delamination and matrix cracking areas were employed as cohesive zone and the damage process as contact behaviour between the interfaces. The damage evolution law was derived from a damage surface which combined stress based and fracture-mechanics-based failure criteria. The damage model showed in the paper used software ABAQUS and its user subroutine VUINTER.

The numerical results were based on carbon/epoxy laminate plates with stacking sequence $(0_4/90_4)_S$. The model simulated a low-velocity impact and showed a good agreement with experimental observation.

Zou [130] reported a model for progressive inter-laminar delamination for composite laminate structure. A computationally efficient 2D technique was used which modelled the laminated structure was an assembly of sublaminates connected through their interfaces. Constraints between sublaminates were removed to form delamination. A stress-based failure criterion was used to predict delamination initiation. Delamination propagation was using a fracture mechanics approach. In this paper the main intra-laminar damage mode and matrix cracking were also presented. The FE analysis was employed to assess the deformation and the delamination development. The structures modelled in this work included a double cantilever beam, a cross-ply laminate and some filament-wound composite pipes. The results showed a good agreement between predictions and experimental data.

Craven and Olsson [131] presented a finite element model of carbon fibre composite laminate with multiple delaminations of realistic shape. This model also included the fibre fracture cracks which were loaded under compression. The modelling techniques were firstly applied on circular and elliptical delaminations of single ply sublaminates. Then the techniques were applied to models with multiple delaminations of realistic shape and their behaviour in buckling. In this work an inverse method was also used to determine the stiffness reduction caused by the damage and peanut-shape delaminations. The authors concluded that when fibre fracture cracks were added, the stiffness reduction was small but the cracks affected the buckling shapes significantly.

Wimmer [132] analysed delaminations in fibre reinforced laminated composite structure. The numerical simulation of delamination was divided into two parts, the creation of a starting delamination and the delamination growth. The starting delamination was predicted by a stress based failure criterion. The growth of the starting delamination was modelled by Virtual Crack Closure Technique (VCCT). The linear finite element analysis was used to predict the starting delamination. The non-linear analysis was used in the simulation of delamination growth. The work predicted the

maximum bearable load of structure from the simulations of the growth of various starting delaminations. The cohesive zone elements were to verify the simulation procedure.

Li [133] presented the modelling damage due to low velocity impact with neglecting the role of inertia to composite laminate. A mixed mode delamination propagation criterion was employed for modelling delamination propagation. In this model, a simplistic ply-discount technique was used to calculate the effects of transverse matrix cracking. The model was applied to different structures such as quasi-static indentation of filament-wound pipes.

2.7 Compression after Impact

Matrix cracks, delamination, permanent indentation, and fibre failure can be induced during impact. Delamination, from the perspective of damage tolerance, is the most critical damage mode. It effectively separates a laminate into several sublaminates under the impacted region. These sublaminates will propagate and interact with other damage modes upon subsequent continuous in-plane loading. Compared with the residual tensile and flexural performance, the reduction in compressive strength due to BVID is the most significant scenario [110,111]. The presence of multiple delaminations incurred by low-velocity impact or indentation loading in CFRP laminates reduces the flexural stiffness of the laminate due to the formation of sublaminates, which leads to premature buckling and a reduction of compressive strength by up to 60% [112]. Therefore, the low-velocity impact test in conjunction with the Compression after Impact test are often of most interest in the building-block approach for design of composite structures. The damage mechanisms of composites during transverse loading and CAI should be coherently investigated establish the overall damage resistance and tolerance for low velocity impact.

In contrast to the large body of research on laminated composite under low-velocity impact (LVI) and quasi-static indentation (QSI) loading [109,113,114], studies of damage tolerance using CAI tests are far fewer in number, despite CAI strength being one of the governing parameters in composite strength design. Its various failure

mechanisms during local instability, and at the moment of structural failure, are therefore still not fully understood.

Under uniaxial compression, the buckling and failure behaviour of laminated composite with impact damage are strongly influenced by the impact damage extent [115–119] and specimen geometric parameters [112,120,121] for a given material system. Amaro et al. [122] performed compression tests on cross-ply laminates containing different damage extents, and established three different buckling failure modes. They verified that the number of damaged interfaces and size of the damage plays an important role in CAI buckling behaviour.

Studies in the literature have identified an empirical relationship between material properties, the CAI strength, delamination area, and impact energy. Cartie and Irving [115] showed that the CAI strength is a function of impact energy across different material systems and found that the CAI response of delaminated laminates largely depends upon the damage threshold load or the toughness of resin system in the previous impact test. The damage induced below the threshold load under a low energy impact has little or no effect on the overall compressive strength. As the delamination area increases and reaches a critical size, as a result of increasing impact energy, the CAI strength drops significantly and then tends to level off to a point where it is equivalent to a complete perforation at the delaminated region [60,95,103]. Thick laminates, which have a width-to-thickness ratio lower than 50, have been studied with the help of deflection sensors that measure the out-of-plane deformation, and strain gauges measuring local in-plane strain. It is believed that the compressive failure process in these laminates usually starts with appearance of local buckling at the delaminated region and then develops in a direction perpendicular to the loading until the structure collapses [41,88,104]. These CAI tests are usually conducted in conjunction with standardised testing procedures and compression fixtures recommended by companies or organisations such as NASA, Boeing, CRAG, SACMA, and ASTM. According to these test methods, specimens with impact damage introduced either by drop-weight impact tests or static indentation are required to be positioned into a compression rig with simple supports and clamps applied to the edges of the specimen. This positioning effectively prevents global buckling and results in

preferable failure originating at the damage region.

Studies on the compressive failure of either thick or thin laminate without any anti-buckling mechanism which contain either actual or artificial delamination have been given considerable attention. The validation of analytical models developed for residual strength prediction provided that the delamination is artificially embedded at single or multiple interfacial locations in order to simplify the complex impact-induced delamination [130–133]. The influence of delamination buckling progression and other factors such as the number and depth of artificial delamination is significant to the global and post- buckling behaviour of laminate. Recently, Pérez et al. [134] presented systematic comparative experiments on the CAI properties of laminates with actual delamination induced by transverse loadings and laminates with an embedded single artificial delamination. It was found that single artificial delaminated plate - irrespective of the embedded location - overestimated the residual compressive strength compared to that obtained by real impact delaminated plate, especially as the delamination area increased. In contrast, Zhou and Rivera [135] summarised a deformation sequence of compressive and buckling behaviours of thin laminates with artificial delaminations at different locations and demonstrated that the compressive behaviour of laminate with artificially embedded delamination was helpful to understand and characterise the response of impact damaged laminate under compression.

When a composite plate is under transverse loading in either a dynamic or a quasi-static case, the plies near the impacted surface under the impactor exhibit a high in-plane compressive stress and Hertzian contact stress, potentially resulting in compressive failure of CAI load-bearing 0^o fibre plies at the front surface if the central deflection is large. These surface fibre cracks, together with strong geometric imperfections that are the dent and bulge at front and back face, can lead to crack propagation due to fibre fracture and local buckling towards the previous transverse loading direction [129]. More recently, the same authors [41] performed the CAI experiment with micro-focus x-ray computed tomography scanning offering highly detailed information on the damage progression during CAI. It was observed that a compressive crack near the front surface 0^o fibre plies caused by previous impact propagates perpendicular to the loading direction under compression, causing stress redistribution in 0^o plies, which contributes

to the residual compressive strength reduction.

In a standard CAI test [129], in order to ensure the alignment of the specimen and collect the in-plane stress-strain response and out-of-plane displacement at multiple points within the specimen, strain gauges, linear variable differential transformers (LVDTs), and dial gauges are usually required to be attached directly to the specimen's front and back surfaces [117,141,142]. These requirements permit deformation histories of multiple points to be obtained and the buckling modes and compressive behaviours to be predicted based on these readings. However, information outside of the predefined point/region is simply neglected. These regions where measurement is not taken could be equally important and useful for studying CAI failure mechanisms and for modelling validation. The 'contact' and 'point' displacement or strain measurement techniques, such as those mentioned above, and frequently used laser displacement sensors are not sufficient to capture the full-field deformation of the specimen during plate buckling, and the failure progression at the moment of structure rupture. A 'non-contact' full-field measuring approach that has been applied to CAI testing is the moiré interferometry technique, which is able to capture the out-of-plane deformation with a high degree of accuracy [110]. Another full-field measurement technique that has been frequently applied to mechanical testing in recent years is Digital Image Correlation (DIC) system. This system offers the measurement of in-plane and out-of-plane displacement fields at the surface of the objects under any mechanical loading. And the DIC technique is based on comparisons of images taken consecutively by the DIC cameras at different load steps [143]. He et al. [144] and Rhead et al. [145] used DIC system for characterising the shear properties of the composites and studying the buckling performance of the post-impact hybrid composite laminates, respectively, and the results were found reliable and easy to be couple with finite element model validation.

2.8 Experimental Preparations for Low-velocity Impact

2.8.1 Testing Device

In order to find out the mechanism from the foreign object impact event, numerous impact tests have been conducted during the past half century. Impact energy is usually taken as a control variable for characterising the different impact response and damage, and identical impact energy level can be achieved by large-mass low velocity impact or

small mass high-velocity impact. However, the resultant damage and substrate response as the result of these two impact events can be quite different. Therefore, this needs to be considered when selecting the impact test instrumentation. It is also important to understand the strain rate regime which the studied material will be subjected to, and the strain-rate sensitivity of the material under test. The objective of experimental investigation of an impact event is to simulate the exact loading environment of actual foreseeable impact events under controlled conditions. Gas guns, drop-weight impact testers, cantilevered impactors, and pendulum-type testers are the most frequently used instrumented impact testing methods in the literature [13, 18, 22, 40, 75, 100].

2.8.2 Impactor

Typical impactor shapes for low-velocity impact study are hemispherical, flat-ended and conical. The effect of impactor mass on the response and damage formation of the substrate has been introduced in previous sections. For a given impactor mass, various impactor shapes can lead to completely difference responses and damage modes. It is therefore of great importance during experimental investigation. Mitrevski [101] extensively studied the effect of various impactor shapes on low-velocity impact damage and the response of carbon fabric/epoxy laminates. They found that, under the same impact energy, the highest energy absorbed by the specimen and the largest indentation/penetration damage was caused by a conical impactor. The hemispherical impactor gave the highest delamination threshold load, the greatest peak force (i.e. the shortest contact duration), and the largest delamination area. From this study, it can be deduced that the reason for the hemispherical impactor being most frequently used in low-velocity impact tests is that it creates the largest delamination area without causing significant surface damage. This is close to the definition of BVID. For the design point of view, the damage induced by a hemispherical impactor is large and thus is more conservative for use in design. Hence, impact damage created by other impactors is not a major concern of this work.

2.8.3 Laminate Thickness

Laminate thickness can be treated as the fundamental parameter affecting impact response and damage propagation. Studies have shown that the damage initiation in cross-ply laminates relies upon the thickness of the laminate [106], and the flexural

stiffness of plate. It is given that the initial failure occurs in thin flexible laminate at lower plies. For thicker and stiffer laminate, the initial failure was on the top surface due to contact stress. From either the equation of dynamic response of plate or flexural rigidity of a homogenised composite plate, it is easy to distinguish that the response of plate under transverse loading is closely related to the third power of the plate thickness. Therefore, plate thickness governs the linear elastic region of the plate response under transverse loading until damage takes place.

2.8.4 Boundary Conditions & Curvature

In most current experimental studies the laminate is either placed under simply supported or fully constrained boundary conditions. The former case allows more deflection and energy to be transferred during impact compared to the latter. The fully constrained boundary condition often has two supporting plates with a circular opening at the centre of both, and the laminate is sandwiched between the two clamped windows. This test configuration is beneficial for analytical solutions [107–110] since the plate is circular with a cantilever boundary and therefore presents an axi-symmetric analytical condition. In actual aircraft structural applications, the lower composite fuselage and composite wing lower skin are exposed to debris impact during take-off and landing and are under tension and compression. The correlation of damage and impact response between pre-loaded and unloaded laminate under low-velocity impact has to be made in order to understand the effect of pre-load. It has been observed that the pre-tension stiffens the laminate and results in high peak load and lower maximum deflection compared to un-loaded laminate under low-velocity impact [111]. Because the transverse deflection increases the instability of a laminate under compression, laminates under pre-compression exhibit larger deflection and in turn more energy is absorbed, thus creating larger damage than un-loaded laminates. But, Chiu [112] reported that the peak impact force are pre-tension, un-loaded and pre-compression specimen in decreasing sequence. In fact, both pre-loading conditions decrease the impact resistance of unloaded laminate [111–114]. In addition, low-velocity impact on the edge of the laminated composite is also one of the major concern for industry [115].

3 Damage Resistance of Carbon-Glass Laminates in Low-velocity Impact Experiments

3.1 Introduction

The hybridization of laminates aimed at reinforcing resistance to BVID formation and the damage tolerance properties of laminates include adding aramid interlayers to CFRP laminates to enhance the delamination resistance of the laminate [17, 18] and using GLAss-REinforced Fibre Metal Laminates (GLARE) [19] which have entered service in the Airbus A380.

The aim of the work presented in this section is to determine the effect that adding GFRP layers to CFRP laminates, which can improve the damage resistance properties of the laminates. GFRP layers are cheaper and less dense than CFRP layers and have been added to carbon fibre helicopter blades [20] where their non-serious failure mechanism was seen as an advantage for compressive failures where damage was not a factor. Here it is considered that this mechanism may lead to induced impact damage drawn into deeper position through thickness. The deeper the delaminations located, the thicker the sub-laminas are, which requires more energy to bulk the sub-laminas. The corresponding failure stress will be improved in CAI. Hence, the influence of stacking sequence and both position and number of glass layers on hybrid laminate damage resistance is crucial to improve damage resistance and damage tolerance, which is important to conduct investigations.

A range of laminates, which have been subject to out-of-plane impacts with various energies, have been assessed experimentally using NDI methods to exam the formation of impact damage and investigate the influence adding GFRP to improve damage resistance. CFRP laminates with a stacking sequence that has already been identified as being damage tolerant [22] are used as comparative baselines.

3.2 Experimental Methods

3.2.1 Laminate Manufacture and Stacking Sequence Selection

Hybrid CFRP/GFRP specimens are manufactured from carbon (HTA/913C) and glass

(GE5/913) pre-preg layers with material properties given in Table 1 and stacking sequences given in Table 2. Three full CFRP specimens are made, two are manufactured from HTA/913C and the third manufactured from AS4/8552 material.

Material	E_{11} (GPa)	E_{22} (GPa)	G_{12} (GPa)	ν_{12}	t (mm)	G_{IC} (J/m^2)
GE5/913 (glass)	43.9	15.4	4.29	0.28	0.142	225
HTA/913C (carbon)	135.0	18.5	4.97	0.29	0.134	225
AS4/8552 (carbon)	128.0	10.3	6.0	0.30	0.125	261

Table 1 *Material properties (t is cured layer thickness).*

Laminate ID - Impact energy	Lay-up (C1=AS4/8552, C=HTA/913C, g=GE5/913)	E_{xx} (GPa)
CC_1-8J	$[(\pm 45_{C1})_4/(90_{C1}/0_{C1})_4]_S$	51
CC_2-18J	$[(\pm 45_C)_4/(0_C/90_C)_4]_S$	55
CC_3-18J	$[(\pm 45_C)_4/(0_C/90_C)_4]_S$	55
H_1-12J	$[45_C/-45_C/0_C/0_g]_{4S}$	55
H_1-15J	$[45_C/-45_C/0_C/0_g]_{4S}$	55
H_1-18J	$[45_C/-45_C/0_C/0_g]_{4S}$	55
H_2-12J	$[\pm 45_C/45_C/(\mp 45_g)/-45_C/\pm 45_C/(0_C/0_g)_4]_S$	55
H_3-12J	$[(\pm 45_g)_2/(\pm 45_C)_2/((0_C)_3/0_g)_2]_S$	65
H_3-18J	$[(\pm 45_g)_2/(\pm 45_C)_2/((0_C)_3/0_g)_2]_S$	65
H_4-8J	$[(\pm 45_C)_4/(0_C/0_g)_4]_S$	55
H_5-8J	$[(\pm 45_C)_4/(0_g/0_C)_4]_S$	55
H_5-12J	$[(\pm 45_C)_4/(0_g/0_C)_4]_S$	55

Table 2 *Impact energy, stacking sequence, theoretical axial modulus E_{xx}.*

In the various hybrid (H) laminates, H_1 had a conventional, homogeneous lay-up which is widely used throughout the aerospace industry as it is suited to ensuring surface and ply continuity across thickness variations during manufacture due to the ease with which ply-drops can be made. All other laminates used variations of a damage tolerant stacking sequence [22] where the variation is a function of the through-thickness placement of GFRP layers. The key principle followed in the damage tolerant laminate design was the placement of less stiff ±45° plies towards the outer surfaces of the laminates to protect a central core of load carrying 0° plies from local buckling and hence delamination propagation.

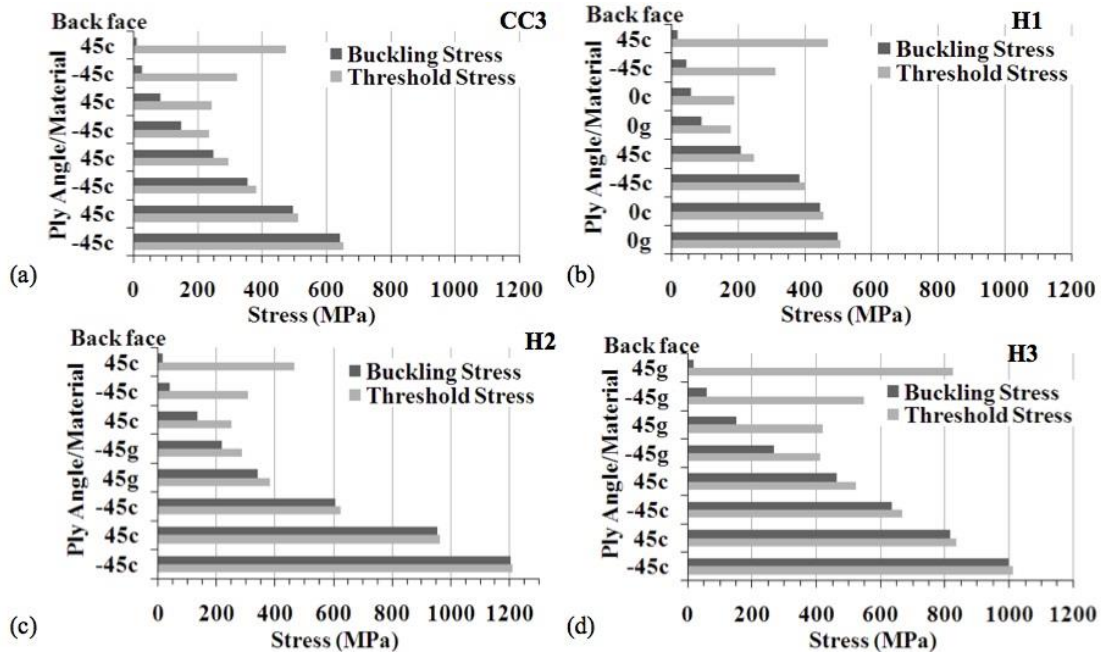

Figure 1 *Plots of theoretical buckling stress and threshold stress for individual layers assuming a 30mm circular delamination at each interface for stacking sequences (a) CC_3, (b) H_1, (c) H_2 and (d) H_3.*

Figure 1 shows plots of theoretical buckling stress σ_C and threshold stress σ_{th} (the stress below which delamination propagation as a result of local buckling will not occur) on a layer by layer basis constructed using the Strip model [23]. A 30mm circular delamination was assumed at each interface and it can be seen that the damage tolerant stacking sequences (Figure 1 (a), (c) and (d)) have higher threshold stress than the homogeneous sequence (Figure 1 (b)). This effect is particularly magnified for the H_3 sequence which has GFRP $\pm 45^o$ outer layers. In addition, hybrid H_3 specimens were designed to increase the probability of damage detection by improving impact damage visibility for a given impact energy. This was achieved by placement of glass layers on the outer surface of the laminate.

The specimens were made using Hexcel GE5/913 GFRP, HTA/913C CFRP and AS4/8552 CFRP unidirectional carbon fibre pre-impregnated (pre-preg) sheet with 0.125 mm nominal cured ply thickness. The composite plates (from which several specimens were cut) were fabricated by traditional hand lay-up. Pre-preg sheet with predefined dimensions were stacked together with specific fibre orientations. Consolidation vacuum was applied to each stack of four pre-preg sheets during laying-up in order to minimise the occurrence of trapped air between pre-preg sheets. The

consolidated laminates were then cured by autoclave using the manufacturer's recommended curing cycle. The basic mechanical properties of GE5/913 GFRP, HTA/913C CFRP and AS4/8552 CFRP lamina are listed in Table 1. The cured composite plate was then cut to the required specimen sizes.

3.2.2 Low-velocity Impact Test Configuration

A number of hybrid laminates were subjected to low-velocity impact tests, using an Instron Dynatup 9250 HV drop-weight impact tower as Figure 2 shows with an impact weight of 6.35 kg. A supporting window was used in low-velocity impact tests. A 16 mm diameter hemispherical impactor was used to impact specimens clamped over a 75 mm x 125mm test window (the long edge being aligned parallel to the 0˚ fibre axis) as prescribed by ASTM standard D7136/D7136M-07. Test data is acquired from a single accelerometer located on the impactor. A velocity sensor, which is responsible for recording initial impact velocity (i.e. the velocity at the point of contact between impactor and specimen) and activating the secondary impact stopper, can be positioned at different heights depending upon the thickness of the specimens. Therefore, a trial velocity test prior to each impact test is required.

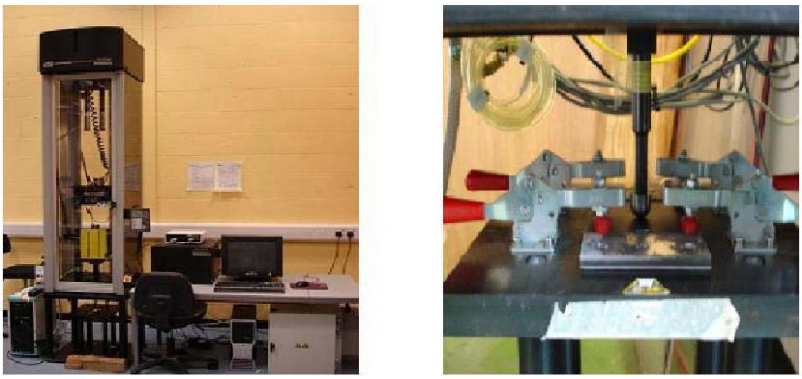

Figure 2 *Instron Dynatup 9250 HV drop-weight impact tower with an impact weight of 6.35 kg. Specimens clamped over a 75 mm x 125 mm test window.*

To commence the impact test, the impactor is released from a pre-determined height, depending on the impact energy required, and it accelerates through gravitation. When contact is established with the specimen, the impactor decelerates and the data is recorded from the accelerometer. The velocity, deflection, and energy are derived by integrating the acceleration of the impactor. It important to understand the constituents of the energy level produced by the impact tower and to determine the amount of energy

for creating damage. In the following section, the absorbed energy and energy for damage creation is compared between the dynamic impact and static indentation tests for given damage areas.

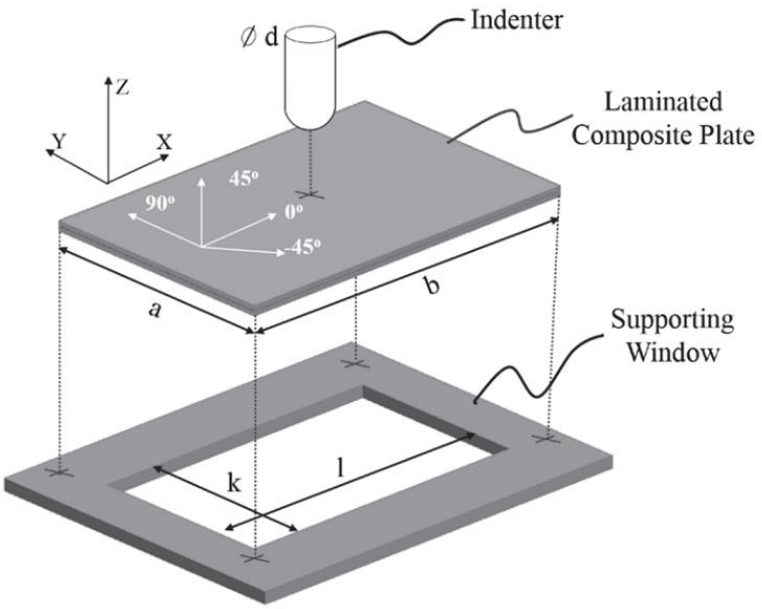

Figure 3 *Schematic of low-velocity impact and static indentation test environment.*

An American Standard Test Method (ASTM) test configuration for low-velocity impact was used to conduct impact test. The specimen were supported on a 75×125 mm window with four rubber-tipped clamps. A schematic of the overall test setup is presented in Figure 3.

In order to describe and understand the relationship between the different occurrences of damage mechanisms, extensive Non-Destructive Inspection (NDI) was carried out in this experimental study. This included ultrasonic C-scan for overall damage mapping and X-ray Computed Tomography (CT) scanning for full 3D damage interpretation.

3.2.3 Ultrasonic C-scan

The composite specimens were scanned using an ultrasonic C-scan before conducting CAI to locate the delaminations caused in impact. Images of the internal damage were produced for the purpose of comparing the damage size and delamination morphology for post-buckling analysis.

The success of ultrasonic inspection is dependent on the orientation of the specimen. Assessment of damage through the hybrid carbon-glass laminates proved difficult since C-Scans were interfered by undesirable signal noise. It is believed that this was caused by the variation of density of CFRP and GFRP. However, it was found that inspection of the delamination can be achieved by scanning individual interfaces. By adjusting signal range, the delamination located in individual interfaces can be picked up and added together to form an overall delamination inspection. This technique will be used extensively throughout the remaining experimental programmes.

When the ultrasonic probe passes over an unbroken area, there is no reflection and the wave front travels through entire specimen. The reflected signal is not scattered so there is delamination detected in this area. When ultrasonic probe passes a delaminated area, the wave reflected back to indicate a strong signal and forming the size of delamination on monitor. A range of spectrum is used to indicate individual depth of the delaminations. All specimens were inspected before testing to ensure quality and generate a reference image for those subjected to the impact.

The scanning speed was 10mm/s and the transverse step size 0.1mm. The scanning window (region of interest) was 35mm square. This was centred on the overlap region and allowed an additional 5mm boundary on each side. The gain was set at 20dB to ensure a strong signal was reflected from the interface.

3.2.4 X-ray Computed Tomography (CT)

Use of X-ray Computed Tomography (XRCT) to investigate damage morphology has previously been constrained to post-test analysis of unloaded specimens. As delaminations and intra-ply cracks close when load is removed, a limit is placed on the information available for identifying mechanisms causing resin and fibre fracture. Here, a newly developed loading stage, for in-situ XRCT imaging of laminates under quasi-static impact loading, is employed to visualise the mechanisms that drive the formation of damage morphologies. Multiple X-ray CT scans taken at increasing indenter displacements reveal the evolution of damage morphology.

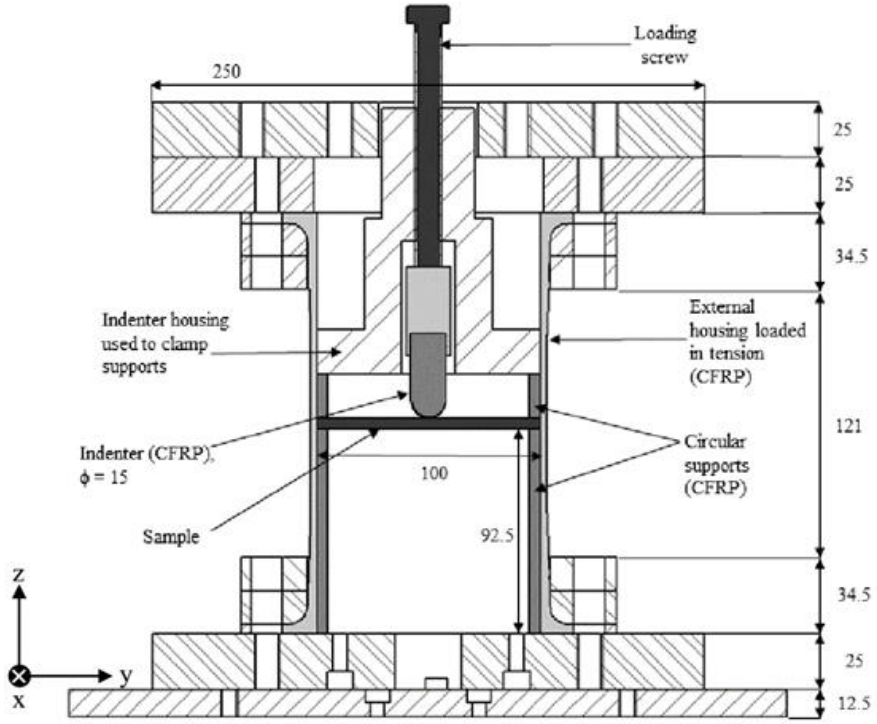

Figure 4 *Cross-section of the loading stage with a horizontal circular specimen for front impact.*

Figures 4 shows cross-sections of the purpose built quasi-static loading stage as adapted for in-plane. The loading stage comprises an impactor, clamped specimen supports and load cell as its major parts. The housing (outer tube) and the impactor are made of CFRP making them relatively transparent to X-rays.

The CFRP supports shown in Figure 4 are contained within a concentric CFRP tube. Both the supports and tube are 5mm thick. The CFRP housing is bounded by steel plates on both ends. In the out-of-plane impact configurations, axial compressive load is applied to the support rings by the internal impactor housing, creating a clamped boundary condition around the circumference of the specimen. For the in-plane impact configuration, rings are swapped for semi-cylindrical supports. These are slit along their vertical axis in order to provide out-of-plane support to the rectangular specimen required for the in-plane impact.

In the zero load position, the impactor sits on the top edge of the specimens as shown in Figs 4. To create a quasi-static impact load the impactor is driven into the specimens using the loading screw that extends beyond the top steel plate. When a load is applied,

the reaction force on the impactor pushes the loading structures away from each other creating a tensile reaction load in the external CFRP tube.

The loading screw is used to apply incremental increases in indenter displacement. Each displacement is held for 255 minutes, the time required to XRCT scan the sample. In order to determine the order of damage progression, all specimens were scanned under zero load and then at two further indenter displacements. The vertical displacement being measured using XRCT data. It is noted that there was no evidence of rigid body movement of the sample relative to its fixture during scanning and that the loading stage remained locked in position in the XRCT scanner throughout all applications of load. Displacement was halted after either initial audible cracking or, for the second displacement stage, after extensive audible cracking. XRCT scans were taken prior to loading and at the end of each displacement phase using a Nikon XT H 225 ST CT scanner with a Tungsten target and Perkin Elmer 1620 16-bit, 2000 by 2000 pixel detector. The system has a 225kV microfocus source with a minimum 3μm spot size. 3600 projections were taken per scan with each projection being a composite of the average of 4 images. Images were taken with 708ms exposures under x-ray conditions of 140kV and 242 μA. To improve the signal to noise ratio, the loading stage was inclined at approximately 7.5° for circular and semi-circular samples. This minimised the number of projections in which X-rays must travel through the full diameter of the specimen. After reconstruction, scans were processed using Avizo Fire 8.0 visualisation software [19].

3.3 Impact Results

Specimens were subjected to single 8, 12, 15 or 18J out-of-plane impacts at their centre using impact test machine with a 16mm diameter impactor. During impact, specimens were clamped over a 75x125mm test window (the long edge being aligned parallel to the 0^{o}fibre axis) as prescribed by the ASTM standard [24]. The BVID was measured using an ultrasonic C-scan system, see Figure 5

Laminate ID.	Non-impact face	Interface number								
		1	2	3	4	5	6	7	8	9
CC_1-8J		-	13	(13)	15	11	10	20	16	37
CC_2-18J		-	16	-	-	-	-	20	-	-
CC_3-18J		-	11	-	16	-	-	44	37	38
H_1-12J		-	(26)	-	-	20	31	29	-	-
H_1-15J		-	33	-	-	(30)	30	-	30	-
H_1-18J		-	21	-	-	(30)	-	-	34	-
H_2-12J		-	-	-	-	42	49	45	-	-
H_3-12J		-	-	-	-	-	-	13	57	54
H_3-18J		-	-	-	-	-	-	50	60	57
H_4-8J		-	-	-	-	-	-	32	35	37
H_5-8J		-	-	-	-	-	-	33	37	36
H_5-12J		-	-	-	-	-	54	-	59	50

Table 3 *Diameters of circles (in mm) containing delamination damage at individual interfaces as defined by C-scans of each specimen. Maximum diameters are underlined. Circles indicate interfaces at which local propagation was predicted by the Strip model.* "-" implies little or no delamination damage.

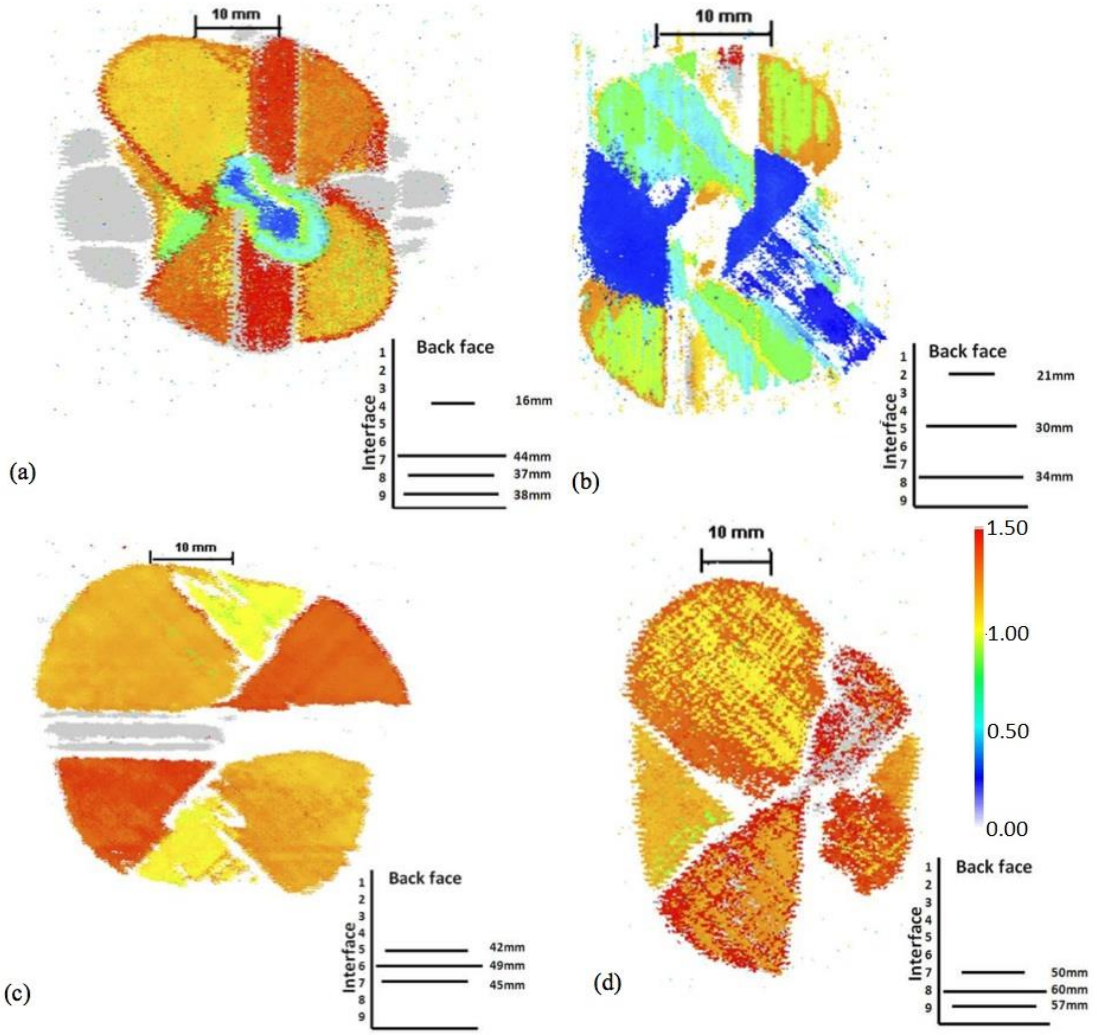

Figure 5 *C-scan images of delaminations caused by impact in (a) CC_3-18J, (b) H_1-18J, (c) H_2-12J and (d) H_3-18J laminates. Delamination colouring indicates distance of delamination from the back face and is consistent across images. Insets show the maximum diameter of a circle that contains the full delaminated area for each delaminated interface. In each the 0°fiber axis is vertical.*

The following Table 3 gives the diameter of circles containing delamination at individual interfaces in the experimental laminates for the first nine interfaces from the back face. This provides a delamination diameter for all interfaces at which local-buckling and hence delamination propagation could possibly occur. Note that the largest delamination for specimen CC_2-18J had a diameter of 41mm and occurred at the 12th interface. Impact energies associated with the delamination distributions are noted in the laminate ID in Table 3.

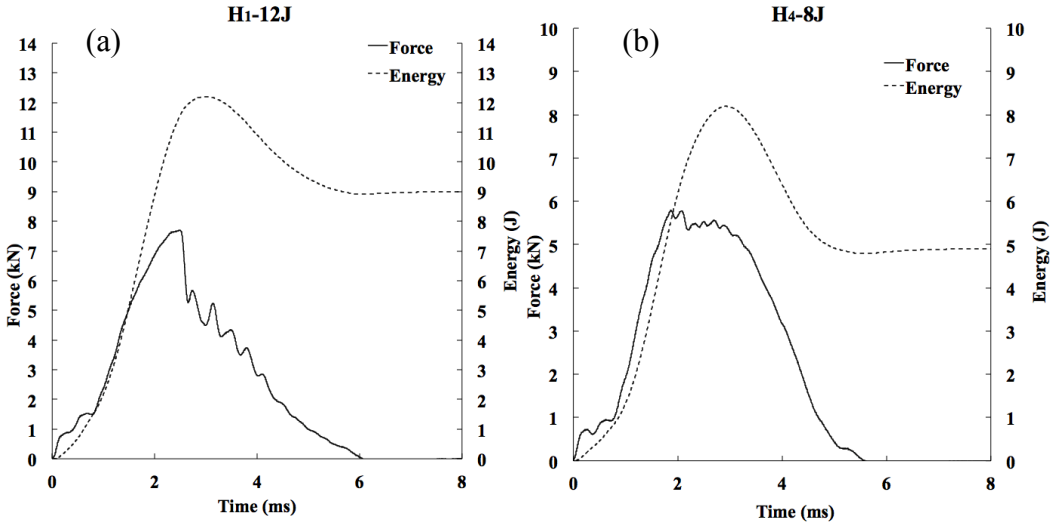

Figure 6 *Typical responses of the force and the energy of the specimen H_1-12J (a) and H_4-8J (b) in impact tests.*

Figure 6 shows the responses of force and energy of specimen H_1-12J (a) and H_4-8J (b) in impact tests. For H_1-12J, the force peaked at 2ms and immediately decreased to zero but in contrast to H_4-8J where highest force last 1ms. It is a result of H_4-8J contains a relatively soft centre region which can deform more than CFRP. In other word, the soft centre region absorbs impact energy and creates delamination easily. H_1-12J has evenly distributed glass layer that induces damage in every soft layer. This observation validate the results shown in Table 3 where the specimens contain glass layer at centre draw the delamination damage towards centre of specimens.

3.3.1 Damage Mechanisms and Interaction CT-scan

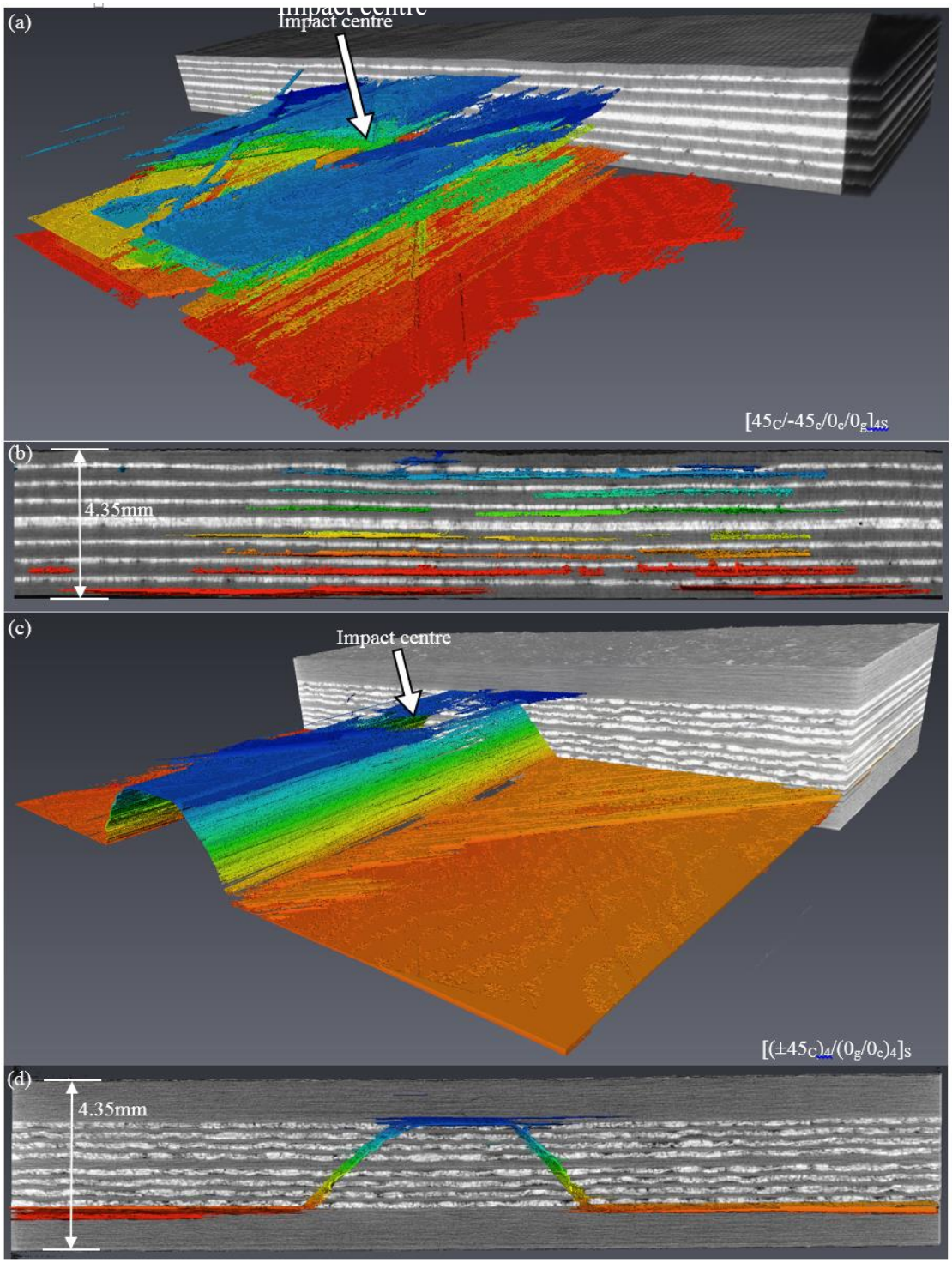

Figure 7 *X-ray CT 3D distribution and cross-section of delaminations and intra-ply cracks following an 18J impact to a* $[(\pm 45_C)_4/(0_g/0_c)_4]_s$ *laminate. White layers are GFRP. Colours are indicative of delamination depth. Impact is to the top of the specimen. Scales are approximate.*

Figure 7 shows a 'hat-shaped' damage morphology (coloured region) derived from a dynamic 18J impact to a hybrid GFRP/CFRP laminate with blocked stacking sequence $[(\pm 45_C)_4/(0_g/0_c)_4]_s$.

3.4 Damage Resistance Discussion

A comparison of C-scan results in Table 3 for specimens with 12J impacts (H_2, H_3 and H_5) and identical stacking sequences suggests that if glass layers are included, their through-thickness positioning has a significant effect on delamination morphology, independent of the overall percentage of glass layers. The through-thickness position of the largest delamination is also affected. A detailed discussion of damage morphology follows.

3.4.1 Delamination Size

Stacking sequence and in particular blocking of plies into either (45_C/-45_C) and (0_C/0_g) or (45_C/-45_C) and (-45_g/45_g) groups has a significant effect on the maximum delamination diameter. A comparison of damage distributions for all specimens clearly shows this effect as the largest delaminations occur in the region where these blocks meet, i.e. interface 8 for all specimens except H_2 where blocking of (45_C/-45_C) and (-45_g/45_g) plies occurs at the 5th interface and H_1 where all even interfaces separate blocks of (45_C/-45_C) and (0_C/0_g) plies. Blocking produces interfaces where sharp contrasts in dominant ply direction and thus significant differences in the direction of principal bending stiffness occur. These incompatibilities result in large inter-laminar stresses.

Hybrid laminates H_2, H_3, H_4 and H_5 displayed larger maximum delaminations than both H_1 and the fully CFRP laminates. This is partially due to the effect of ply-blocking noted above but is also an effect of the placement of glass layers.

Although the hybrid laminates tested here are thicker than the CFRP laminates, which increases the second moment of area of the former, this does not necessarily result in higher laminate bending stiffness as GFRP plies are considerably less stiff than CFRP plies. Laminates H_2, H_4 and H_5 have similar longitudinal and transverse bending stiffness to the fully CFRP laminates CD and hence any full laminate stiffness effects are unlikely to play a role in the difference between delamination sizes and distribution seen in these sets of laminates. In contrast, H_1 has a relatively high longitudinal stiffness in comparison to the other laminates which may have played some part in the small back face delaminations seen in this laminate as impacts to stiffer/thicker laminates tend to cause delaminations to occur closer to the impact surface. H_3 has the lowest bending

stiffness due to its GFRP outer plies and hence will deflect the most under impact creating the highest bending induced intra-ply shear-stresses and the largest delaminations.

3.4.2 Delamination Distribution

The comparatively large number of delaminations in H_1 is a consequence of the dispersed stacking sequence creating multiple through thickness regions with considerably different bending stiffness. In contrast to H_1, which has interspersed carbon and glass layers, where the first delamination occurs at the 2nd interface from the back face, the first delamination from the back face for the other hybrid laminates does not occur before the 5th interface. This is because when considered with regard to the shape of the ASTM impact window and the resulting relative lengths of the 45^o fibres, pairs of ±45^o plies are relatively compliant compared to quasi-isotropic (i.e. $[45/0/-45/90]_2$) outer ply stacking sequences during impact and thus relieve inter-laminar stresses.

The use of GFRP layers in combination with a damage tolerant stacking sequence, which places compliant pairs of ±45^o plies on the outside of the laminate, has in most cases amplified an effect of the stacking sequence which causes a high proportion of the total area of delamination to occur closer to the mid-plane of the laminate. The central delamination distributions seen in H_3, H_4, H_5 and to some extent H_2 are a product of the damage resistant aspects of the stacking sequences used and the ductility and low modulus of the GFRP layers. It is evident that centrally located GFRP layers draw damage to the centre of laminates H_2-H_5. This is an effect that is hybrid laminates where damage was drawn to the outer layers when non-CFRP layers were blocked together there. This means little or no delamination occurs in the critical through-thickness region where local buckling and delamination propagation can occur.

Impacts to H_3 and H_4 specimens resulted in the least near-surface delaminations, in the latter case this was most likely a consequence of the low impact energy particularly when the damage distribution of H_5-12J is taken into account. In the former case it has been shown that GFRP and aramid fibre hybrid laminates have high strains to failure indicating they maintain laminate integrity better than CFRP under impact conditions.

Further to this it was shown that the failure strength of GFRP unidirectional laminates in tension increased significantly with increasing rates of strain, an effect not seen in CFRP laminates.

3.4.3 Damage Visibility

Coupon	D_{11} (kNmm)	D_{22} (kNmm)	Buckling mode
CC2/CC3	340	322	Overall (Anti-symmetric)
H1	455	237	Local (Sublaminate)
H2	335	262	Overall (Symmetric)
H3	291	199	Overall (Symmetric)
H4	366	293	Overall (Symmetric)
H5	350	293	Overall (Symmetric)

Table 4 *Buckling modes and overall bending stiffness of Table 2 laminates in longitudinal (D_{11}) and (D_{22}) transverse direction.*

Impact damage visibility and BVID detecting ability was improved by the GFRP layers on the outside of the H_3 laminate. This was due to the formation of opaque through-thickness regions in the outer glass plies, particularly on the back face, following impact that were easily distinguished from the intact glass regions that remained translucent. However, external aircraft surfaces are painted and thus this increased visibility will only apply to internal surfaces. Note that, hybrid laminates have a more elastic response to impact than CFRP laminates due to the lower bending stiffness of the former, see Table 4. This is likely to result in smaller visible dents in the hybrid laminates following impact which may hamper impact detection. This would result in a higher energy impact being required to create BVID in hybrid laminates than that required for CFRP laminates. The authors conclude though that although damage visibility may decrease for hybrid laminates the significant increases seen in damage tolerance would be worth the sacrifice particularly if a non-visual damage detection system/method were implemented.

3.5 Analytical Through-Thickness Shear Stress Model

The aim of building up an analytical model is to discover the through-thickness shear stress when laminates are subject to low-velocity impact. From the observations made in the previous section, the CFRP/GFRP hybrid laminates can draw delamination damage into a centre region which is relatively softer than the outer surface. As the physical properties of GFRP are softer than carbon fibre, the through-thickness shear

stress could be extensively induced in this region. The preliminary analytical model is based on this assumption and in this section the full shear stress derivation will be presented.

3.5.1 Derivation of through-thickness shear stress

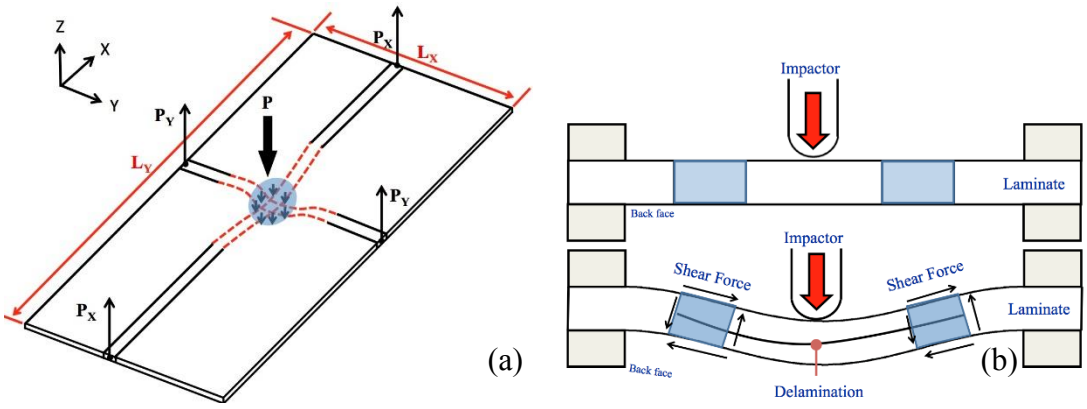

Figure 8 *(a) A 2D free body diagram of impact test. (b) A 2D free body diagram of impact test from cross sectional view.*

The specimens experimented in impact tests have same dimensions of 210x100 mm. As the ASTM standard requires for impact test, the specimens are clamped over a window of 125x75 mm. In the analytical model, the dimension parameters used for specimens are the impact window dimensions. This is due to the impact window provides a clamped boundary condition that only within this region the impact damage are initiated. In order to simply the impact procedure, the impact force is simulated as a concentrated load applied in the centre of specimen as Figure 8 (a) shows, P. From this 2D free body diagram, the distributed reaction forces on each edge of specimen are treated as one resultant force acting in the middle of each edge as Figure 8 (a) shows above. In this global axis, the X and Y directions indicate the 0^o and 90^o fibre orientation and Z is the through-thickness direction. In this stage of work the plate is simplified as 1D model, which treats the specimen as two strips perpendicular to each other at centre and the impact force acts on the overlapped region of two strips as the shaded area represents in Figure 8 (a). As the specimen is under compression, the contact region deflects as Figure 8 (b) shows. For the same deflection the following equations are derived. P_X and P_Y are resultant forces of total impact load P. Δ_X and Δ_Y are out-of-plane deflections due to impact on two strips. L_X and L_Y are length and width of impact

window. The term *EI* gives the global bending stiffness of strip in X and Y direction respectively. It assumes both the strips have same the deflection.

$$2P_X + 2P_Y = P \qquad (1)$$

$$\Delta_X = \Delta_Y = \frac{P_X L_X^3}{(EI)_{XX}} = \frac{P_Y L_Y^3}{(EI)_{YY}} \qquad (2)$$

Using above two equations, the value of reaction forces P_X and P_Y can be determined for any given impact load P.

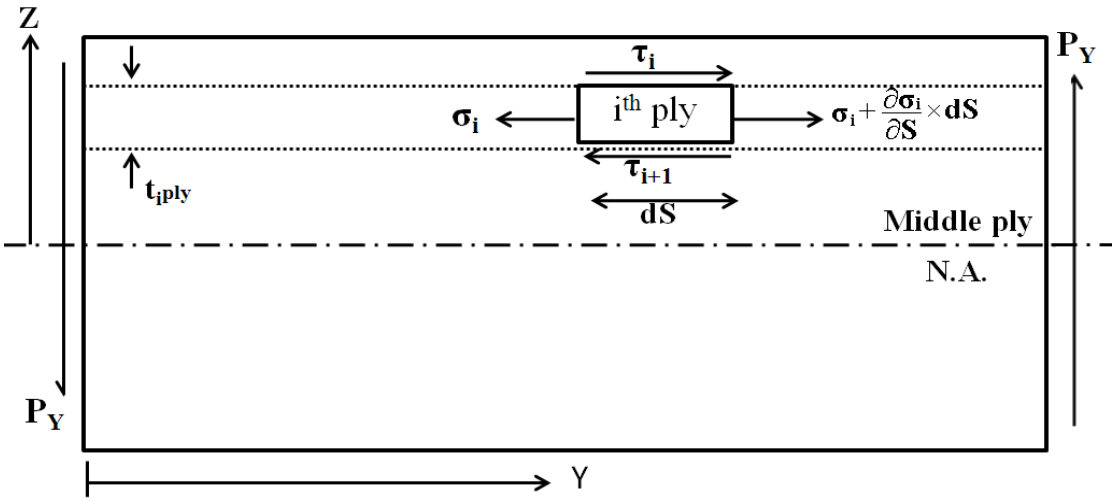

Figure 9 *Detailed free body diagrams in cross sectional view.*

Take the strip in Y direction as an example, the Figure 9 shows a detailed free body diagram in half cross section of plane YZ. Laminate of thickness, t_{total}, ply thickness of t_{iply}, subject to a running shear of q Nmm^{-1}(caused by reaction for P_Y), which is equal to P_Y / t_{total}. The stress equilibrium over a distance *ds* gives

$$\left(\sigma_i + \frac{\partial \sigma_i}{\partial s} ds - \sigma_i\right) t_{iply} - (\tau_i - \tau_{i+1}) ds = 0 \qquad (3)$$

Simplify (3) gives

$$\tau_{i+1} = \tau_i - \frac{\partial \sigma_i}{\partial s} t_{iply} \qquad (4)$$

For Engineer's bending theory (5) and strain stress relationship (6)

$$\varepsilon = \frac{My}{D} \tag{5}$$

$$\frac{\sigma_i}{\varepsilon_i} = k_i \tag{6}$$

Where D is the plate bending stiffness, M is the bending moment, y is the distance to the neutral axis, k_i is the through-thickness stiffness and subscript i indicates the ply number. Then combines (5) and (6), it gives

$$\sigma_i = \frac{Mk_i y_i}{D} \tag{7}$$

Differentiate σ_i respect to ∂s gives

$$\frac{\partial \sigma_i}{\partial s} = \frac{k_i y_i}{D}\, q \tag{8}$$

Then substitute (8) into (4)

$$\tau_{i+1} = \tau_i - \frac{k_i y_i}{D}\, q \tag{9}$$

According to the final equation (9), for any layer i there are corresponding k_i, y_i, D and q. When i=0, which give the through-thickness shear stress at specimen surface, the term τ_i=0. Thus it gives that the shear stress remains zero at the outer surface, asthe calculation moves towards the centre, the shear stress accumulates to maximum where the distance between the lay and neutral axis starts becoming negative (it assumes the region above the neutral axis has positive y_i).

3.5.2 Results

For the analytical model derived above, the through-thickness shear stress is calculated for each interface under a same compressive load applied to all the specimens. The results present here for three specimens CC_2 ($[(45/-45)_4(0/90)_4]_S$), H_1 ($(45/-45/0/0_g)_{4S}$) and H_4 ($[(45/-45)_4(0/0_g)_4]_S$). Three curves indicate the shear stress peak at the mid region of specimen as shows in Figure 10. For H_4, the centre group $0/0_g$ contains a large amount of fibre in the same direction that allows cracks to initiate in this region. Furthermore, this region is softened by 0_g fibres which induce a higher through-thickness shear stress than the 45/-45 outer sub-group. Under these combined facts, extensive delaminations occur in this centre region. This validates the delamination distribution for H_4 shown in Table 3. For H_1, the sub-laminate $45/-45/0/0_g$ contains a weak layer 0_g at every group, which increases the through-thickness shear stress in every four interfaces as the dashed line shown in Figure 10 compared with other two curves. Since $0/0_g$ evenly distributes in every four interfaces, which allows the cracks initiate and causes delamination to occur in the interface of $0/0_g$. It explains the discontinuity of delamination for H_1 in Table 3. Specimen CC_2 does not contain any unidirectional fibre groups, but the stiffness mismatching between sub-laminate 45/-45 and 0/90 leads to a major delamination occurred at 7^{th} interface. The close surface delamination is possibly caused by surface crack peeling (see delamination distribution in Table 3). These factors stated above indicate that a combined idea of unidirectional sub-laminate and softening layer could locate cracks initiation and delamination. It can be concluded that hybrid CFRP/GFRP laminate H_4 is a damage resistant design that draws the delamination into centre region to protect the specimen away from sub-laminate buckling.

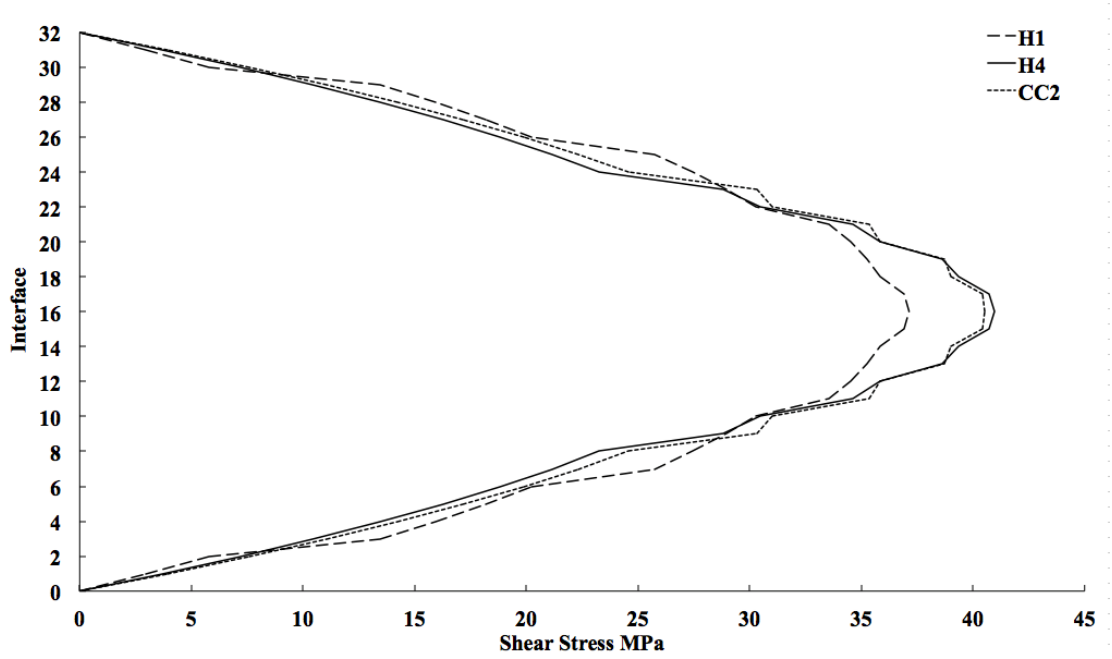

Figure 10 *Through-thickness shear stress distribution under same compressive load for* CC_2 *(*$[(45/-45)_4(0/90)_4]_S$*),* H_1 *(*$((45/-45/0/0_g)_{4S}$*) and* H_4 *(*$[(45/-45)_4(0/0_g)_4]_S$*).*

3.6 Analytical Strip Model

There is a simple Strip model to predict critical threshold values of applied strain below which initial local buckle-driven propagation of a delamination will not occur. Delamination areas below the sub-laminate under investigation are modelled as circles to produce a simple approximation of the damage in a laminate, as viewed on a C-scan. The Strip model is then used to calculate the compressive threshold strain ε_{th} for the associated sub-laminate, ε_{th} is given by,

$$\varepsilon_{th}=\varepsilon^{C}\left(-1+\sqrt{4+\frac{2G_{IC}}{A_{11}(\varepsilon^{C})^{2}}}\right)$$

Where ε^{C} is the buckling strain of the circular sub-laminate adjacent to the delamination, calculated using the 2D infinite strip program, G_{IC} is the strain energy release rate required to cause Mode I fracture in the matrix material and A_{11} is the axial stiffness of the sub-laminate. The propagation strain is converted to a propagation stress σ_{th} using the theoretical axial modulus E_{xx} of the laminate.

3.7 FEA Simulation

In this section of work the finite element method is introduced along with the FEA software used (ABAQUS) in order to investigate the through-thickness shear stress between the adjacent layers of laminate plate under a concentrated load. The shear stress calculated from analytical model and FEA model are compared for the best damage tolerance design specimens. The aim of this study is to validate the results that generate from analytical model and experimental work.

In this phase of work the FEA model is established to simplify the low-velocity impact test. The impact test is defined as a concentrated force loading in the centre of hybrid laminate specimen and the four edges are fully clamped. In order to meet the requirement in analytical model, the specimen size remains 125x75 mm which is the dimension of impact window. The first step of FEA model starts from a simple 1D beam mode, which only contains dimensional characters in one single direction of specimen. In order to observe the through-thickness shear stress in both X direction and Y direction, the beam mode contains two beam strips under a central line loading which can generate date comparable with analytical model. The aim of this step is learning to use ABAQUS building composite laminate model and apply suitable boundary conditions and loading conditions. The second step is creating a plate model to simulate the real specimen shape and apply a central loading area as a simplified solution of impact.

3.7.1 Beam Model

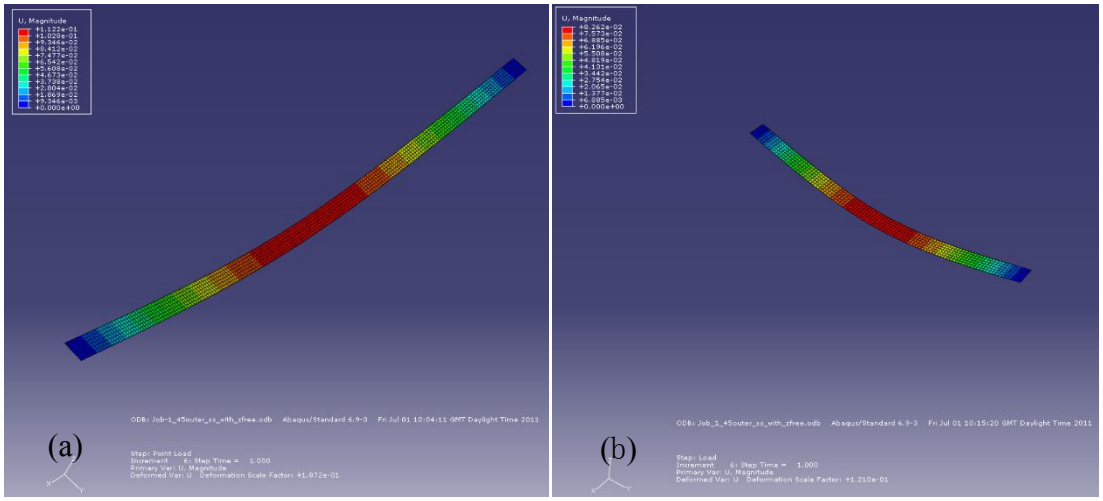

Figure 11 *(a) Beam deflects under line loading in X direction. (b) Beam deflects under line loading in Y direction.*

In order to simply the simulation of impact test, the start of FEA model is focus on a beam model. The beam model contains two beam strips taken from the middle of specimen in X (where 0^o fibre aligns) and Y direction. As Figure 11 shows below, (a) is the beam strip crosses specimen longitudinally with a dimension of 125x6 mm and (b) is the beam strip crosses specimen transversely with a dimension of 75x6 mm. Since the impactor size as 16mm, the width of beam must be small enough to ensure the effectiveness of line loading on beams. The both beam strips receive a line loading in the centre and it aligns the same as beam's short edge and pushes the beam down to its thickness. The colour contour shows the distribution of through-thickness shear stress where the maximum shear stress occurs in the centre of beam as the red area indicates. The evenly distributed line loading has equivalent impact energy of 10J.

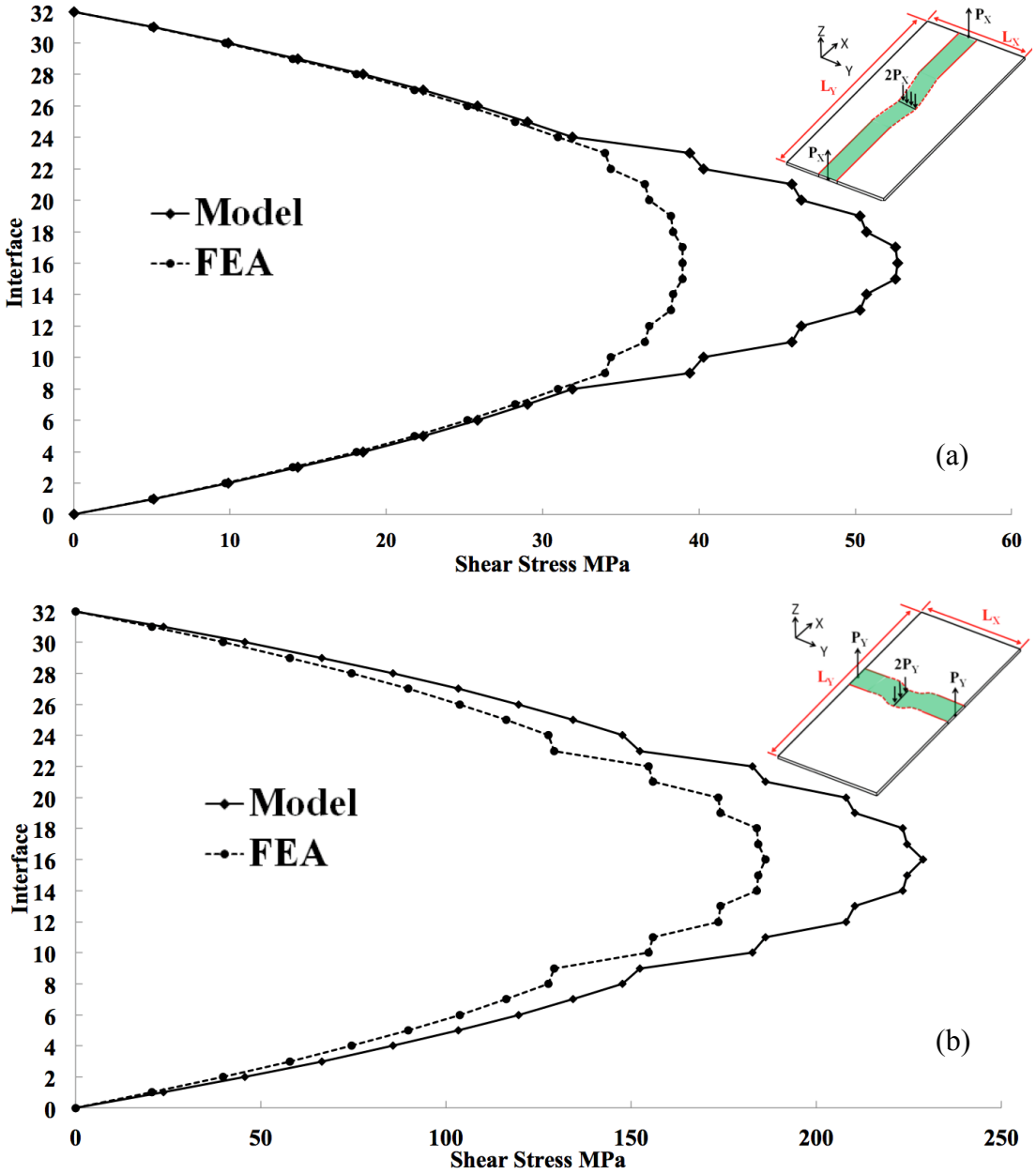

Figure 12 *Interface through-thickness shear stress for* CC_2 *(*$[(45/-45)_4/(0/90)_4]_S$*) in (a) X direction and (b) Y direction respectively.*

The through-thickness shear stresses are calculated in both directions for each interface. Figure 12 shows a comparison of through-thickness shear stress in every interface between analytical model (label as Model) and FEA model (label as FEA). The through-thickness shear stress, in both directions, presents a same tendency where the shear stresses in outer surface $(45/-45)_4$ group increases slowly and smoothly. At the 8^{th} interface, as the centre group takes place, the slope suddenly leaps and then slows down. This pattern of growth repeats until the curve peaks in the centre. For symmetric laminate, the shear stress plots are always symmetrical and it peaks at the mid-plane.

The analytical and FEA results show an agreement on tendency, but the magnitude of stress in individual interface, especially in the centre groups, the analytical results are 20% higher than FEA. This could be a consequence of imperfect analytical model. The magnitude difference between two directions is quite significant. The cause is due to the size difference of two beam strips. For the long beam strip, the reaction force distributed on the edge is much smaller than the short one. This can be improved by introducing the plate model. The analytical model is only through-thickness shear stress based calculation with ignoring other effects such as twisting effects (relative to D_{33}). However, the FEA model is only a simplified simulation with concentrated line loading that is less practical than real impact test. All these terms that effect the analytical model and FEA model will be discussed in Future Work section. The great achievement in this stage of work is to get both models running and they show an agreement in tendency.

3.7.2 Middle Delamination Model

This part of work is continued from the hypothesis made in previous section that the delaminations occur at the region with highest through-thickness shear stress. Once the delamination occurs at the maximum shear stress region, it assumes, consequently, this mid-plane losses stiffness and strength and the 32 plies specimen can be treated as two separated 16 plies specimen with half stacking sequence (asymmetrical) received half impact load. If repeat the analytical model and FEA model for this 16 plies specimen, the next delamination position can be located at next through-thickness shear stress peaks. In order to prove the hypothesis in Section 6, the same stacking sequences are taken into consideration CC_2 ($[(45/-45)_4(0/90)_4]$), H_1 ($((45/-45/0/0_g)_4)$ and H_4 ($[(45/-45)_4(0/0_g)_4]$).

As Figure 13 shows (a), in X direction, the maximum through-thickness shear stress occurs also at the mid-plane in the 8^{th} interface. Since CC_2 and H_4 contain a sub-group (45/-45), the curve increases smoothly before the stress peeks. As the ply stiffness changes after maximum value, the stress decreases dramatically when 0/90 or $0/0_g$ groups appear. Comparing full CFRP CC_2 with hybrid H_1 and H_4, it can tell from both Figure 13 (a) and (b) adding glass layers into full CFRP specimens can significantly increase through-thickness shear stress to the mid-plane. For H_4, it contains relatively soft mid region which induces the shear stress between the layers to create delamination.

This is a clear analytical evidence for H_4that receives higher impact energy and contains delamination towards the centre as the impact results show in Table 3. For H_1, the independent sub-layer ($45/-45/0/0_g$) reserves a weak layer in every four plies and due to the high through-thickness shear stress the damage occurs quite close to the surface (also see Table 3). The full CFRP CC_2 also contains a soft mid-region, but there is no glass layers in it which makes the inter-plies are unlikely to shear.

In Figure 14, the through-thickness shear stress in Y direction, for both analytical results and FEA results, shows reverse phenomenon that observes in Figure 13. With adding the glass layers into full CFRP specimen the shear stress decreases as the CC_2 has the highest stress in three specimens. This could be a result of limitation of analytical and FEA model. For analytical model, the assumption made is purely based on shear stress, there are other effects should be included such as the twisting stiffness D_{33}. And for FEA model, the simulation is only based on a simplified model, for the future work the impact simulation will be required to fix this conflict.

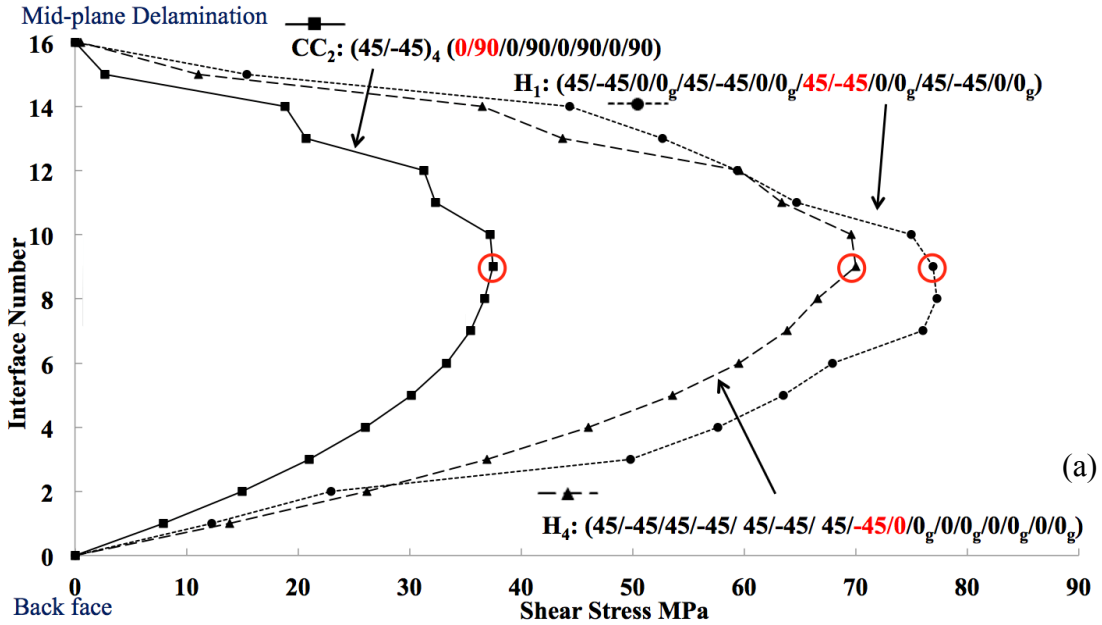

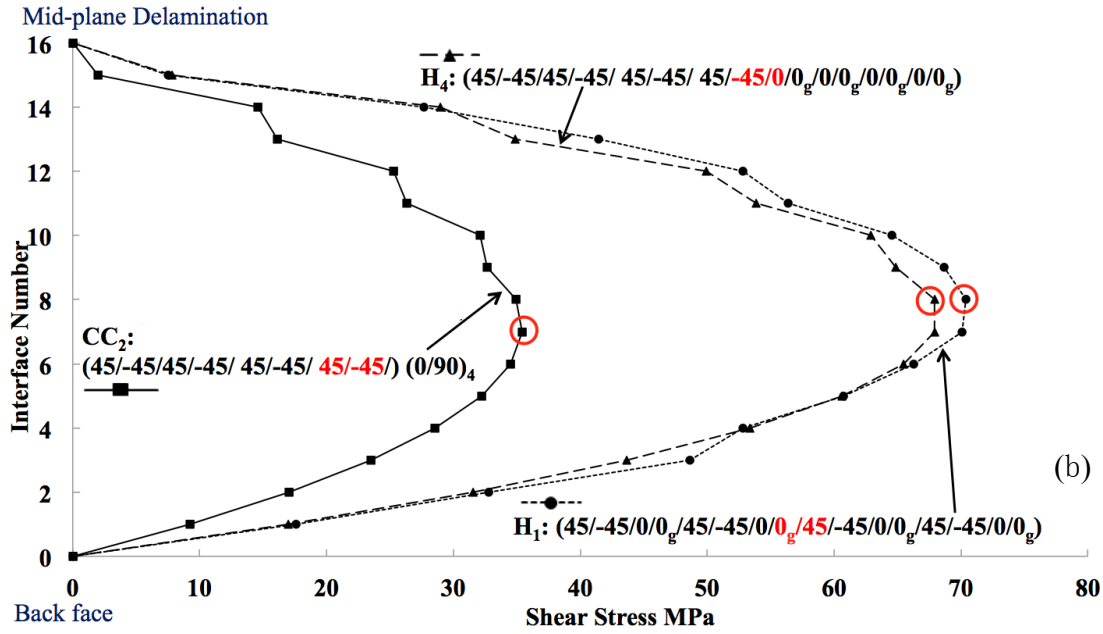

Figure 13 *Through-thickness shear stress in X direction for 16 plies specimens CC_2 ($[(45/-45)_4(0/90)_4]$), H_1 ($(45/-45/0/0_g)_4$) and H_4 ($[(45/-45)_4(0/0_g)_4]$) for (a) analytical model and (b) FEA model.*

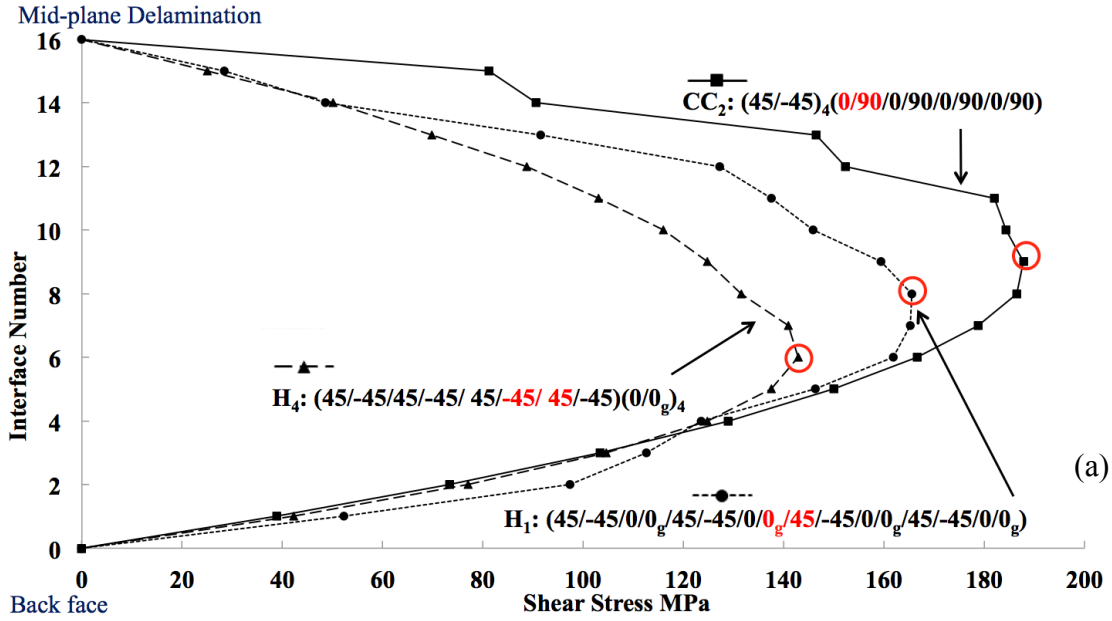

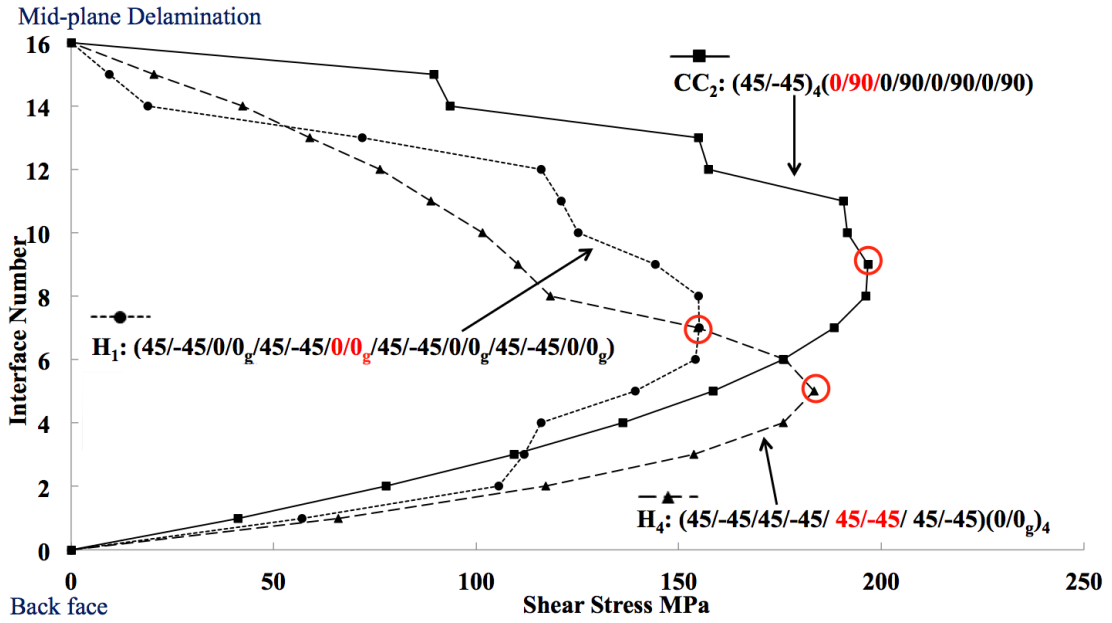

Figure 14 *Through-thickness shear stress in Y direction for 16 plies specimens CC_2 ($[(45/-45)_4(0/90)_4]$), H_1 ($(45/-45/0/0_g)_4$) and H_4 ($[(45/-45)_4(0/0_g)_4]$) for (a) analytical model and (b) FEA model.*

3.7.3 Plate model

As in beam model, the shear stress tendency shows agreement that encourages author carrying on to plate model. In this model, a plate with size of 125x75 mm is created and receives an area loading and the through-thickness shear stress is observed. This method is much closer to the real impact test than beam strip method. As Figure 15 shows, the plate model is under an area pressure and the maximum shear stress occurs at the centre of plate.

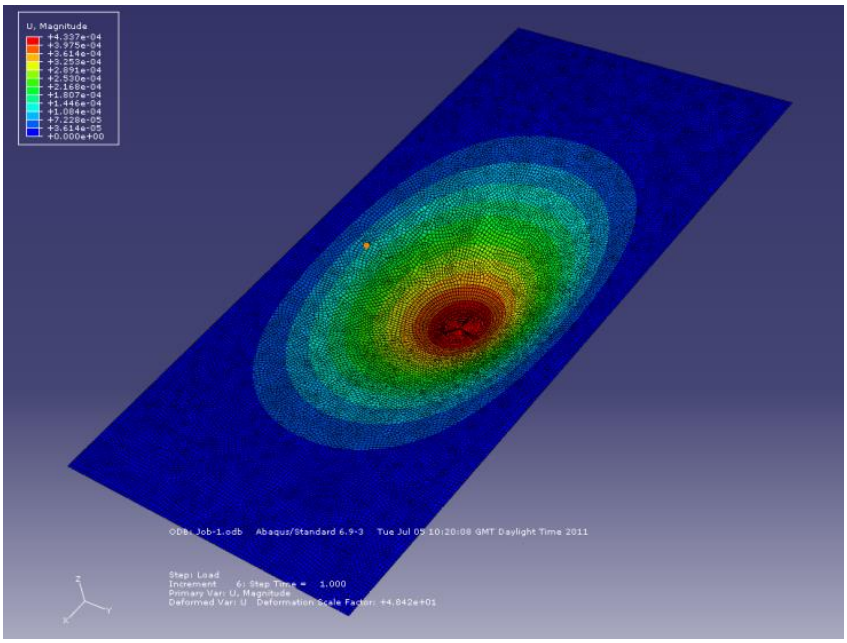

Figure 15 *Plate model under an area loading at the centre.*

In Figure 16, it clearly shows the through-thickness shear stress distribution at mid-plane for CC_2 ($[(45/-45)_4/(0/90)_4]_S$). In contrast to the shear stress in X direction (Figure 16 (a)), the shear stress is much more widely distributed in Y direction. The difference is again due the closer boundaries in Y direction. However, the maximum stress region covers the equal area at centre where the red contour indicates.

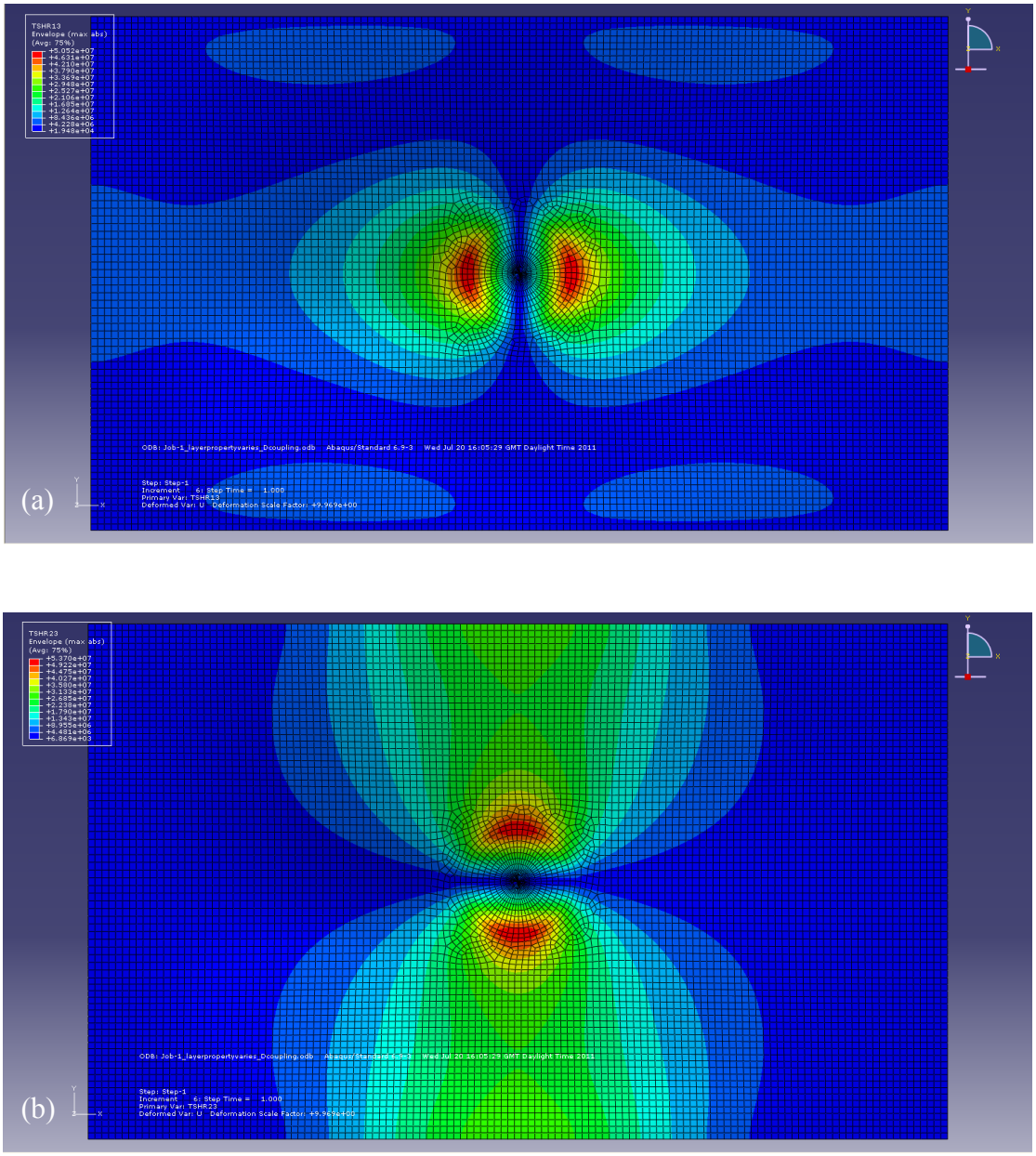

Figure 16 *Through-thickness shear stress at mid-plane for plate model for* CC_2 *[(45/-45)*$_4$*/(0/90)*$_4$*]*$_S$ *in (a) X direction and (b) Y direction.*

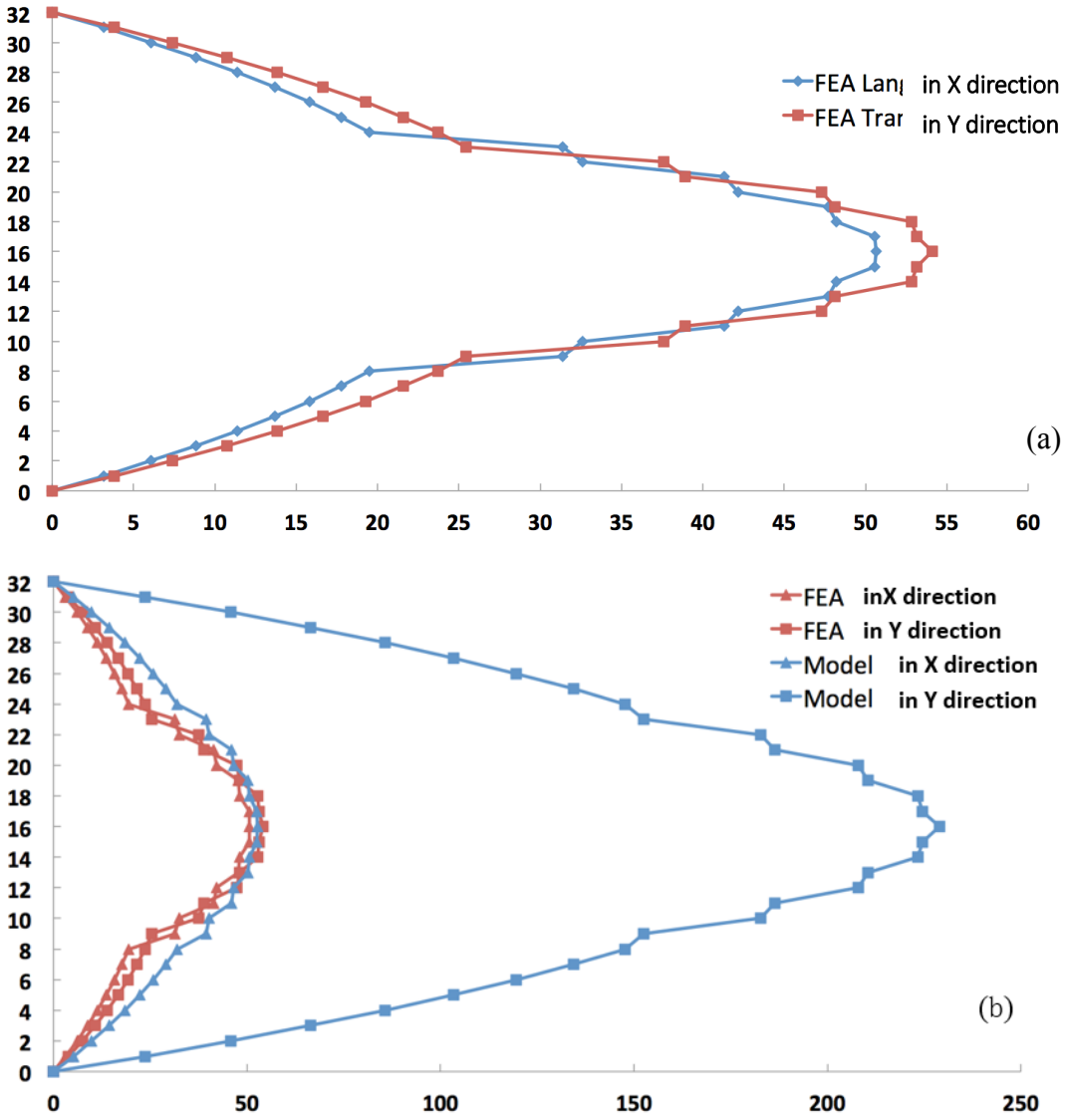

Figure 17 *(a) Plate shear stress for FEA model in both directions. (b) Plate shear stress for FEA and analytical model in both directions. Both figures are for* CC_2 *[(45/-45)*$_4$*/(0/90)*$_4$*]*$_S$*.*

In order to keep results comparable, CC_2 is studied in this model. The plate shear stress in Figure 17 (a) presents the curves for FEA model in both directions agree each other, the large value in Y direction for beam model decreases and converge to longitudinal values. Although the individual interface has greater or smaller shear stress, but the difference is minor, and the peak value is close. Figure 17 (b) compares the shear stress for analytical and FEA models in two directions. Except for shear stress of analytical model in Y direction, the other three stresses show strong agreement. This proves that the analytical model predicts shear stress in Y direction need to be modified. The reason could be the different strip dimensions used in model or the effects have not been taken into consideration such as twisting effect.

4 Chapter 5 Damage Tolerance of Carbon-Glass Laminates in Compression after Impact Experiments

4.1 Introduction

For compression testing, laminates were placed in a compression devise with a circular anti-buckling guide of internal diameter 85mm, see Figure 19. Tests applied axial compression under displacement control that leads to local delamination propagation and/or global failure. The back (non-impact) faces of the specimens were covered in a random speckle pattern to allow buckling modes and failure sequences to be visualized using the DIC system. This system employs a pair of stereo cameras to produce plots of out-of-plane displacement relative to a reference image taken under zero loads. To ensure specimens were correctly aligned, strains were recorded throughout the tests by two pairs of vertically aligned back-to-back strain gauges as Figure 18 shows for a schematic diagram of strain gauge placement.

4.2 Experimental Methods

4.2.1 Strain Gauge Installation

Before the composites were compressed, each specimen was end-tabbed and installed four strain gauges on the surface in back to back pairs. The position of the stain gauges for each specimen is shown in Figure 17. The purpose of fixing strain gauges is to monitor the strain variation across the specimens during CAI.

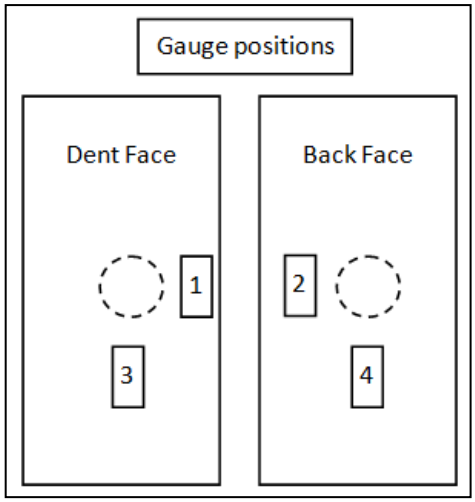

Figure 18 *Strain gauge positions.*

4.2.2 CAI

Before the specimens were tested in compression, an anti-buckling guide was used to provide fixed boundary conditions. This fixture is designed to make sure the specimen would buckle only inside the window of the guide and prevent the global buckling as Figure 19 shows.

For CAI test, numerous measurements are taken using several different pieces of equipment. The Instron 1332 is connected to a computer, via Spider 8, with a data recording software Catman. Catman monitors the strain variation from the strain gauges and loads at chosen sample rates of either 5 or 10 Hz.

It is also necessary to shim the specimen before the test. Shimming is a process whereby a number of thin metal shims are placed between the specimen mounting blocks and the Instron machine in order to ensure the specimen is loaded evenly in pure axial compression and does not twist or bend out-of-plane. To test the specimen is twisting or bending is by measuring the strains across the gauges whilst applying a small compressive load through the specimen. If all the strains across the specimen are within 10% of each other the specimen is considered to be in pure compression. The specimen is then compressed with larger loads of up to 5kN to ensure an accuracy of 10% across the strain gauges is maintained.

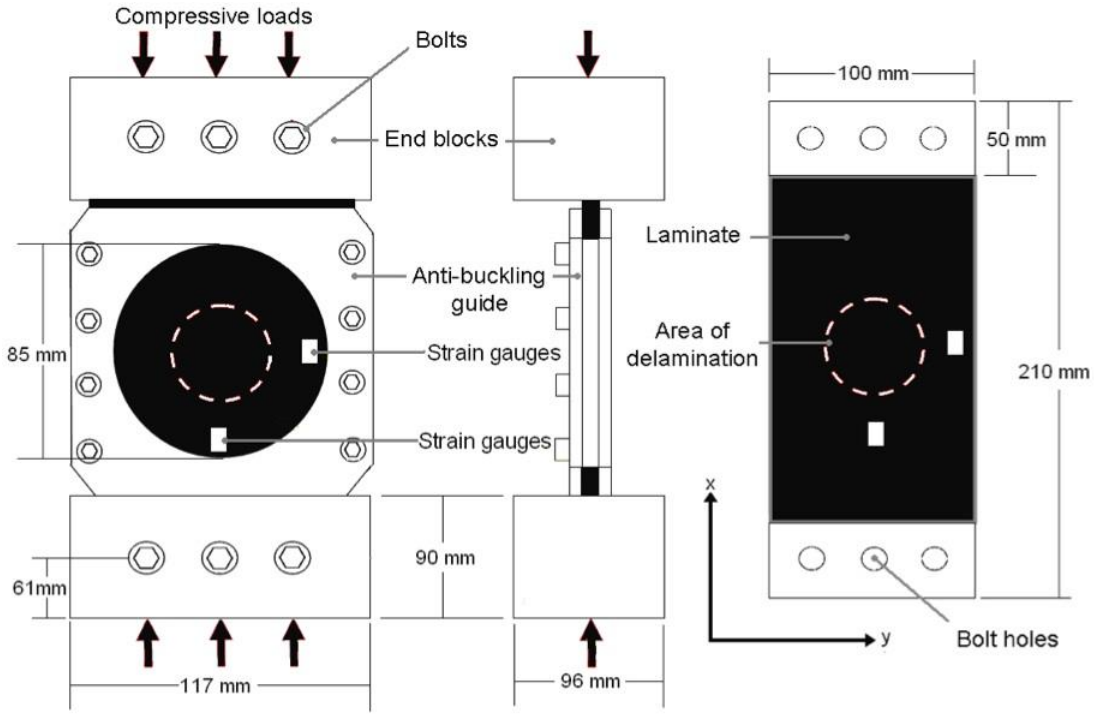

Figure 19 *Anti-buckling guide and compression test rig.*

4.2.3 Digital Image Correlation (DIC) Systems

During the CAI tests, full-field displacement profiles of the specimen surfaces as well as the specimen local behaviour at the moment of rupture were captured by three 3D Digital Image Correlation (DIC) systems. The DIC results together with specimen compliance derived from the testing machine were analysed here.

In order to capture 3D displacement, a pair of high-speed cameras were placed at an angle to one face of the specimen as it buckled. The specimen were dotted with white paint which marks the displacement of the surface of the specimens as they buckle during the compression tests.

4.3 CAI Results

Laminate ID - Impact energy	Lay-up (C1=AS4/8552, C=HTA/913C, g=GE5/913)	E_{xx} (GPa)	σ_{th} (MPa) Experimental/ Analytical	Experimental Failure Stress (MPa)
CC_1-8J	$[(\pm 45_{C1})_4/(90_{C1}/0_{C1})_4]_S$	51	289 / 300	349
CC_2-18J	$[(\pm 45_C)_4/(0_C/90_C)_4]_S$	55	-	253
CC_3-18J	$[(\pm 45_C)_4/(0_C/90_C)_4]_S$	55	-	250
H_1-12J	$[45_C/-45_C/0_C/0_g]_{4S}$	55	284 / 290	284
H_1-15J	$[45_C/-45_C/0_C/0_g]_{4S}$	55	247 / 275	276
H_1-18J	$[45_C/-45_C/0_C/0_g]_{4S}$	55	233 / 275	288
H_2-12J	$[\pm 45_C/45_C/(\mp 45_g)/-45_C/\pm 45_C/(0_C/0_g)_4]_S$	55	-	342
H_3-12J	$[(\pm 45_g)_2/(\pm 45_C)_2/((0_C)_3/0_g)_2]_S$	65	-	343
H_3-18J	$[(\pm 45_g)_2/(\pm 45_C)_2/((0_C)_3/0_g)_2]_S$	65	-	355
H_4-8J	$[(\pm 45_C)_4/(0_C/0_g)_4]_S$	55	-	404
H_5-8J	$[(\pm 45_C)_4/(0_g/0_C)_4]_S$	55	-	403
H_5-12J	$[(\pm 45_C)_4/(0_g/0_C)_4]_S$	55	-	>382*

Table 5 *Impact energy, stacking sequence, theoretical axial modulus E_{xx}, initial propagation stress σ_{th} and failure stress of specimens. Note that analytical initial propagation stresses σ_{th} are found using the Strip model and are based on delamination sizes from C-scan data.*

Failure stresses and propagation stresses are given in Table 5 and were calculated by dividing the corresponding loads by the cross-sectional area of each specimen. Table 5 also gives analytical predictions of propagation stresses. Failure of the laminates occurred via one of the three following mechanisms, determined from a combination of DIC images (Figure 20) and load vs. strain plots (Figure 21). For the CC_1 and H_1 specimens failure was brought about by propagation of a delamination following local buckling as shown by the localized colouring and tight contours in Figure 20 (c) and (d). Propagation is also indicated by small discontinuities which are highlighted by a circle on the corresponding load vs. strain plot; see Figure 21 (b). The circle of Figure 19 (c) indicates the boundary of the area containing the initially buckled region, propagation occurs once the buckled region spreads outside this circle.

For the CC_2 and CC_3 specimens, failure followed a change in global buckling mode shape from that seen in Figure 20 (a) to a fully anti-symmetric mode contained within the confines of the anti-buckling guide seen in Figure 20 (b). The large discontinuities seen on the load vs. strain plot in Figure 21 (a) are coincident with the sudden jump to a fully anti-symmetric buckling mode from an intermediate asymmetric mode that developed at loads between those shown in Figure 20 (a) and (b). The third failure mechanism noted in the remaining laminates, see Figure 20 (e) and (f), was that of material failure induced by (symmetrical) global buckling. Note the non-localized,

more slowly changing pattern of colours in Figure 20 (e) and (f) seen for global buckling in comparison to the central region of Figure 20 (c) and (d). Load vs. strain plots for symmetric globally buckled specimens show a steady divergence of strain gauge curves (see Figure 21 (c)) consistent with global buckling.

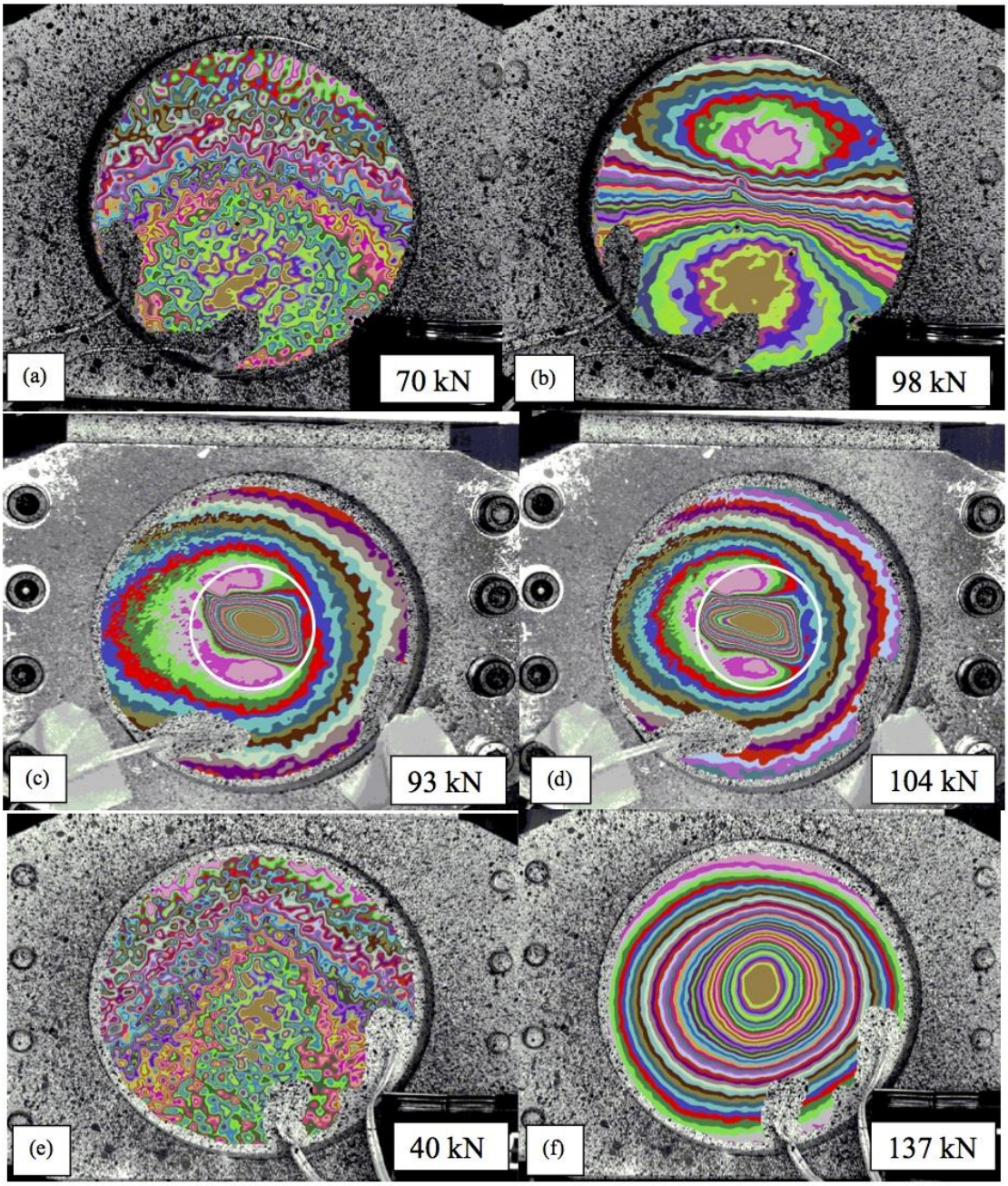

Figure 20 *DIC images during CAI testing with colours indicating out-of-plane displacement from an initial unloaded state. (a) Global buckling prior to (b) anti-symmetric global buckling in CC_2-18J. (c) Local buckling above a delamination and (d) following propagation in H_1-18J. (e) and (f) Evolution of the global buckling of H_3-18J.*

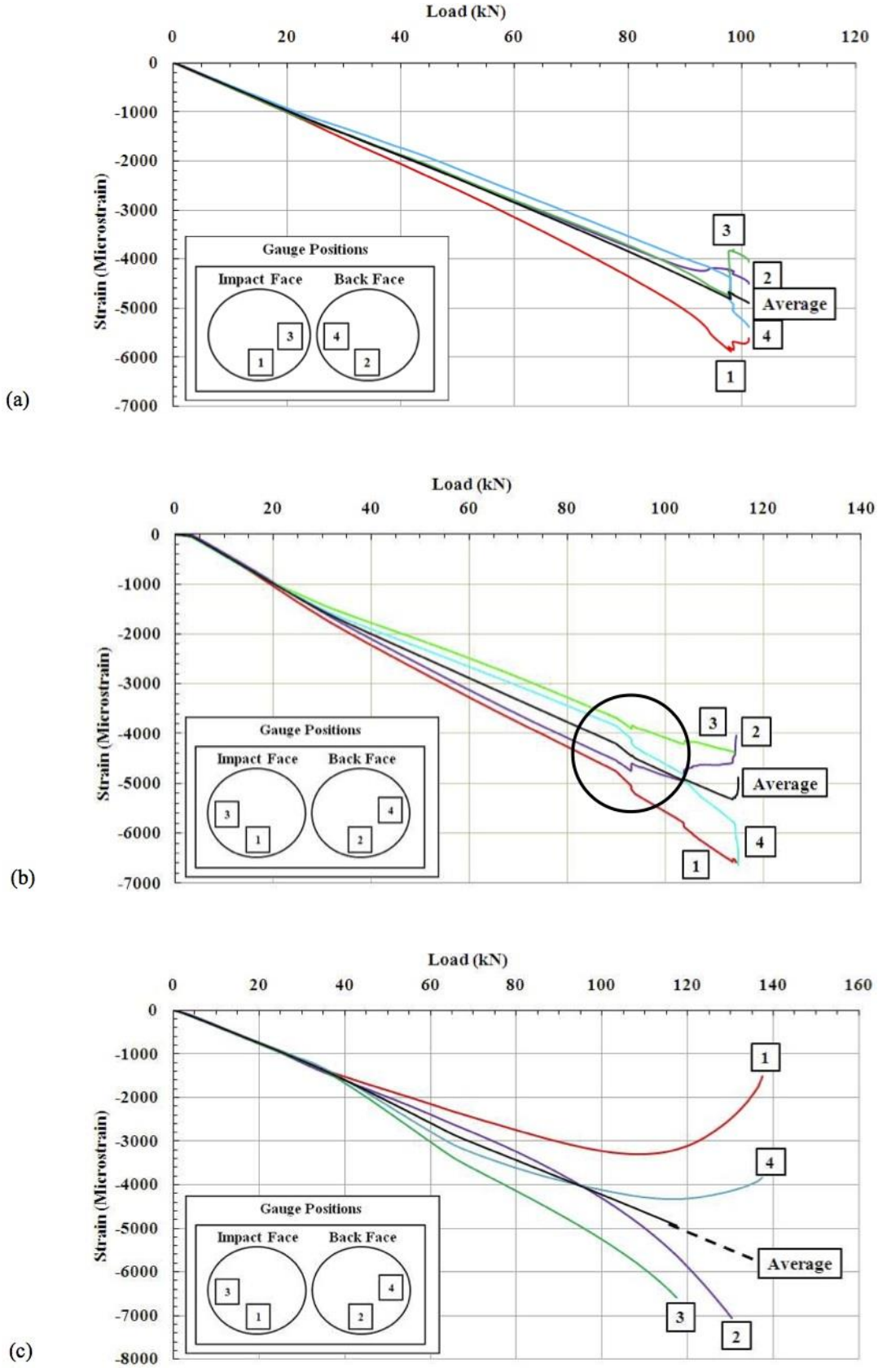

Figure 21 *Load vs. Strain plots for compression (CAI) testing of laminates: (a) CC_2-18J, (b) H_1-18J and (c): H_3-18J. The circle in (b) highlights discontinuities associated with delamination propagation.*

4.4 Discussion

4.4.1 Damage tolerance

Despite the use of an anti-buckling guide during compression tests, global buckling was detected via strain gauge plots and DIC images for all specimens and was the final failure mechanism for all specimens except, CC_1-8J, H_1-8J, H_1-12J and H_1-18J. For these specimens DIC images indicated the presence of near surface delaminations that allowed formation of local buckles under compressive loading which subsequently caused delamination propagation thus weakening the laminate and causing failure. The local buckling and delamination propagation seen in the above laminates meant it was possible to apply the analytical Strip model. Analytically predicted stresses were within 4%, 2%, 10% and 15% of the experimental values for CC_1-8J, H_1-8J, H_1-12J and H_1-18J, respectively, demonstrating the applicability of the modelling methodology to hybrid laminates.

In contrast to the CC_1 and H_1 laminates, a comparison of DIC images and load vs. strain plots for the fully CFRP laminates indicates an anti-symmetric global buckling mode caused the failure of CC_2 and CC_3 at reduced levels of applied stress. It is believed this anti-symmetric mode was promoted by through-thickness shear deformation at the centre of the damaged laminate. This mode is thought to have been enabled by intraply cracking in the 90^o plies allowing the laminate to deform much more easily than would be allowed by the intact central 0^o plies in the hybrid laminates. It is thought this mechanism did not occur in the CC_1 specimen due to the lower impact energy sustained by this laminate producing less damage.

As a consequence of the combination of GFRP layers and damage tolerant stacking sequences in the hybrid laminates H_2, H_3, H_4 and H_5 delamination was contained to a through-thickness region near the mid-plane of the laminate. By constraining delamination formation during impact to the centre of the laminate hybrid laminates H_2, H_3, H_4 and H_5 firstly prevented local buckling and thus delamination propagation and secondly delayed global buckling by keeping the outer layers adhered thus maintaining the bending stiffness of the laminate. Table 5 clearly indicates that hybrid laminates H_2, H_3, H_4 and H_5 have the potential to offer improvements of up to 32% in damage tolerant strength compared with the CFRP laminates of similar stacking sequence and similar

impact energies. Although specimen H_5-12J failed at a higher stress than the strongest CFRP laminate CC_1-8J despite being subject to a 50% higher energy impact. Note also that the H_3-18J specimen failed at only 4% lower stress than the CC_1-8J specimen despite impact energy about 2 times that received by the CC_1-8J specimen. A comparison of results in Table 5 and Table 3 shows that local buckling propagation can be prevented via stacking sequence selection in combination with the addition of GFRP plies and that this combination led to hybrid laminates outperforming carbon laminates.

The results in Table 5 shows that increased impact energy had little effect on the maximum stress to failure of the hybrid laminates in contrast to the CFRP laminates where an increase in impact energy produced a considerably lower failure stress due to a change in failure mechanism.

5 The Effect of Ply Blocking on Near-edge and On-edge Impact Damage Mechanisms

5.1 Introduction

Due to the serious reduction in residual strength, the impact damage of CFRP laminates has drawn huge attention for both academia and the aerospace industry to conduct extensive research into this area [146-159]. Barely Visible Impact Damage (BVID) has been considered to be particularly crucial due to the difficulty of detection in service.

Although some existing theories have revealed damage formation of composite laminates, there is still limited understanding in impact damage morphology mechanisms especially in near-edge and on-edge impact [151, 152, 155-158]. This has become the motivation of conducting research in this chapter.

Non-destructive testing (NDT) techniques, such as C-scan and X-ray Computed Tomography (XRCT), can provide insight into internal damage formation. NDT of damaged laminates has been widely used to post-test analysis of unloaded coupons [146,147,160]. However, the delaminations and intra-ply cracks close when load is removed, some information is not captured in standard NDT which makes it difficult to find out mechanisms causing damage morphology. This is partially a consequence of the dynamic nature of impact and partially a consequence of the comparatively long scan-times.

However, at the low velocities at which BVID typically forms, laminate response is dominated by the lowest mode shape implying that load, deflection and hence, the strain are effectively in the same phase. As such, quasi-static loading is a good approximation of the low velocity impacts that typically produce BVID [148-150]. In this research, a novel rig for in-situ XRCT imaging of laminates under out-of-plane near edge indentation is used to capture quasi-static impact damage progression through incremental scanning and loading of a blocked stacking sequence $[(\pm45)_3(0_3/90)_2/0_2]_S$ laminate and dispersed stacking sequence laminate $[(\pm45/0_2/90/0_2)_2/\pm45]_S$.

In this chapter, low-velocity dynamic impact is conducted on both blocked and dispersed laminates at near-edge and on-edge location. In order to easily access the internal damage, extra coupons are manufactured with glass fibre for both stacking sequences. Another set of experiment is employed to conduct in-situ XRCT. This provides an opportunity to investigate the initiation of impact damage and damage morphology.

5.2 Experimental method

5.2.1 Laminate manufacture and stacking sequence selection

Laminate ID	Lay-up	Impact type	Size
$CFRPA_{Reg,NE}$		Near Edge	150 x 50 mm
$CFRPA_{Reg,OE}$	$[(\pm45/0_2/90/0_2)_2/\pm45]_S$	On Edge	150 x 50 mm
$GFRPA_{Reg,OE}$		On Edge	150 x 50 mm
$CFRPB_{Reg,NE}$		Near Edge	150 x 50 mm
$CFRPB_{Reg,OE}$	$[(\pm45)_3(0_3/90)_2/0_2]_S$	On Edge	150 x 50 mm
$GFRPB_{Reg,OE}$		On Edge	150 x 50 mm
$CFRPA_{Semi,NE}$	$[(\pm45/0_2/90/0_2)_2/\pm45]_S$	Near Edge	100 mm Semi-circle
$CFRPB_{Semi,NE}$	$[(\pm45)_3(0_3/90)_2/0_2]_S$	Near Edge	100 mm Semi-circle
$GFRPB_{Semi,NE}$	$[(\pm45)_3(0_3/90)_2/0_2]_S$	Near Edge	100 mm Semi-circle

Table 6 *Coupon ID and stacking sequence: the subscript Reg describes coupon is rectangular shape, Semi is for semi-circular, NE is near-edge impact, OE is on-edge impact.*

Material	E_{11} (GPa)	E_{22} (GPa)	G_{12} (GPa)	ν_{12}	t (mm)	G_{1C} (J/m^2)
M21/T800	172	8.9	4.2	0.35	0.25	-

Table 7 *Material properties.*

The blocked stacking sequence, $[(\pm45)_3(0_3/90)_2/0_2]_S$, contains ±45º fibre at outer surface and blocked 0º fibre at mid core. The dispersed stacking sequence, $[(\pm45/0_2/90/0_2)_2/\pm45]_S$, uses ±45º dispersing 0º. These two stacking sequences are specially designed to investigate the effect of blocking angles to damage formation in near-edge and on-edge impact. Both stacking sequences are manufactured into full carbon coupon and full glass coupon. The glass coupons are designed to provide better visual access to damage formation since the material has transparent property. For each stacking sequence, the coupon is manifested in rectangular size of 150 x 50 mm and receives out-of-plane on-edge and near-edge dynamic impact. A special set of coupons is manufactured approximately semi-circular to allow investigation of out-of-plane near-edge quasi-static impact. This set of coupons will receive in-situ quasi-static

impact and XRCT to closely look at the damage initiation and damage morphology.

Each coupon has a 32-ply stacking sequence presented in Table 6 and geometry defined in Figure 22 (a). All samples were manufactured from M21/T800, unidirectional CFRP prepreg with ply thickness 0.25mm resulting in a full laminate thickness of 8mm. The material properties are presented in Table 7.

5.2.2 On-edge and near-edge dynamic impact set up

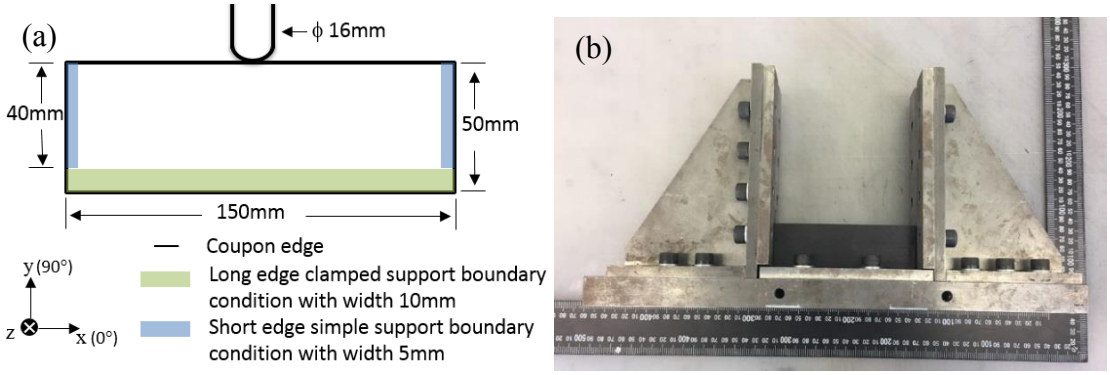

Figure 22 *On-edge dynamic impact set up. (a) shows the boundary conditions under dynamic impact test and (b) shows test rig set up.*

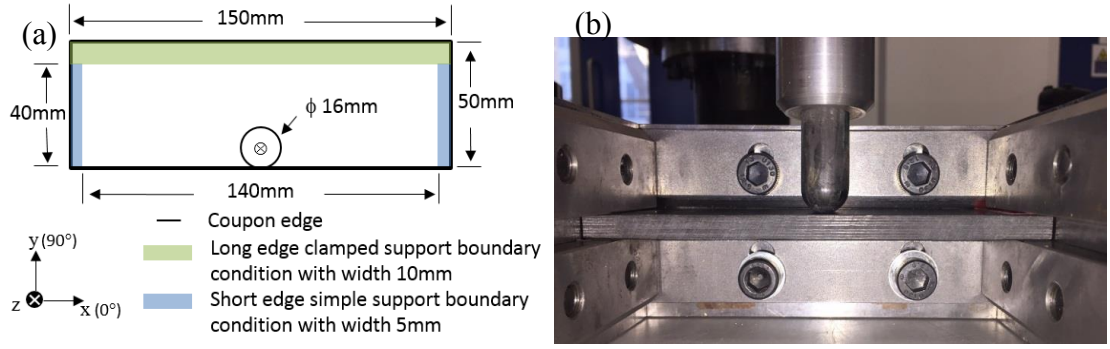

Figure 23 *Near-edge dynamic impact set up. (a) shows the boundary conditions under dynamic impact test and (b) shows test rig set up.*

As above figure 22 shows an impactor of 16mm diameter directly impacts on coupon long edge. The coupon has two short edges simply supported and bottom long edge fully clamped. For near-edge impact, the bottom long edge and two short edges are set up same way as on-edge impact as figure 23 shows. But the impactor is located at free long edge and provides out-of-plane impact.

5.2.3 X-ray computed tomography (XRCT)

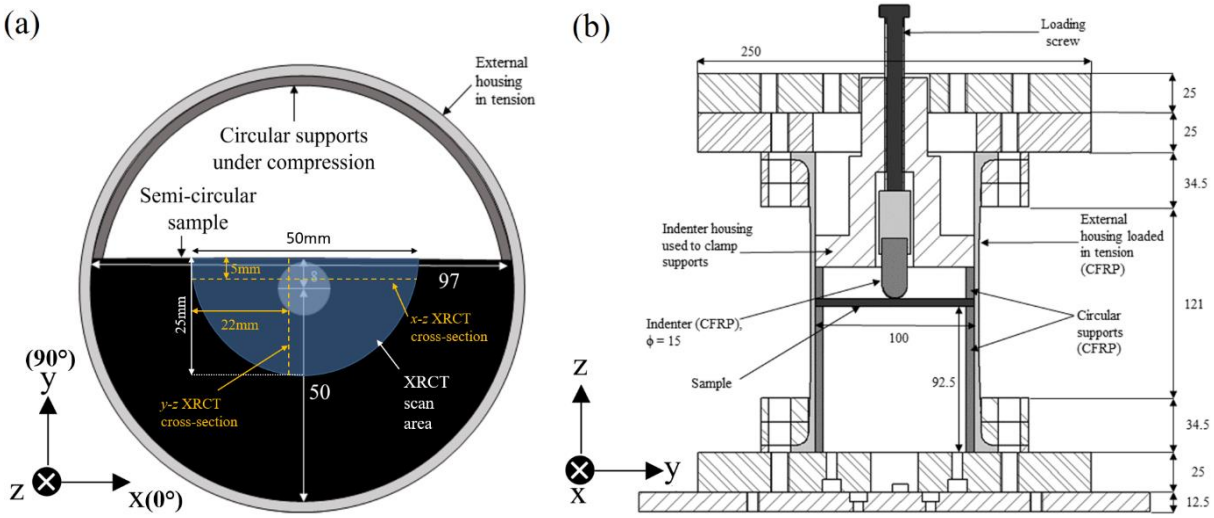

Figure 24 *(a) x-y plane cross sectional view of the jig showing supports, indenter and coupon; (b) z-y cross-section of the load stage showing coupon placement and load stage construction.*

The in-situ XRCT loading rig is shown in Figure 24 (b). A loading screw is used to apply incremental increases in indenter displacement. Each displacement is held for 255 minutes, the time required to XRCT scan the sample. In order to capture the order of damage progression, the coupon was scanned under zero load and then at multiple indenter displacements with damage being detected at displacements of 3.1mm, 4.2mm and 5.4mm; displacement being measured using measurements of the displacement of the loading screw relative to the rig surface. It is noted that no evidence of rigid body movement of the sample relative to its fixture was noted during scanning and that the loading stage remained locked in position in the XRCT scanner throughout all applications of load. Displacement was halted after either audible cracking or after 1mm displacement steps. XRCT scans were taken using a Nikon XT H 225 ST CT scanner with a Tungsten target and Perkin Elmer 1620 16-bit, 2000 by 2000-pixel detector. The system has a 225kV micro focus source with a minimum 3µm spot size. Between 2033 and 3141 projections (with 4-8 averages per projection) were taken per scan with each projection being a composite of the average of 4 images. Images were taken with 708ms exposures under x-ray conditions of 155kV and 150 µA.

5.3 Results

On-edge dynamic impact

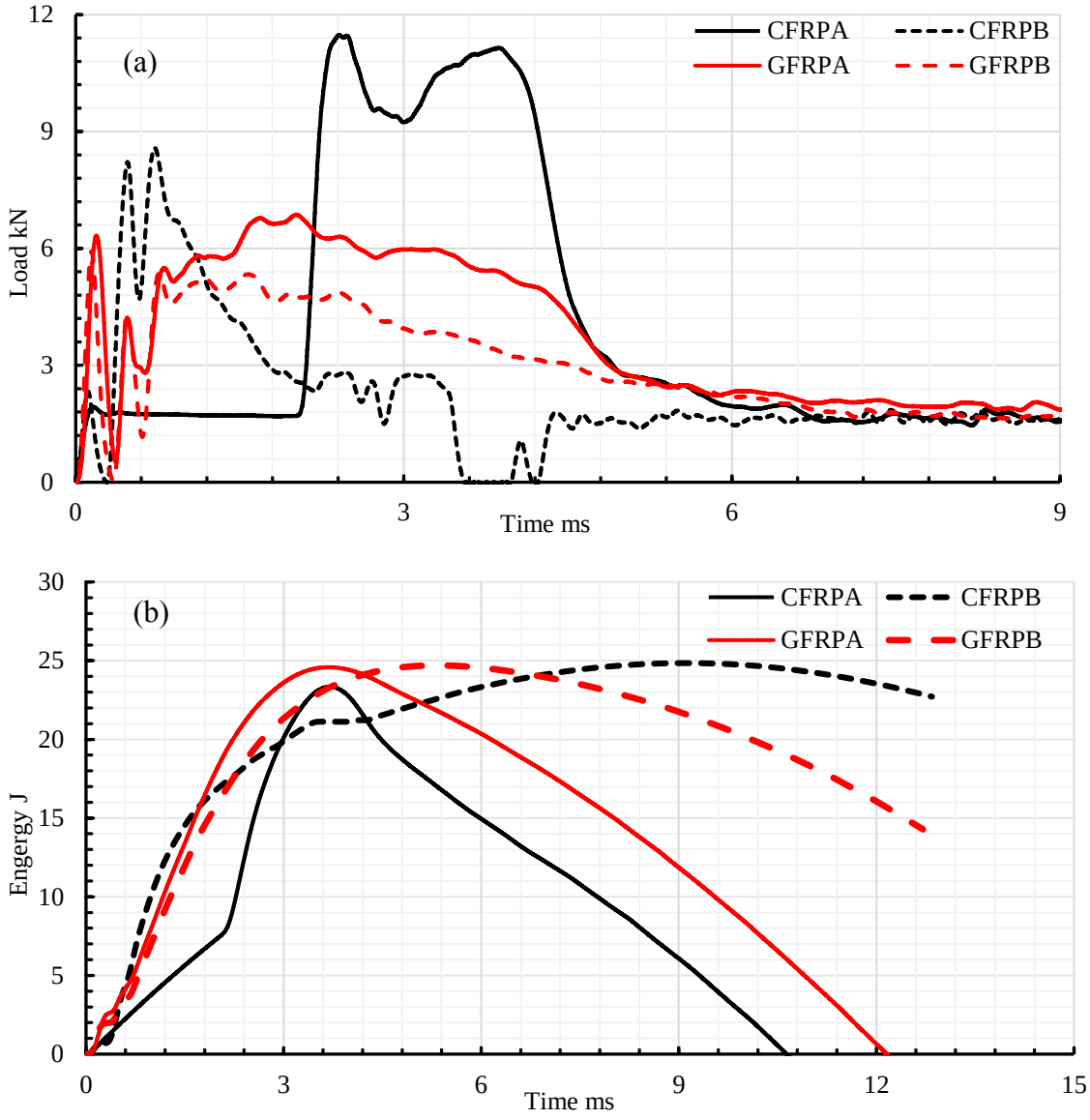

Figure 25 *(a) On-edge dynamic impact load-time history and (b) energy-time history for* $CFRPA_{Reg,OE}$, $CFRPB_{Reg,OE}$, $GFRPA_{Reg,OE}$, $GFRPB_{Reg,OE}$ *at 25J impact energy.*

Figure 25 shows (a) the relationship of impact load and time, (b) impact energy and time for CFRPA/$B_{Reg,OE}$ and GFRPA/$B_{Reg,OE}$. The black and red lines present carbon and glass samples, solid and dashed lines present stacking sequence A and B respectively.

In figure 25 (a), the glass samples show good agreement for impact load between both A, dispersed and B, blocked designs. Though the carbon samples show same impact

behaviour, the load peaks at different time and magnitude. The reason for peaking differently is due to the impact point on edge slightly off centre. Impactor hits slightly toward one side for $CFRPA_{Reg,OE}$, which causes a low load-time response due to impactor sliding at contact moment. The glass samples pick up load after peaks for both A and B design. Contrarily, the carbon samples react impact differently; the load drops and remains low after peaking. Generally, carbon samples reach higher impact load level than glass samples due to the material nature is stiffer and less deformable ability. The position where curve kinks show the delamination and damage occur. More details will be presented in following content.

The relation between energy and time is shown in figure 25 (b). All samples act similarly as energy increases but split in different ending. The dispersed design shows good agreement for both carbon and glass samples. Energy reaches maximum at about 3.5ms after impact contact and decreases to 0 at 11 and 12ms respectively as the solid black and red lines indicate. Unlike this tendency, $CFRPB_{Reg,OE}$ keeps receiving more energy after the first drop and impact is stopped by machine hydraulic stopping device. $GFRPB_{Reg,OE}$ peaks and decreases as same as $CFRPA_{Reg,OE}$ but also stopped by impact safety mechanism where the energy does not return to 0.

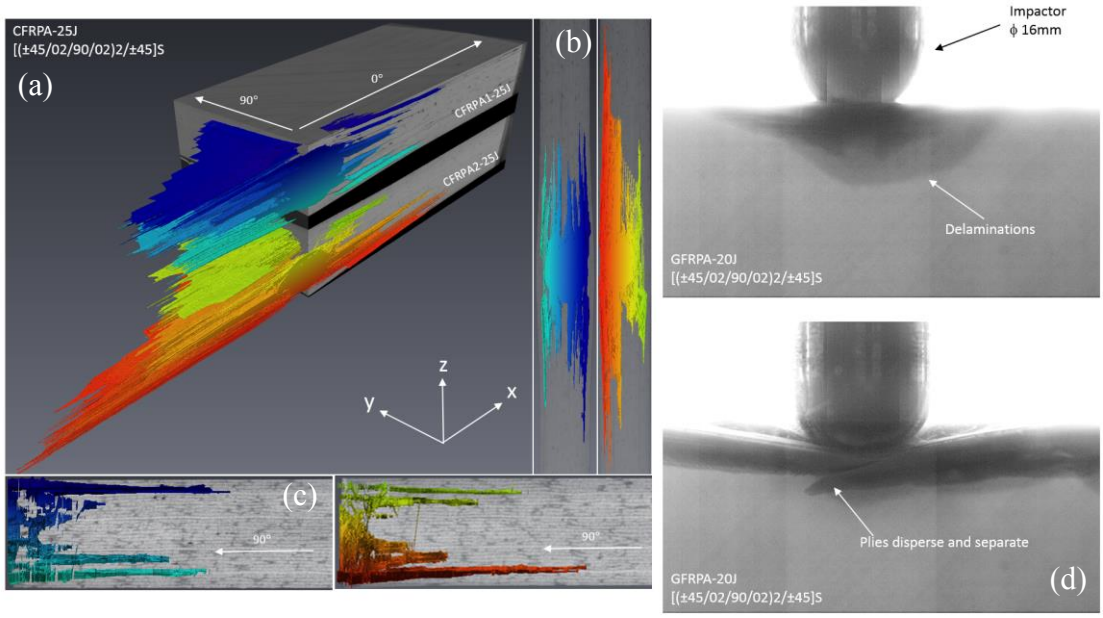

Figure 26 *XRCT scan images and high-speed camera images for* $CFRPA_{Reg,OE}$ *and* $GFRPA_{Reg,OE}$ *under 25J on-edge dynamic impact. (a) coloured damage for 3d view. (b) coloured damage for long edge side view. (c) coloured damage for short edge side view. (d) high speed image showing damage propagation.*

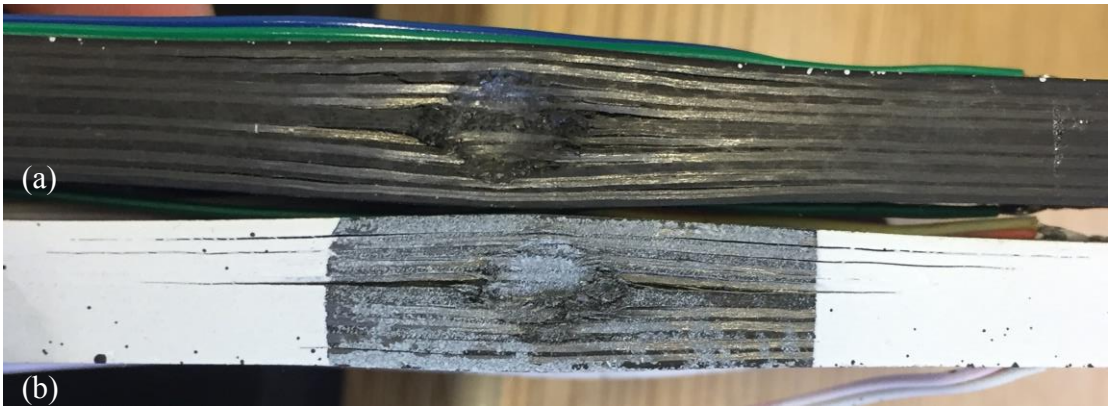

Figure 27 *On-edge dynamic impact dent for* $CFRPA_{Reg,OE}$ *under 25J impact energy. (a) impactor hits right in the middle. (b) impactor hits slightly off set toward one side.*

Figure 26 shows the XRCT scan images and high-speed camera images for $CFRPA_{Reg,OE}$ and $GFRPA_{Reg,OE}$ under 25J on-edge dynamic impact. Due to time consumption, only dispersed design is XRCT scanned. (a), (b) and (c) present the internal damage caused by on-edge impact from 3D and two side views. (d) is taken using high speed camera captures the damage propagation during the impact for full

glass coupon. The strong light shines through glass material and allow high speed camera recording the whole impact process.

For the dispersed coupon $CFRPA_{Reg,OE}$, $[(\pm45/0_2/90/0_2)_2/\pm45]_S$, the damaged area have been coloured out. The colour contour indicates different depth from one surface to another. As figure 26 (c) shows, the on-edge impact damage coupon widely thought thickness. The delamination occurs at every interface. Noticeably, the large delamination occurs towards coupon outer surface and the damage size decreases towards to middle core. For layers underneath the impactor, the direct impact load squashes the material and causes a dent as figure 27 shows. The adjacent layers are pushed away and cause delaminations. The further away from the centre, the bigger delamination is. To keep the experimental repeatability, this on-edge impact test contains two sets of coupons. As can see in Figure 26, the delamination in red is bigger than delamination in blue. This is a result of impactor sliding as Figure 27 shows where (a) is coupon impacted directly in the centre and (b) is impacted slightly toward one side. This off-set leads to a bigger delamination by push layers further away in one side to cause a greater damage than another side.

Figure 26 (d) shows the initiation of damage when impactor contacted the edge of $GFRPA_{Reg,OE}$ and the damage propagated when impactor fully delivered 20J energy, which is captured by high-speed camera. During this impact process, the damage initiates at the outer surface and grow and separate as impact energy fully absorbed.

Near-edge dynamic impact

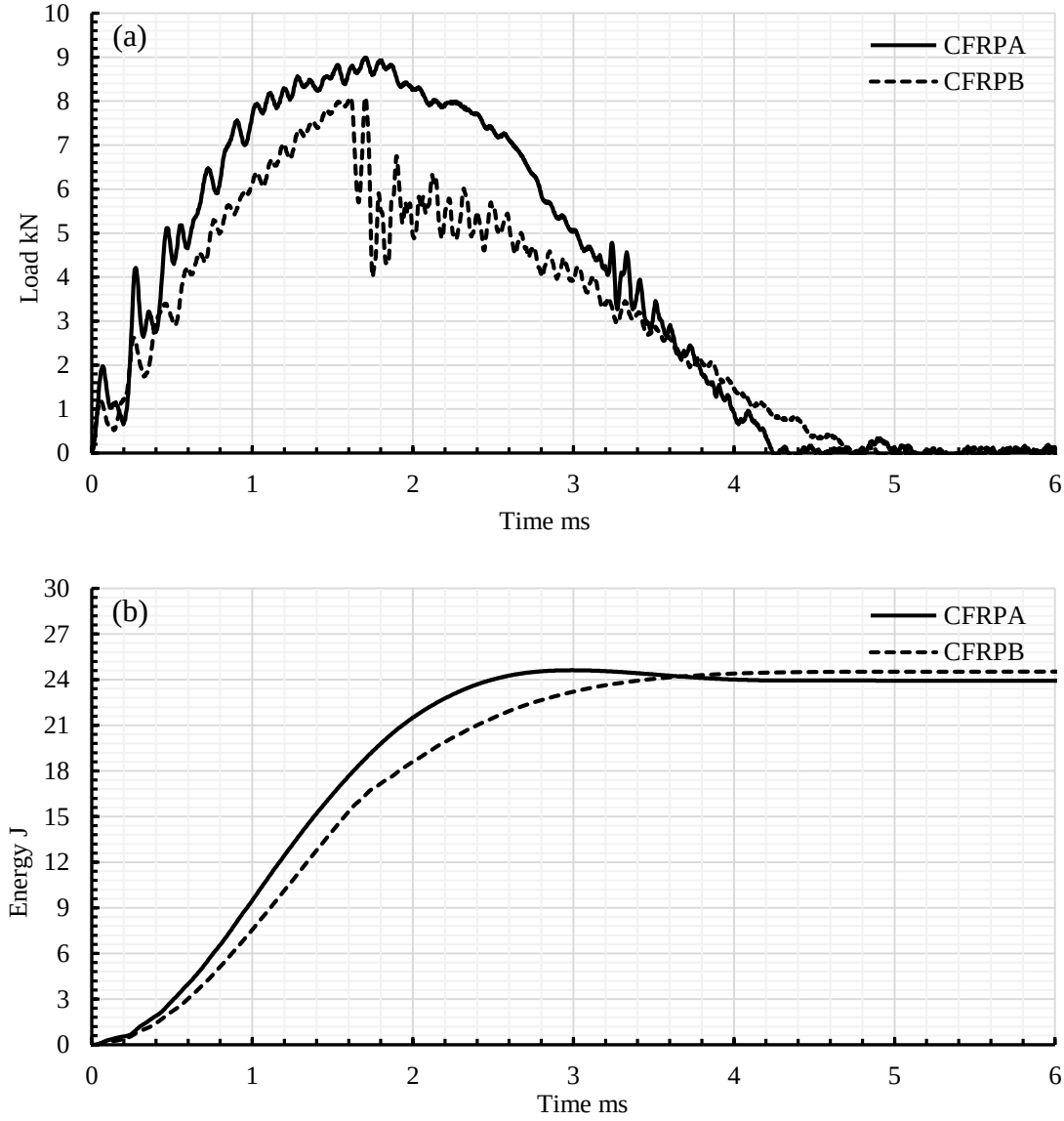

Figure 28 *a) Near-edge dynamic impact load-time history and (b) energy-time history for* $CFRPA_{Reg,NE}$ *and* $CFRPB_{Reg,NE}$.

Near-edge dynamic impact time history is presented in Figure 28. Due to the extremely weak material property of glass in out-of-plane direction, only carbon samples are impacted for near-edge tests. The solid and dashed line present dispersed design $[(\pm 45/0_2/90/0_2)_2/\pm 45]_S$ and blocked design $[(\pm 45)_3(0_3/90)_2/0_2]_S$ respectively.

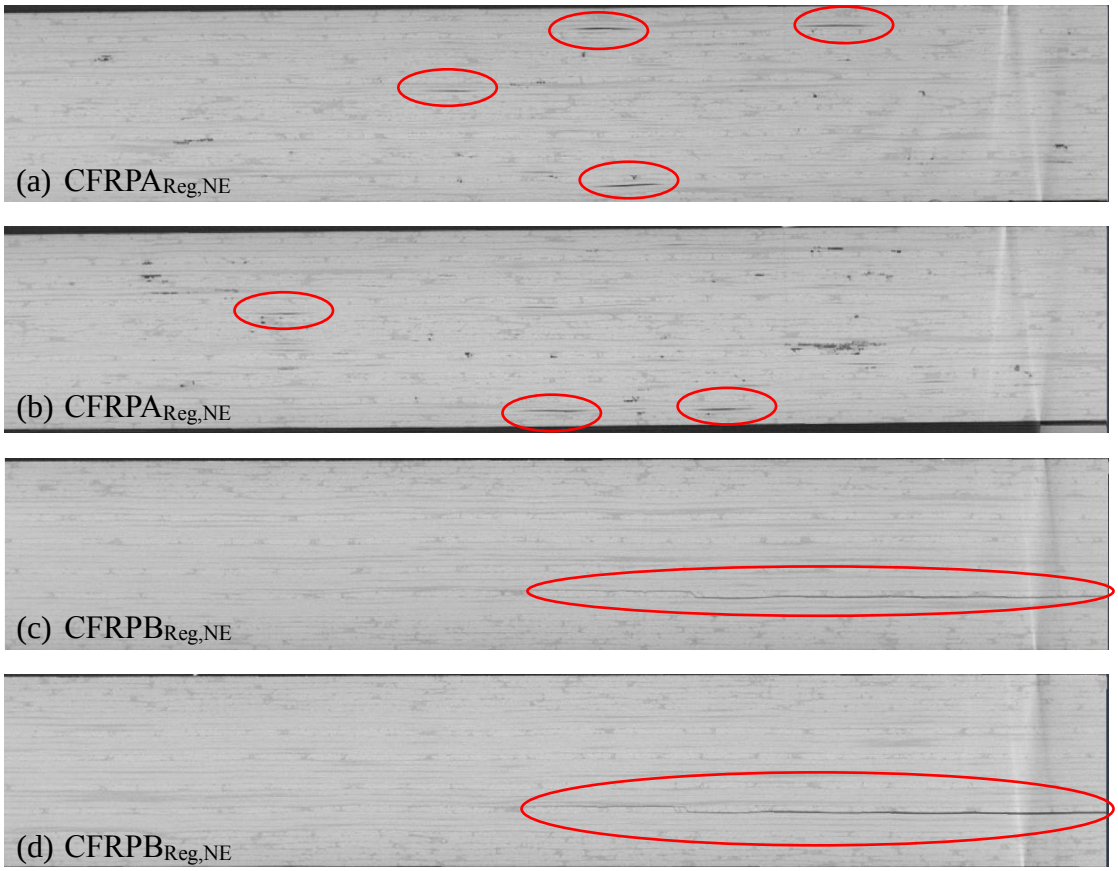

Figure 29 *XRCT scan images for CFRPA$_{Reg,NE}$ and CFRPB$_{Reg,NE}$ under 25J near-edge dynamic impact. Delaminations are circled in red. (a) and (b) are long edge cross sections for CFRPA$_{Reg,NE}$. (c) and (d) are taken are long edge cross sections for CFRPB$_{Reg,NE}$. (c) and (d) are taken from long edge cross sections for CFRPB$_{Reg, NE}$.*

Figure 28 (a) shows a good agreement for both sample that load decreases after peaking in the middle. But the blocked design drops immediately after 2.6 ms where dispersed design decreases gradually. This is due to a big delamination occurs at blocked design in the middle core as Figure 29 (c) and (d) shows below. Both dispersed and blocked design are noisy at the beginning of load increasing period and the blocked design gets very noisy directly after peaking where the dispersed design keeps smooth and becomes noisy when the load approaches 0. This is because, unlike the blocked design, the dispersed design forms multiple minor cracks and delaminations all the way through coupon thickness as circled in Figure 29 (a) and (b).

Figure 29 shows XRCT scan images for CFRPA$_{Reg,NE}$ and CFRPB$_{Reg,NE}$ under 25J near-edge dynamic impact. The images are taken from coupon long edge cross sections. (a)

and (b) contains multiple minor delaminations located at different interfaces for the dispersed design $CFRPA_{Reg,NE}$. The blocked design $CFRPB_{Reg,NE}$ only shows a big delamination at middle core.

In-situ static indentation

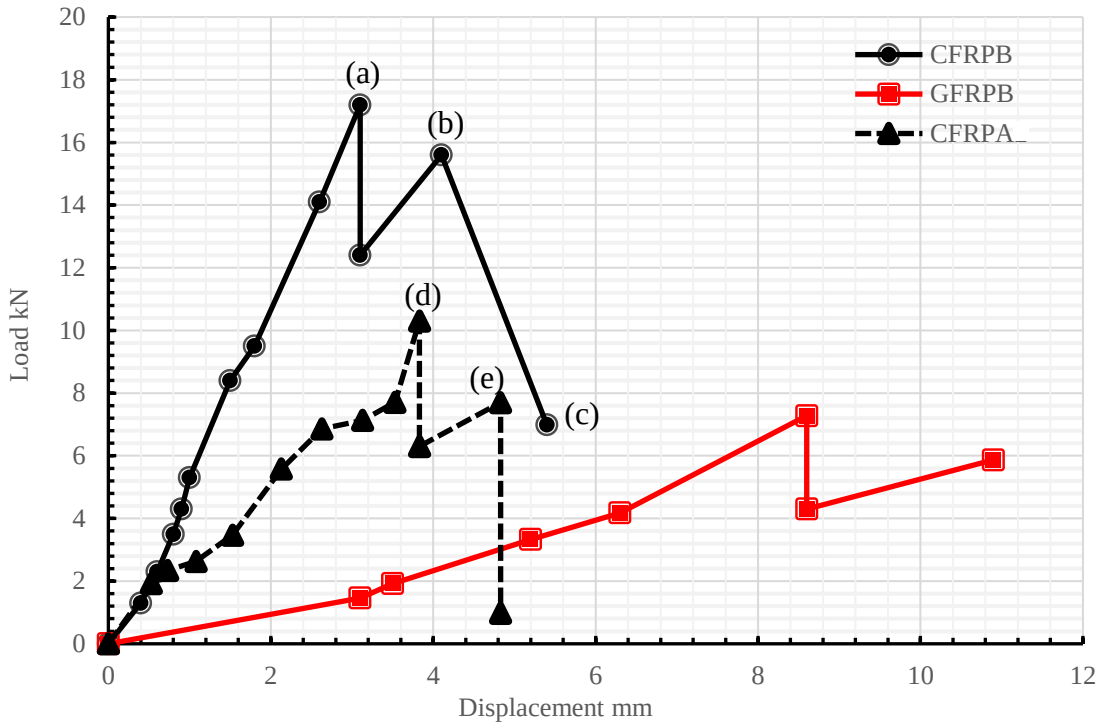

Figure 30 *Load-displacement curve for* $CFRPA_{Semi,NE}$, $CFRPB_{Semi,NE}$ *and* $GFRPB_{Semi,NE}$ *in in-situ static indentation tests.*

The above Figure 30 is a comparison of load vs. displacement for $CFRPA_{Semi,NE}$, $CFRPB_{Semi,NE}$ and $GFRPB_{Semi,NE}$. The black solid and dashed lines present carbon blocked and dispersed designs. The red solid lines present glass blocked design. The in-situ static indentation uses displacement as a control to scan and find out damage morphology at each displacement increment.

All three curves show same tendency that load suddenly drops at the maximum due to major delamination occurs. The glass sample due to its low material property, the curve is much lower the full carbon samples. The blocked $CFRPB_{Semi,NE}$, $[(\pm45)_3(0_3/90)_2/0_2]_S$, shows a stiffer behaviour than the dispersed $CFRPA_{Semi,NE}$, $[(\pm45/0_2/90/0_2)_2/\pm45]_S$, before the major delamination occurs. The dispersed design is less stiff due to multiple

minor cracks and delaminations occur before the major delaminations, which can be seen in Figure 31 and Figure 32. The blocked $CFRPB_{Semi,NE}$

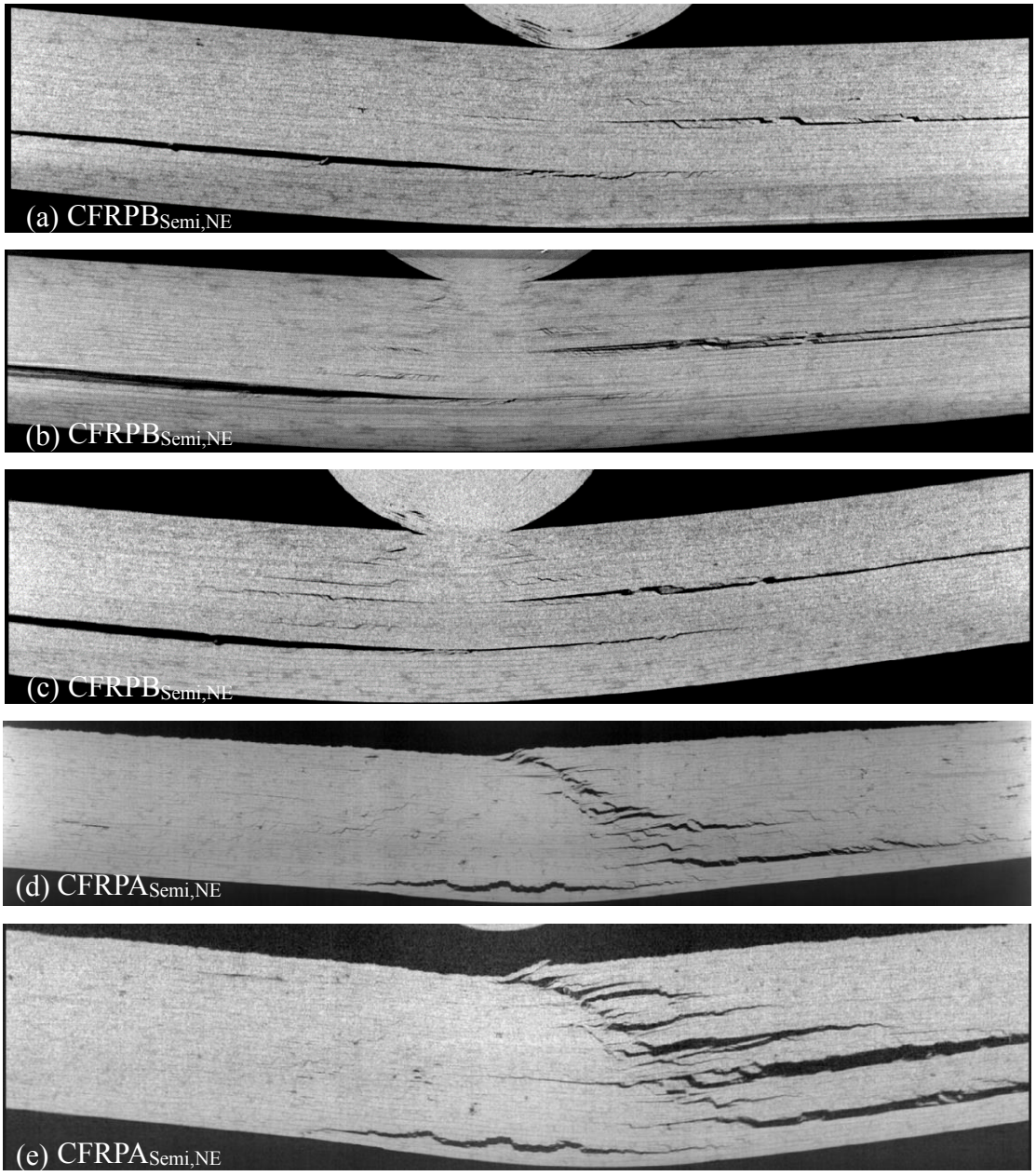

Figure 31 *XRCT scan images from long edge cross section for $CFRPA_{Semi,NE}$ and $CFRPB_{Semi,NE}$ under near-edge in-situ static indentation. (a) 17.2kN, (b) 15.6kN, (c) 7kN, (d)10.2kN and (e) 7.8kN.*

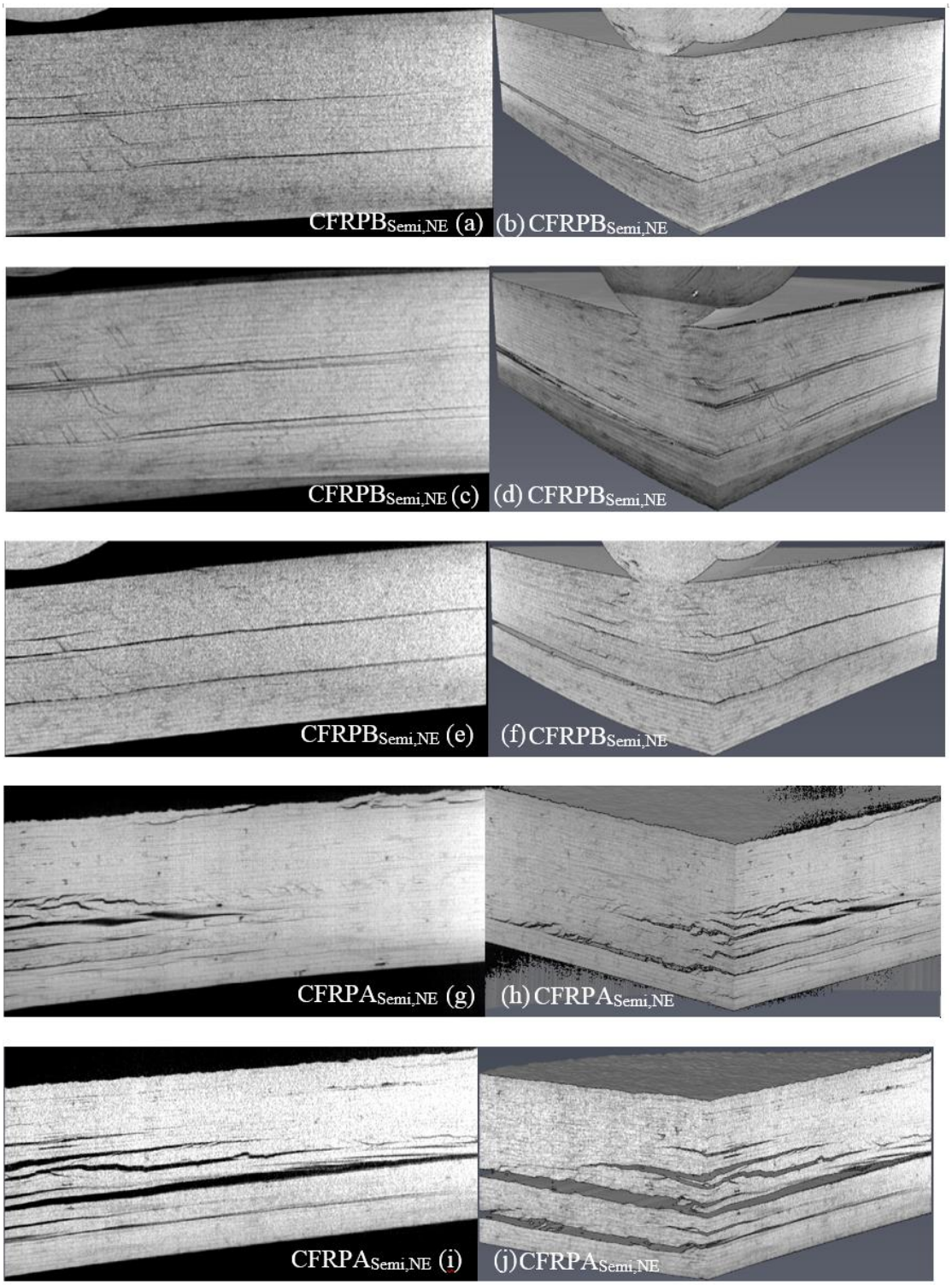

Figure 32 *XRCT scan images from short edge cross section and 3D view for* $CFRPA_{Semi,NE}$ *and* $CFRPB_{Semi,NE}$ *under near-edge in-situ static indentation. (a),(b) 17.2kN, (c), (d) 15.6kN, (e), (f)7kN, (g), (h) 10.2kN and (i), (j) 7.8kN.*

Figure 31 and Figure 32 show the XRCT scan from long edge, short edge cross section

and 3D view of in-situ static indentation for $CFRPA_{Semi,NE}$ and $CFRPB_{Semi,NE}$. These scans present five different loading stages where delaminations initiate and propagate in individual ply interfaces at 17.2kN, 15.6kN, 7kN, 10.2kN and 7.8kN.

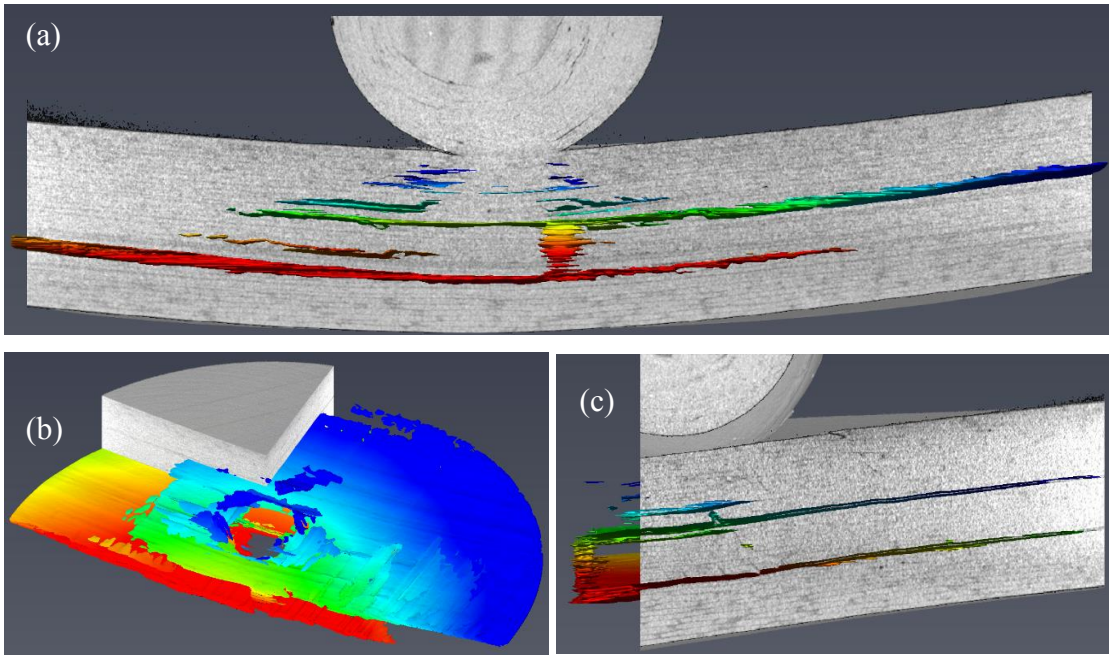

Figure 33 *Coloured damage in $CFRPB_{Semi,NE}$ [(±45)3(03/90)2/02]S (a) Cross sectional view from long edge with laminate material present. Centre cross section from short edge of damage (b) without laminate (c) with laminate.*

The damage are coloured out to easily identify damaged position as Figure 33 and Figure 34 show where colour contour indicates through thickness depth from indentation surface to non-indentation surface.

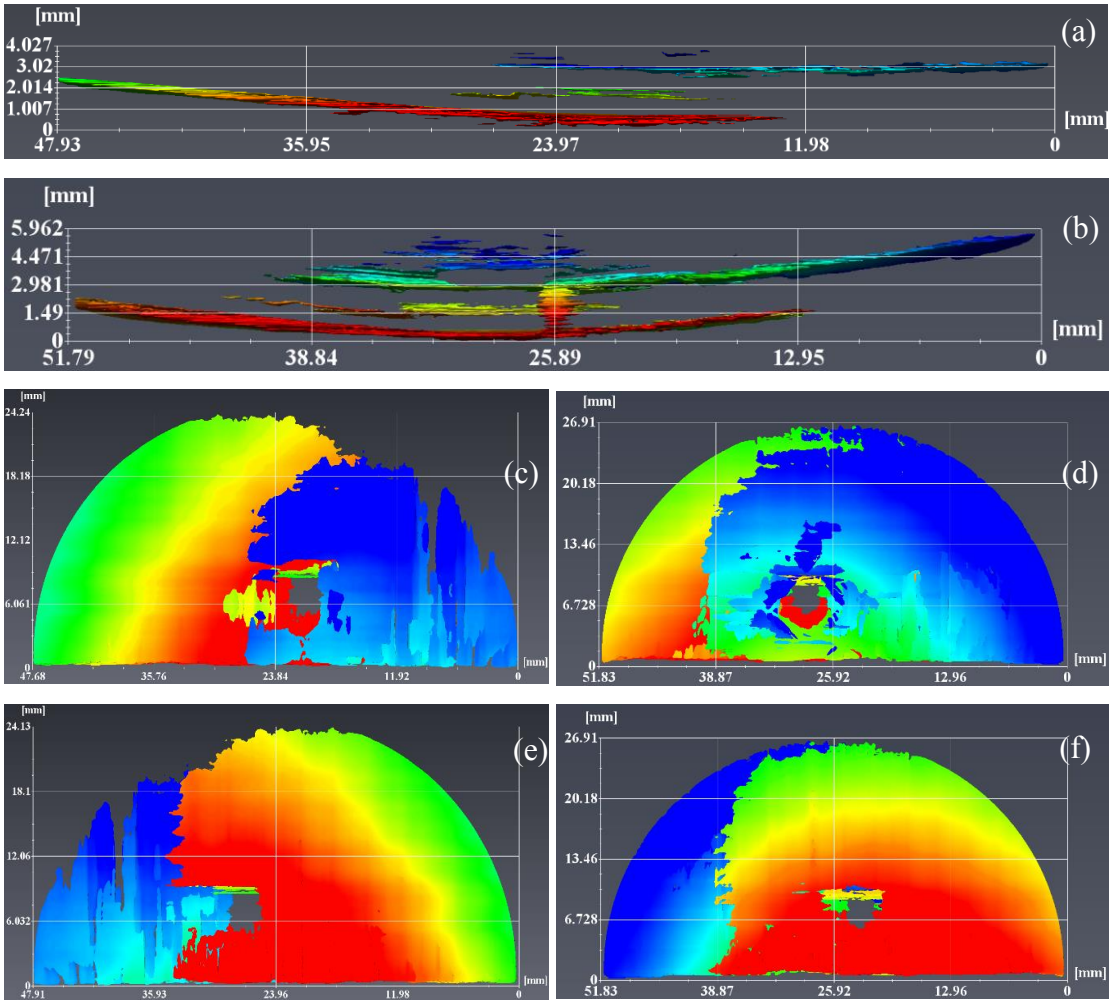

Figure 34 *Coloured damage from long edge of CFRPB$_{Semi,NE}$ at (a) 17.2kN and (b)7kN. Plan view of damage from indentation surface at (c) 17.2kN and (d) 7kN and non-indentation surface at (e) 17.2kN and (f) 7kN.*

5.4 Discussions

In Figure 26, the on-edge dynamic impact causes multiple minor and major delaminations through entire thickness. The major damage are shallow and occur in both close surface position. This is due to compression of core layers and impactor pushing and splitting outer layers. The major delaminations have a potential threat to cause buckling and structure failure in compression after impact testing. Comparing to Figure 27, the near-edge dynamic impact induces less damage and cracks than Figure 26. Especially for the blocked design $CFRPB_{Reg,NE}$, $[(\pm45)_3(0_3/90)_2/0_2]_S$, the delamination occurs and is controlled in the middle core where requires more energy to propagate damage and buckle.

In Figure 31 and Figure 32, the blocked design $CFRPB_{Semi,NE}$, $[(\pm45)_3(0_3/90)_2/0_2]_S$, contains delamination and cracks at middle core at interface 0/90. Only a few minor cracks occur underneath the indenter. However, under the same loading condition, the dispersed design $CFRPA_{Semi,NE}$, $[(\pm45/0_2/90/0_2)_2/\pm45]_S$, has delaminations and cracks through entire sample thickness. With increasing load, these damage propagate and join to form major delaminations. Particularly the big and shallow delamination occurs at the non-indentation surface as shown in Figure 31 (d) which is highly possible to reduce residual stiffness significantly in compression after impact test.

In Figure 32 and 33, the damage are coloured out for blocked design $CFRPB_{Semi,NE}$ to show delamination position. These two delaminations are not symmetrical to each other. The damage only propagates toward one side. This phenomenon can also be observed for dispersed design in Figure 31. This is a resultant of imperfect loading condition and delaminated carbon indenter. As Figure 24 (b) shows, the testing sample is held by two pieces of carbon cylinders which are contained by the jig top lid. The top lid is sealed by controlling the screws which might not be balanced to cause the testing sample loaded unevenly. In order to make sure the XRCT image quantity, the indenter is made of carbon to allow x-ray goes through. The indenter is easily delaminated in high loading condition which is also a reason of unbalanced loading.

5.5 Conclusions and Future Works

As the previous results show, the on-edge dynamic impact causes more damage than near-edge dynamic impact. The potentials stiffness reduction in compression after impact will make on-edge area less damage resistant and damage tolerant for aircraft components and structures.

The blocked design, $[(\pm 45)_3(0_3/90)_2/0_2]_S$, can contain delaminations and cracks in the middle region in testing samples, which will increase residual stiffness and make aircraft structure more damage tolerant than the dispersed design $[(\pm 45/0_2/90/0_2)_2/\pm 45]_S$.

The works suggested in future is to conduct compression after impact test for dynamic impacted on-edge and near-edge samples. This will allow better understanding on the effect of blocked and dispersed stacking sequence for on-edge and near-edge impact.

6 Conclusions and Future Works

6.1 Conclusion

The experiments conducted in this work provide benchmark test results for comparison of CAI damage tolerance and damage resistance properties of CFRP and CFRP/GFRP hybrid laminates that can be used to validate other analytical models in future.

Hybrid laminates are shown to display increases in structural efficiency of up to 32% in comparison to CFRP laminates with identical impact energies. The extent to which the hybrid laminates outperformed the CFRP laminates in the CAI tests was dependent on the stacking sequence and through-thickness positioning of glass layers. Laminates displaying the highest stresses at failure were those that exploited the above to prevent delamination from occurring close to the outer surface during impact. This in turn prevented local sub-laminate buckling under compression and hence prevented failures due to delamination propagation. A change from a symmetric to an anti-symmetric global buckling failure noted in some of the CFRP laminates subject to higher energy impacts was not displayed by the hybrid designs.

However, this must be considered in the context of BVID which is described by dent depth and diameter. It may be the case that BVID is reached for carbon coupons at a lower impact energy than for hybrid coupons and thus an impact energy comparison may be invalid. Some coupons failed at a higher stress than the strongest CFRP laminate despite being subject to 50% higher energy impact.

By adding GFRP lamina to CFRP laminates, the impact damage were integrated and drawn away from specimen outer surface which displays improvement of damage resistance, and the failure stress was increased by 32% in CAI to show the damage tolerance is much improved.

The on-edge dynamic impact causes more damage than near-edge dynamic impact. The potentials stiffness reduction in compression after impact will make on-edge area less damage resistant and damage tolerant for aircraft components and structures.

The blocked design, $[(\pm 45)_3(0_3/90)_2/0_2]_S$, can contain delaminations and cracks in the

middle region in testing samples, which will increase residual stiffness and make aircraft structure more damage tolerant than the dispersed design $[(\pm 45/0_2/90/0_2)_2/\pm 45]_S$.

6.2 Future Work

In this work, a preliminary analytical was developed to investigate the influence of GFRP lamina in CFRP laminates. The preliminary analytical model was purely based on through-thickness shear stress where several effects had be neglected. The assumption made in analytical model is using constant deflection for both orthogonal strips under different resultant forces. It is much simplified and ideal comparing with realistic impact test. For work in next stage, an energy equilibrium method is suggested to carry on. The energy method assumes for both strips receive the equal impact energy which provides energy equilibrium between strips. For the disagreement of the maximum shear stress in X and Y direction, the twisting effect known as term D_{33} should be taken into consideration. The following list shows the some other effects will be looked into in analytical model:

- Intra-ply cracking effects
- Dynamic effects
- Twisting effects D_{33}
- Shear stress for resin rich zone

For the analytical energy model for quasi-static test, a more realistic boundary conditions are suggested to be used. In order to save computing time, it is suggested that the displacement and rotation at section joints needs to be eliminated before substituting into energy equations. It can be done by equating shape functions that sharing same degrees of freedom at section joints. Another way to optimise the analytical model is replacing cubic shape function with high order sin or cos equations, which could clearly present degrees of freedom such as rotation and amplitude.

A more complicated FEA impact simulation with cohesive elements is suggested to build, which will produce more realistic through-thickness shear stress.

In order to achieve the targets above, a deeper research of impact modelling and damage formation modelling is suggested to conduct, including impact contact modelling, inter-

laminar cohesive layers, mesh types and methods for impact modelling and impactor loading study. The study of analytical model is also missing from this literature review. In order to provide a comprehensive chapter of analytical model for damage resistance and damage tolerance, a review of through-thickness shear stress and damage propagation is required to provide.

7 References

[1] Bibo GA, Hogg PJ. The role of resinforcement architecture on impact damage mechanisms and post-impact compression behaviour 1996; 31:1115–37.

[2] Hancox NL. Izod impact testing of carbon-fibre-reinforced plastics. Composites 1971; 2:41–5.

[3] Bader MG, Ellis RM. The effect of notches and specimen geometry on the pendulum impact strength of uniaxial CFRP. Composites 1974; 5:253–8.

[4] Lawrence J. Broutman et al. Impact strength and toughness of fibre composite materials. Air Force Office of Scientific Research 1972.

[5] Running DM, Ligon JB, Miskioglu I. An experimental study of low velocity impact damage in woven fiber composites. Journal of Composite Materials 1999; 33:928–40.

[6] Mouritz AP, Cox BN. A mechanistic interpretation of the comparative in-plane mechanical properties of 3D woven, stitched and pinned composites. Composites Part A: Applied Science and Manufacturing 2010; 41:709–28.

[7] Dransfield K, Baillie C, Mai Y. Improving the delamination resistance of CFRP by stitching—a review. Composites Science and Technology 1994; 50:305–17.

[8] Naik N., Ramasimha R, Arya H, Prabhu S., ShamaRao N. Impact response and damage tolerance characteristics of glass–carbon/epoxy hybrid composite plates. Composites Part B: Engineering 2001; 32:565–74.

[9] Fan J, Guan Z, Cantwell WJ. Structural behaviour of fibre metal laminates subjected to a low velocity impact. Science China Physics, Mechanics and Astronomy 2011; 54:1168–77.

[10] Fan J, Guan Z, Cantwell WJ. Modeling perforation in glass fiber reinforced composites subjected to low velocity impact loading. Polymer Composites 2011; 32:1380–8.

[11] Cairns D. Static and dynamic strain energy release rates in toughened thermosetting composite laminates. FAA, Ninth DOD (NASA) FAA Conference on Fibrous Composites in Structural Design 1992; 3:1529–38.

[12] Kim J-K, MacKay DB, Mai Y-W. Drop-weight impact damage tolerance of CFRP with rubber-modified epoxy matrix. Composites 1993; 24:485–94.

[13] Richardson MO., Wisheart MJ. Review of low-velocity impact properties of composite materials. Composites Part A: Applied Science and Manufacturing 1996; 27:1123–31.

[14] Konur O, Matthews FL. Effect of the properties of the constituents on the fatigue performance of composites: a review. Composites 1989; 20:317–28.

[15] Davies GAO. Damage tolerance to low-velocity impact of laminated composite. vol. 4. 2000.

[16] Dorey G, Bishop SM, Curtis PT. On the impact performance of carbon fibre laminates with epoxy and PEEK matrices. Composites Science and Technology 1985; 23:221–37.

[17] Nairn J a., Harper SI, Bascom WD. Effects of fiber, matrix, and interphase on carbon fiber composite compression strength. 1994.

[18] Cantwell WJ, Morton J. The impact resistance of composite materials — a review. Composites 1991; 22:347–62.

[19] Davies P, Cantwell W, Richard H, Moulin C, Kausch HH. Interlaminar Fracture Testing of Carbon Fibre/Peek Composites Validity and Applications. In: Bunsell AR, Lamicq P, Massiah A, editors. Developments in the Science and Technology of Composite Materials SE - 102, Springer Netherlands; 1989, p. 747–55.

[20] Beaumont P. Failure of fibrous composites. 1981.

[21] Robinson P, Davies G a. O. Impactor mass and specimen geometry effects in low velocity impact of laminated composites. International Journal of Impact Engineering 1992; 12:189–207.

[22] Olsson R. Mass criterion for wave controlled impact response of composite plates. Composites Part A: Applied Science and Manufacturing 2000; 31:879-87.

[23] Sjoblom PO, Hartness JT, Cordell TM. On Low-Velocity Impact Testing of Composite Materials. Journal of Composite Materials 1988; 22:30–52.

[24] Abrate S. Impact on Laminated Composites: Recent Advances. Applied Mechanics Reviews 1994; 47:517.

[25] Liu D, Lansing E, Malvern LE. Cracking in Impacted Glass / Epoxy Plates 1987:594– 609.

[26] Godwin W, Davies GAO. Impact behaviour of thermoplastic composites. International Conference Computer Aided Design in Composite Material Technology 1988:371–82.

[27] ASTM standard D7136 / D7136M. Standard Test Method for Measuring the Damage Resistance of a Fiber-Reinforced Polymer Matrix Composite to a Drop-Weight Impact Event 2003.

[28] Hongkarnjanakul N, Rivallant S, Bouvet C, Miranda a. Permanent indentation characterization for low-velocity impact modelling using three-point bending test. Journal of Composite Materials 2013; 48:2441–54.

[29] Bouvet C, Rivallant S, Barrau JJ. Low velocity impact modeling in composite laminates capturing permanent indentation. Composites Science and Technology 2012; 72:1977–88.

[30] González EV, Maimí P, Camanho PP, Turon A, Mayugo J a. Simulation of drop-weight impact and compression after impact tests on composite laminates. Composite Structures 2012; 94:3364–78.

[31] Bull DJ, Spearing SM, Sinclair I. Observations of damage development from compression-after-impact experiments using ex situ micro-focus computed tomography. Composites Science and Technology 2014; 97:106–14.

[32] Esrail F, Kassapoglou C. An efficient approach for damage quantification in quasiisotropic composite laminates under low speed impact. Composites Part B: Engineering 2014; 61:116–26.

[33] Shi Y, Pinna C, Soutis C. Modelling impact damage in composite laminates: A simulation of intra- and inter-laminar cracking. Composite Structures 2014; 114:10–9.

[34] Nettles A, Hromisin S. Normalization of Impact Energy by Laminate Thickness for Compression After Impact Testing 2013.

[35] Shi Y, Swait T, Soutis C. Modelling damage evolution in composite laminates subjected to low velocity impact. Composite Structures 2012; 94:2902–13.

[36] González EV, Maimí P, Camanho PP, Lopes CS, Blanco N. Effects of ply clustering in laminated composite plates under low-velocity impact loading. Composites Science and Technology 2011; 71:805–17.

[37] Swanson SR. Limits of quasi-static solutions in impact of composite structures. Composites Engineering 1992; 2:261–7.

[38] Olsson R. Impact Response of Composite Laminates: A Guide to Closed Form Solutions. Aeronautical Research Institute of Sweden; 1993.

[39] Christoforou AP, Yigit AS. Characterization of impact in composite plates. Composite Structures 1998; 43:15–24.

[40] Loikkanen M, Praveen G, Powell D. Simulation of Ballistic Impact on Composite Panels. 10th International LS-DYNA Users Conference; 1–12.

[41] Zhang ZY, Richardson MOW. Visualisation of barely visible impact damage in polymer matrix composites using an optical deformation and strain measurement system (ODSMS). Composites Part A: Applied Science and Manufacturing 2005; 36:1073–8.

[42] Prichard JC, Hogg PJ. The role of impact damage in post-impact compression testing. Composites 1990; 21:503–11.

[43] Shyr T-W, Pan Y-H. Impact resistance and damage characteristics of composite laminates. Composite Structures 2003; 62:193–203.

[44] Chang F. A Model for Predicting Damage in Graphite/Epoxy Laminated Composites Resulting from Low-Velocity Point Impact. Journal of Composite Materials 1992; 26:2134–69.

[45] Sridharan S. Delamination behaviour of composites. 1st ed. Woodhead Publishing; 2008.

[46] Robinson P, Greenhalgh E, Pinho S. Failure mechanisms in polymer matrix composites: Criteria, testing and industrial applications. Elsevier; 2012

[47] Dvorak GJ, Laws N. Analysis of Progressive Matrix Cracking In Composite Laminates II. First Ply Failure. Journal of Composite Materials 1987; 21:309–29.

[48] Nairn J a. Matrix Microcracking in Composites. Comprehensive Composite Materials 2000; 2:1–34.

[49] Gdoutos EE, Giannakopoulou a. Stress and failure analysis of brittle matrix composites. Part I: Stress analysis. International Journal of Fracture 1999:263–77.

[50] Abrate S. Impact on composite structures. Cambridge University Press; 2005.

[51] Chiao T, Reifsnider K, Sendeckyj G, Morgan R, Lien P, Takeda N, et al. Microscopic Observations of Cross Sections of Impacted Composite Laminates. Journal of Composites Technology and Research 1982; 4:40.

[52] Joshi SP, Sun CT. Impact Induced Fracture in a Laminated Composite. Journal of Composite Materials 1985; 19:51–66.

[53] Choi HY, Chang F-K. A Model for Predicting Damage in Graphite/Epoxy Laminated Composites Resulting from Low-Velocity Point Impact. Journal of Composite Materials 1992; 26:2134–69.

[54] Choi HY, Wu HT, Chang F-K. A New Approach toward Understanding Damage Mechanisms and Mechanics of Laminated Composites Due to Low-Velocity Impact: Part I—Analysis. Journal of Composite Materials 1991; 25:1012–38.

[55] Parvizi A, Garrett KW, Bailey JE. Constrained cracking in glass fibre-reinforced epoxy cross-ply laminates. Journal of Materials Science 1978; 13:195–201.

[56] Cantwell WJ, Morton J. Geometrical effects in the low velocity impact response of CFRP. Composite Structures 1989; 12:39–59.

[57] Wisnom MR, Hallett SR. The role of delamination in strength, failure mechanism and hole size effect in open hole tensile tests on quasi-isotropic laminates. Composites Part A: Applied Science and Manufacturing 2009; 40:335–42.

[58] Sun CT, Zhou SG. Failure of Quasi-Isotropic Composite Laminates with Free Edges. Journal of Reinforced Plastics and Composites 1988; 7:515–57.

[59] Lorriot T, Marion G, Harry R, Wargnier H. Onset of free-edge delamination in composite laminates under tensile loading. Composites Part B: Engineering 2003; 34:459–71.

[60] Vidyashankar BR, Krishna Murty a. V. Analysis of laminates with ply drops. Composites Science and Technology 2001; 61:749–58.

[61] Kedward KT, Wilson RS, McLean SK. Flexure of simply curved composite shapes. Composites 1989; 20:527–36.

[62] Guynn EG, Obrien TK. The influence of lay-up and thickness on composite impact damage and compression strength 1985.

[63] Buynak CF, Moran TJ. Characterization of Impact Damage in Composites. In: Thompson D, Chimenti D, editors. Review of Progress in Quantitative Nondestructive Evaluation SE - 137, vol. 6 A, Springer US; 1987, p. 1203–11.

[64] Davies GAO, Robinson P, Robson J, Eady D. Shear driven delamination propagation in two dimensions. Composites Part A: Applied Science and Manufacturing 1997; 28:757–65.

[65] Liu D. Impact induced delamination — a view of bending stiffness mismatching. Composites 1989; 20:287.

[66] Kumar P, Rai B. Impact damage on single interface GFRP laminates—An experimental study. Composite Structures 1991; 18:1–10.

[67] Aymerich F, Meili S. Ultrasonic evaluation of matrix damage in impacted composite laminates. Composites Part B: Engineering 2000; 31:1–6.

[68] Bouvet C, Castanié B, Bizeul M, Barrau J-J. Low velocity impact modelling in laminate composite panels with discrete interface elements. International Journal of Solids and Structures 2009; 46:2809–21.

[69] Lesser A., Filippov, A G. Kinetics of damage mechanisms in laminated composites. Int SAMPLE Symp and Exhibition 26 Part 1 1991:886–900.

[70] Davies GAO, Zhang X. Impact damage prediction in carbon composite structures. International Journal of Impact Engineering 1995; 16:149–70.

[71] Abdallah EA, Bouvet C, Rivallant S, Broll B, Barrau J-J. Experimental analysis of damage creation and permanent indentation on highly oriented plates. Composites Science and Technology 2009; 69:1238–45.

[72] He W, Guan Z, Li X, Liu D. Prediction of permanent indentation due to impact on laminated composites based on an elasto-plastic model incorporating fiber failure. Composite Structures 2013; 96:232–42.

[73] Lopes CS, Seresta O, Coquet Y, Gürdal Z, Camanho PP, Thuis B. Low-velocity impact damage on dispersed stacking sequence laminates. Part I: Experiments. Composites Science and Technology 2009; 69:926–36.

[74] Caprino G, Lopresto V. The significance of indentation in the inspection of carbon fibre-reinforced plastic panels damaged by low-velocity impact. Composites Science and Technology 2000; 60:1003–12.

[75] Johnson RR. Thermal expansion properties of composite materials 1981.

[76] Caprino G, Langella A, Lopresto V. Indentation and penetration of carbon fibre reinforced plastic laminates. Composites Part B: Engineering 2003; 34:319–25.

[77] Faggiani a., Falzon BG. Predicting low-velocity impact damage on a stiffened composite panel. Composites Part A: Applied Science and Manufacturing 2010; 41:737–49.

[78] Tan W, Falzon BG, Chiu LNS, Price M. Predicting low velocity impact damage and Compression-After-Impact (CAI) behaviour of composite laminates. Composites Part A: Applied Science and Manufacturing 2015; 71:212–26.

[79] Bouvet C, Rivallant S, Barrau JJ. Modelling of Impact Damage and Permanent Indentation on Laminate Composite Plate. 14Th European Conference on Composite Materials 2010:1–10.

[80] Bull DJ, Helfen L, Sinclair I, Spearing SM, Baumbach T. A comparison of multi-scale 3D X-ray tomographic inspection techniques for assessing carbon fibre composite impact damage. Composites Science and Technology 2013; 75:55–61.

[81] Soutis C, Fleck N a, Smith P a. Failure Prediction Technique for Compression Loaded Carbon Fibre-Epoxy Laminate with Open Holes. Journal of Composite Materials 1991; 25:1476–98.

[82] Ahmed A, Wei L. The low-velocity impact damage resistance of the composite structures - A review. vol. 40. 2015.

[83] Hedrick JC, Patel NM, McGrath JE. Toughening of Epoxy Resin Networks with Functionalized Engineering Thermoplastics. Toughened Plastics I; 293–304.

[84] Riew CK, Kinloch AJ. Toughened Plastics I. Washington, DC: American Chemical Society; 1993.

[85] Cantwell WJ, Curtis PT, Morton J. An assessment of the impact performance of CFRP reinforced with high-strain carbon fibres. Composites Science and Technology 1986; 25:133-48.

[86] Gustin J, Joneson A, Mahinfalah M, Stone J. Low velocity impact of combination Kevlar/carbon fiber sandwich composites. Composite Structures 2005; 69:396–406.

[87] Running DM, Ligon JB, Miskioglu I. from the SAGE Social Science Collections. Journal of Composite Materials 1999; 33:928–40.

[88] Zhang X, Hounslow L, Grassi M. Improvement of low-velocity impact and compression-after-impact performance by z-fibre pinning. Composites Science and Technology 2006; 66:2785–94.

[89] Aslan Z, Karakuzu R, Okutan B. The response of laminated composite plates under low-velocity impact loading. Composite Structures 2003; 59:119–27.

[90] Mitrevski T, Marshall IH, Thomson R, Jones R, Whittingham B. The effect of impactor shape on the impact response of composite laminates. Composite Structures 2005; 67:139–48.

[91] Fuoss E, Straznicky P, Poon C. Effects of stacking sequence on the impact resistance in composite laminates—Part 1: parametric study. Composite Structures 1998; 8223.

[92] Lopes CS, Camanho PP, Gürdal Z, Maimí P, González EV. Low-velocity impact damage on dispersed stacking sequence laminates. Part II: Numerical simulations. Composites Science and Technology 2009; 69:937–47.

[93] Hitchen SA, Kemp RMJ. The effect of stacking sequence on impact damage in a carbon fibre/epoxy composite. Composites 1995; 26:207–14.

[94] Zhou G. Damage mechanisms in composite laminates impacted by a flat-ended impactor. Composites Science and Technology 1995; 54:267–73.

[95] Schoeppner G a., Abrate S. Delamination threshold loads for low velocity impact on composite laminates. Composites Part A: Applied Science and Manufacturing 2000; 31:90315.

[96] Shivakumar KN, Elber W, Illg W. Prediction of Impact Force and Duration Due to Low-Velocity Impact on Circular Composite Laminates. Journal of Applied Mechanics 1985; 52:674.

[97] Lee J, Soutis C. Prediction of Impact-Induced Fibre Damage in Circular Composite Plates. Applied Composite Materials 2005; 12:109–31.

[98] Suemasu H, Majima O. Multiple Delaminations and their Severity in Circular Axisymmetric Plates Subjected to Transverse Loading. Journal of Composite Materials 1996; 30:441–53.

[99] Suemasu H, Majima O. Multiple Delaminations and their Severity in Nonlinear Circular Plates Subjected to Concentrated Loading. Journal of Composite Materials 1998; 32:123–40.

[100] Kelkar AD, Sankar J, Rajeev K, Aschenbrenner RJ, Schoeppner G. Analysis of tensile preloaded composites subjected to low-velocity impact loads. In: 39 AIAA/ASME/ASCE/AHS/ASC Structures, Structural Dynamics and Material Conference 1998:1978–87.

[101] Chiu S-T, Liou Y-Y, Chang Y-C, Ong C. Low velocity impact behavior of prestressed composite laminates. Materials Chemistry and Physics 1997; 47:268–72.

[102] Heimbs S, Heller S, Middendorf P, Hähnel F, Weiße J. Low velocity impact on CFRP plates with compressive preload: Test and modelling. International Journal of Impact Engineering 2009; 36:1182–93.

[103] Whittingham B, Marshall IH, Mitrevski T, Jones R. The response of composite structures with pre-stress subject to low velocity impact damage. Composite Structures 2004; 66:685–98.

[104] Malhotra A, Guild FJ, Pavier MJ. Edge impact to composite laminates: experiments and simulations. Journal of Materials Science 2008; 43:6661–7.

[105] Kutlu Z, Chang F-K. Matrix Cracking and Delamination in Laminated Composite Beams Subjected to a Transverse Concentrated Line Load. Journal of Composite Materials 1993; 27:436–70.

[106] Stout MG, Koss D a., Liu C, Idasetima J. Damage development in carbon/epoxy laminates under quasi-static and dynamic loading. Composites Science and Technology 1999; 59:2339–50.

[107] Yokozeki T, Kuroda A, Yoshimura A, Ogasawara T, Aoki T. Damage characterization in thin-ply composite laminates under out-of-plane transverse loadings. Composite Structures 2010; 93:49–57.

[108] Kaczmarek H, Maison S. Comparative ultrasonic analysis of damage in CFRP under static indentation and low-velocity impact. Composites Science and Technology 1994; 51:11–26.

[109] Kwon YS, Sankar B V. Indentation-flexure and low-velocity impact damage in graphite epoxy laminates. Journal of Composites Technology and Research 1993; 15:101.

[110] Guinard S, Allix O, Guedradegeorges D, Vinet a. A 3D damage analysis of low-velocity impacts on laminated composites. Composites Science and Technology 2002; 62:585–9.

[111] Chen P, Shen Z, Xiong J, Yang S, Fu S, Ye L. Failure mechanisms of laminated composites subjected to static indentation. Composite Structures 2006; 75:489–95.

[112] Aymerich F, Dore F, Priolo P. Simulation of multiple delaminations in impacted cross-ply laminates using a finite element model based on cohesive interface elements. Composites Science and Technology 2009; 69:1699–709.

[113] Saito H, Morita M, Kawabe K, Kanesaki M, Takeuchi H, Tanaka M, et al. Effect of ply-thickness on impact damage morphology in CFRP laminates. Journal of Reinforced Plastics and Composites 2011; 30:1097–106.

[114] Nettles A, Douglas M, Estes E. Scaling effects in carbon/epoxy laminates under transverse quasi-static loading. NASA Technical Report 1999; NASA/TM-19.

[115] Yang FJ, Cantwell WJ. Impact damage initiation in composite materials. Composites Science and Technology 2010; 70:336–42.

[116] Lee SM, Zahuta P, Corpornrioti C. Instrumented impact and static indentation of composites. Journal of Composite Materials 1991:204.

[117] Nettles A, Douglas M. A comparison of quasi-static indentation to low-velocity impact. NASA Technical Report 2000; NASA/TP-20.

[118] Bull DJ. Damage Assessment of particle toughened carbon fibre composites subjected to impact and compression after impact using 3D X-ray tomography. PhD Thesis 2014.

[119] Brindle a. R, Zhang X. Predicting the Compression-After-Impact Performance of Carbon Fibre Composites.

[120] Liu H. Ply clustering effect on composite laminates under low-velocity impact using FEA. Cranfield University, School of Engineering, 2012.

[121] Symons DD. Characterization of indentation damage in 0/90 lay-up T300/914 CFRP. Composites Science and Technology 2000; 60:391–401.

[122] Lin C, Fatt MSH. Perforation of Composite Plates and Sandwich Panels under Quasistatic and Projectile Loading. Journal of Composite Materials 2006; 40:1801–40.

[123] Yang S, Sun C. Indentation law for composite laminates. ASTM STP 1982.

[124] Wu E, Shyu K. Response of Composite Laminates to Contact Loads and Relationship to Low-Velocity Impact. Journal of Composite Materials 1993; 27:1443–64.

[125] Sun CT. An analytical method for evaluation impact damage energy of laminated composites. ASTM Special Technical Publication 1977:427–40.

[126] Abrate S. Modeling of impacts on composite structures. Composite Structures 2001; 51:129–38.

[127] Wu E, Yen C-S. The Contact Behavior Between Laminated Composite Plates and Rigid Spheres. Journal of Applied Mechanics 1994; 61:60.

[128] Zhang X, Hounslow L, Grassi M. Improvement of low-velocity impact and compression-after-impact performance by z-fibre pinning. Composites Science and Technology 2006; 66:2785–94.

[129] Tan TM, Sun CT. Use of Statical Indentation Laws in the Impact Analysis of Laminated Composite Plates. Journal of Applied Mechanics 1985; 52:6.

[130] Suemasu H, Kerth S, Maier M. Indentation of Spherical Head Indentors on Transversely Isotropic Composite Plates. Journal of Composite Materials 1994; 28:1723–39.

[131] Esrail F, Kassapoglou C. An efficient approach to determine compression after impact strength of quasi-isotropic composite laminates. Composites Science and Technology 2014; 98:28–35.

[132] Kassapoglou C. Modeling the Effect of Damage in Composite Structures: Simplified Approaches. John Wiley & Sons; 2015.

[133] Shahid I, Chnag F-K, Shah B. Impact damage resistance and damage tolerance of composite with progressive damage. 37th Structure, Structural Dynamics and Materials Conference, 1996, p. 766–75.

[134] Guan Z, Yang C. Low-velocity impact and damage process of composite laminates. Journal of Composite Materials 2002; 36:851–71.

[135] Yigit AS, Christoforou AP. Limits of asymptotic solutions in low-velocity impact of composite plates. Composite Structures 2007; 81:568–74.

[136] Yigit AS, Christoforou AP. Limits of asymptotic solutions in low-velocity impact of composite plates. Composite Structures 2007; 81:568–74.

[137] Davies, GAO Olsson R. Impact on composite structures. Aeronautical Journal 2004; Vol. 108:no. 1089.

[138] Hinton M. Failure Criteria in Fibre Reinforced Polymer Composites: Can any of the Predictive Theories be Trusted? QinetiQ 2011. www.nafems.org/downloads/nwc11/keynotes/hinton.pdf.

[139] Kaddour A, Hinton M, Smith P, Li S. A comparison between the predictive capability of matrix cracking, damage and failure criteria for fibre reinforced composite laminates: Part A of the third world-wide failure exercise. Journal of Composite Materials 2013;47:2749–79.

[140] Jackson W, Jr CP. The use of impact force as a scale parameter for the impact response of composite laminates 1992.

[141] Olsson R, Donadon M V., Falzon BG. Delamination threshold load for dynamic impact on plates. International Journal of Solids and Structures 2006; 43:3124–41.

[142] Olsson R. Analytical prediction of large mass impact damage in composite laminates. Composites Part A: Applied Science and Manufacturing 2001; 32:1207–15.

[143] Suemasu H, Wisnom MR, Sun XC, Hallett SR. An analytical study on multiple delaminations and instability in nonlinear plate subjected to transverse concentrated load. 13th Japan International SAMPE Symposium and Exhibition 2013.

[144] Donadon MV, Iannucci L, Falzon BG, Hodgkinson JM, de Almeida SFM. A progressive failure model for composite laminates subjected to low velocity impact damage. Computers & Structures 2008; 86:1232–52.

[145] Kim E-H, Rim M-S, Lee I, Hwang T-K. Composite damage model based on continuum damage mechanics and low velocity impact analysis of composite plates. Composite Structures 2013; 95:123–34.

[146] Lopes C.S., Camanho P.P., Gurdal Z., Maimi P. and Gonzalez E.V., Low-velocity impact damage on dispersed stacking sequence laminates, Part II: Numerical simulations, Composites Science and Technology; 69; 2009; 937-947.

[147] Bull D.J., Helfen L., Sinclair I., Spearing S.M. and Baumbach T., A comparison of multi-scale 3D X-ray tomographic inspection techniques for

assessing carbon fibre composite impact damage, Composites Science and Technology; 75; 2013; 55-61.

[148] Swanson S.R., Limits of quasi-static solutions in impact of composite structures, Composites Engineering; 2; 1992; 261–267.

[149] Kaczmarek H. and Maison S., Comparative ultrasonic analysis of damage in CFRP under static indentation and low-velocity impact, Composites Science and Technology; 51; 1994; 11-26.

[150] Nettles A.T. and Douglas M.J., A Comparison of Quasi-Static Indentation to Low-Velocity Impact, NASA Technical Publication NASA/TP-2000-210481, 2000.

[151] Ostré B., Bouvet C., Minot C. and Aboissière J., Edge impact modeling on stiffened composite structures, Composite Structures, 126, 2015, pp. 314-328.

[152] Bolotin and Vladimir V., Delaminations in composite structures: its origin, buckling, growth and stability, Composites Part B: Engineering, 27, 1996, pp. 129-145.

[153] Breen C., Guild F. and Pavier M., Impact damage to thick carbon fibre reinforced plastic composite laminates, Journal of materials science, 41, 2006, pp. 6718-6724.

[154] Malhotra A., Guild F.J., and Pavier M.J., Edge impact to composite laminates: experiments and simulations, Journal of materials science, 43, 2008, pp. 6661-6667.

[155] Liu D., Impact-induced delamination – A view of bending stiffness mismatching, Journal of composite materials, 22, 1988, pp. 674-692.

[156] Olsson R., Closed form prediction of peak load and delamination onset under small mass impact, Composite Structures, 59, 2003, pp. 341-349.

[157] Olsson R., Donadon M.V. and Falzon B.G., Delamination threshold load for dynamic impact on plates, International Journal of Solids and Structures, 43, 2006, pp. 3124-3141.

[158] Liu D. and Li X., An overall view of laminate theories based on displacement hypothesis, Journal of composite materials, 30, 1996, pp. 1539-1561.

[159] Richardson M.O.W., and Wisheart M.J., Review of low-velocity impact properties of composite materials, Composites Part A: Applied Science and Manufacturing, 27, 1996, pp. 1123-1131.

[160] Kassapoglou C., Modeling the Effect of Damage in Composite Structures: Simplified Approaches, John Wiley & Sons, 2015.